

PHASES OF DENSE MATTER IN NEUTRON STARS

Henning HEISELBERG^a, Morten HJORTH-JENSEN^b

^a*NORDITA, Blegdamsvej 17, DK-2100 København Ø, Denmark*

^b*Department of Physics, University of Oslo, N-0316 Oslo, Norway*



ELSEVIER

AMSTERDAM – LAUSANNE – NEW YORK – OXFORD – SHANNON – TOKYO



ELSEVIER

Physics Reports 328 (2000) 237–327

PHYSICS REPORTS

www.elsevier.com/locate/physrep

Phases of dense matter in neutron stars

Henning Heiselberg^{a,*}, Morten Hjorth-Jensen^b

^a*NORDITA, Blegdamsvej 17, DK-2100 København Ø, Denmark*

^b*Department of Physics, University of Oslo, N-0316 Oslo, Norway*

Received August 1999; editor: M. Kamionkowski

Contents

1. Introduction	240	4.4. Melting temperatures	291
1.1. The past, present and future of neutron stars	240	4.5. Funny phases	292
1.2. Physics of neutron stars	241	4.6. Summary of neutron star structures	293
2. Phases of dense matter	243	5. Observational consequences for neutron stars	294
2.1. Prerequisites and definitions	245	5.1. Masses from radio pulsars, X-ray binaries and QPO's	294
2.2. Nucleonic degrees of freedom	248	5.2. TOV and Hartle's equations	296
2.3. A causal parametrization of the nuclear matter EoS	265	5.3. Neutron star properties from various equations of state	300
2.4. Hyperonic matter	269	5.4. Maximum masses	304
2.5. Kaon condensation	275	5.5. Phase transitions in rotating neutron stars	306
2.6. Pion condensation	276	5.6. Core quakes and glitches	311
2.7. Superfluidity in baryonic matter	277	5.7. Backbending and giant glitches	312
2.8. Quark matter	281	5.8. Cooling and temperature measurements	313
3. Thermodynamics of multi-component phase transitions	283	5.9. Supernovae	318
3.1. Maxwell construction for one-component systems	283	5.10. Gamma-ray bursters	319
3.2. Two-component systems in a mixed phase	285	6. Conclusions	320
4. Structure of neutron stars	285	6.1. Many-body approaches to the equation of state	320
4.1. Screening lengths	286	6.2. Phase transitions and stiffness of EoS from masses of neutron stars	321
4.2. Surface and Coulomb energies of the mixed phase	287	Acknowledgements	322
4.3. Is the mixed phase energetically favored?	289	References	322

*Corresponding author.

E-mail addresses: hh@nordita.dk (H. Heiselberg), m.h.jensen@fys.uio.no (M. Hjorth-Jensen)

Abstract

Recent equations of state for dense nuclear matter are discussed with possible phase transitions arising in neutron stars such as pion, kaon and hyperon condensation, superfluidity and quark matter. Specifically, we treat the nuclear to quark matter phase transition, the possible mixed phase and its structure. A number of numerical calculations of rotating neutron stars with and without phase transitions are given and compared to observed masses, radii, temperatures and glitches. © 2000 Elsevier Science B.V. All rights reserved.

PACS: 12.38.Mh; 21.30. – x; 21.65. + f; 26.60. + c; 97.60.Gb; 97.60.Jd

Keywords: Neutron star properties; Phase transitions; Equation of state for dense neutron star matter

1. Introduction

1.1. The past, present and future of neutron stars

The discovery of the neutron by Chadwick in 1932 prompted Landau to predict the existence of neutron stars. The birth of such stars in supernovae explosions was suggested by Baade and Zwicky in 1934. First theoretical neutron star calculations were performed by Tolman, Oppenheimer and Volkoff in 1939 and Wheeler around 1960. Bell and Hewish were the first to discover a neutron star in 1967 as a *radio pulsar*. The discovery of the rapidly rotating Crab pulsar in the remnant of the Crab supernova observed by the Chinese in 1054 A.D. confirmed the link to supernovae. Radio pulsars are rapidly rotating with periods in the range $0.033 \text{ s} \leq P \leq 4.0 \text{ s}$. They are believed to be powered by rotational energy loss and are rapidly spinning down with period derivatives of order $\dot{P} \sim 10^{-12}$ – 10^{-16} . Their high magnetic field B leads to dipole magnetic braking radiation proportional to the magnetic field squared. One estimates magnetic fields of the order of $B \sim 10^{11}$ – 10^{13} G . The total number of pulsars discovered so far has just exceeded 1000 before the turn of the millenium and the number is increasing rapidly.

A distinct subclass of radio pulsars are *millisecond pulsars* with periods between $1.56 \text{ ms} \leq P \leq 100 \text{ ms}$. The period derivatives are very small corresponding to very small magnetic fields $B \sim 10^8$ – 10^{10} G . They are believed to be recycled pulsars, i.e. old pulsars with low magnetic fields that have been spun up by accretion preserving their low magnetic field and therefore only slowly spinning down. About 20 – almost half of the millisecond pulsars – are found in binaries where the companion is either a white dwarf or a neutron star. Six double neutron stars are known so far including the Hulse–Taylor PSR 1513 + 16. The first binary pulsar was found by Hulse and Taylor in 1973 and by measuring the general relativistic corrections to Newtonian gravity one could determine all parameters in the binary system as both masses, orbital periods and period derivatives, orbital distances and inclination. Parameters are overdetermined and thus provide a test of general relativity. Inward spiralling or orbital decay is an additional test of general relativity to an unprecedented accuracy. The binary neutron stars all have masses in the narrow interval 1.3 – $1.5 M_{\odot}$, which may either be due to the creation process or that heavier neutron stars are unstable.

With X-ray detectors on board satellites since 1971 almost two hundred *X-ray pulsars and bursters* have been found of which the orbital period has been determined for about sixty. The X-ray pulsars and bursters are believed to be accreting neutrons stars from high ($M \gtrsim 10 M_{\odot}$) and low mass ($M \lesssim 1.2 M_{\odot}$) companions, respectively. The X-ray pulses are most probably due to strong accretion on the magnetic poles emitting X-ray (as northern lights) with orbital frequency. The X-ray bursts are due to slow accretion spreading all over the neutron star surface before igniting in a thermonuclear flash. The resulting (irregular) bursts have periods depending on accretion rates rather than orbital periods. Recently, bursters and pulsars have been linked by observations of X-ray pulsations in bursts from several low mass X-ray bursters [1]. The pulsations are with spin frequency 300–400 Hz and increase by a few Hz only during the burst. The small increase is expected from cooling after a thermonuclear explosion, which leads to smaller size and moment of inertia and, conserving angular momentum, to larger frequency. The radiation from X-ray bursters is not blackbody and therefore only upper limits on temperatures can be extracted from observed luminosities in most cases. Masses are less accurately measured than for binary

pulsars. We mention recent mass determinations for the X-ray pulsar Vela X-1: $M = (1.9 \pm 0.1)M_{\odot}$, and the burster Cygnus X-2: $M = (1.8 \pm 0.2)M_{\odot}$, which will be discussed later. A subclass of six anomalous X-ray pulsars are slowly rotating but rapidly spinning down indicating that they are young with enormous magnetic fields, $B \sim 10^{15}$ G, and thus named *Magnetars* [3]. Recently, quasi-periodic oscillations (QPO) have been found in 12 low mass X-ray binaries. The QPO's set strict limits on masses and radii of neutrons stars, but if the periodic oscillations arrive from the innermost stable orbit [4], it implies definite neutron star masses up to $M \simeq 2.3M_{\odot}$.

Non-rotating and non-accreting neutron stars are virtually undetectable. With the Hubble space telescope one single thermally radiating neutron star has been found [5]. Its distance is only 160 pc from Earth and its surface temperature is $T \simeq 60$ eV. From its luminosity one deduces a radius of the neutron star $R \leq 14$ km. In our galaxy astrophysicists expect a large abundance $\sim 10^8$ of neutron stars. At least as many supernova explosions have occurred since Big Bang which are responsible for all heavier elements present in the Universe today. The scarcity of neutron stars in the solar neighborhood may be due to a high initial velocity (asymmetric “kick”) during their birth in supernovae. Recently, many neutron stars have been found far away from their supernova remnants. Future gravitational microlensing observation may determine the population of such “invisible” neutron stars as dark matter objects in the galactic halo.

From the view of physicists (and mass extinctionists) supernova explosions are unfortunately rare in our and neighboring galaxies. The predicted rate is 1–3 per century in our galaxy but the most recent one was 1987A in LMC. With luck we may observe one in the near future which produces a rapidly rotating pulsar. Light curves and neutrino counts will test supernova and neutron star models. The rapid spin down may be exploited to test the structure and possible phase transitions in the cores of neutron stars [6–8].

The recent discovery of afterglow in gamma ray bursters (GRB) allows determination of the very high redshifts ($z \geq 1$) and thus the enormous distance and energy output $E \sim 10^{53}$ ergs in GRB if isotropically emitted. Very recently evidence for beaming or jets has been found [2] corresponding to “only” $E \sim 10^{51}$ ergs. Candidates for such violent events neutron star mergers or a special class of type Ic supernova (*hypernovae*) where cores collapse to black holes. The latter is confirmed by recent observations of a bright supernova coinciding with GRB 980326.

The marvelous discoveries made in the past few decades will continue as numerous earth-based and satellite experiments are running at present and more will be launched. History tells us that the future will bring great surprises and discoveries in this field.

1.2. Physics of neutron stars

The physics of compact objects like neutron stars offers an intriguing interplay between nuclear processes and astrophysical observables. Neutron stars exhibit conditions far from those encountered on earth; typically, expected densities ρ of a neutron star interior are of the order of 10^3 or more times the density $\rho_d \approx 4 \times 10^{11}$ g/cm³ at ‘neutron drip’, the density at which nuclei begin to dissolve and merge together. Thus, the determination of an equation of state (EoS) for dense matter is essential to calculations of neutron star properties. The EoS determines properties such as the mass range, the mass–radius relationship, the crust thickness and the cooling rate. The same EoS

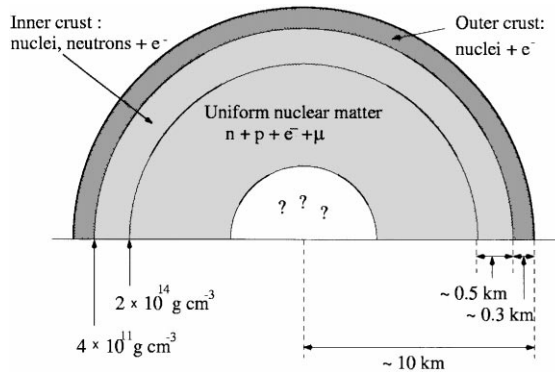


Fig. 1. Possible structure of a neutron star.

is also crucial in calculating the energy released in a supernova explosion. Clearly, the relevant degrees of freedom will not be the same in the crust region of a neutron star, where the density is much smaller than the saturation density of nuclear matter, and in the center of the star, where density is so high that models based solely on interacting nucleons are questionable. These features are pictorially displayed in Fig. 1. Neutron star models including various so-called realistic equations of state result in the following general picture of the interior of a neutron star. The surface region, with typical densities $\rho < 10^6 \text{ g/cm}^3$, is a region in which temperatures and magnetic fields may affect the equation of state. The outer crust for $10^6 \text{ g/cm}^3 < \rho < 4 \times 10^{11} \text{ g/cm}^3$ is a solid region where a Coulomb lattice of heavy nuclei coexist in β -equilibrium with a relativistic degenerate electron gas. The inner crust for $4 \times 10^{11} \text{ g/cm}^3 < \rho < 2 \times 10^{14} \text{ g/cm}^3$ consists of a lattice of neutron-rich nuclei together with a superfluid neutron gas and an electron gas. The neutron liquid for $2 \times 10^{14} \text{ g/cm}^3 < \rho < \times 10^{15} \text{ g/cm}^3$ contains mainly superfluid neutrons with a smaller concentration of superconducting protons and normal electrons [9]. At higher densities, typically 2–3 times nuclear matter saturation density, interesting phase transitions from a phase with just nucleonic degrees of freedom to quark matter may take place [10]. Furthermore, one may have a mixed phase of quark and nuclear matter [6,11], kaon [12] or pion condensates [13,14], hyperonic matter [6,15–20], strong magnetic fields in young stars [21,22], etc.

The first aim of this work is therefore to attempt at a review of various approaches to the equation of state for dense neutron star matter relevant for stars which have achieved thermal equilibrium. Various approaches to the EoS and phases which may occur in a neutron star are discussed in Section 2 while an overview of the thermodynamical properties of the mixed phase and possible phases in neutron stars are presented in Sections 3 and 4.

Our second aim is to discuss the relation between the EoS and various neutron star observables when a phase transition in the interior of the star occurs. Astronomical observations leading to global neutron star parameters such as the total mass, radius, or moment of inertia, are important since they are sensitive to microscopic model calculations. The mass, together with the moment of inertia, are also the gross structural parameters of a neutron star which are most accessible to observation. It is the mass which controls the gravitational interaction of the star with other systems such as a binary companion. The moment of inertia controls the energy stored in rotation

and thereby the energy available to the pulsar emission mechanism. Determining the possible ranges of neutron star is not only important in constraining the EoS, but has important theoretical consequences for the observational prediction of black holes in the universe. Examples are the galactic black hole candidates Cyg X-1 [23] and LMC X-3 [24], which are massive X-ray binaries. Their masses ($0.25M_{\odot}$ and $2.3M_{\odot}$) are, however, smaller than for some low-mass X-ray binaries like A0620-00 [25] and V404 Cyg [26], which make better black hole candidates with mass functions in excess of three solar masses. There is a maximum mass a non-rotating neutron star can have. There is however no upper limit on the mass a black hole can have. If, therefore, one can find a dense, highly compact object and can argue that its rotation is slow, and can deduce that its mass is greater than the allowed maximum mass allowed to non-rotating (or slowly rotating) neutron stars, then one has a candidate for a black hole.

Since neutron stars are objects of highly compressed matter, this means that the geometry of space–time is changed considerably from that of a flat space. Stellar models must therefore be based on Einstein’s theory of general relativity. Based on several of the theoretical equations of state and possible phases of matter discussed in Sections 2–4, various properties of non-rotating and rotating neutron stars are presented in Section 5. The relevant equations needed for the study of the structure of a neutron star are summarized in this section as well, for both non-rotating and rotating stellar structures. There we also discuss the observational implications when phase transitions occur in the interior of the star. In addition to studies of the mass–radius relationship and the moment of inertia, we also extract analytical properties of quantities like the braking index and the rate of slowdown near the critical angular velocity where the pressure inside the star just exceeds that needed to make a phase transition. The observational properties for first- and second-order phase transitions are also discussed. Other properties like glitches and cooling of stars are also discussed in Section 5. Summary and perspectives are given in Section 6.

Finally, we mention several excellent and recent review articles covering various aspects of neutron stars properties in the literature addressing the interesting physics of the neutron star crust [27], the nuclear equation of state [14], hot neutron star matter [28] in connection with protoneutron stars, and cooling calculations [29]. However, as previously mentioned, our aim will be to focus on the connection between the various possible phases of dense neutron star matter in chemical equilibrium and the implications of first- and second-order phase transitions for various observables.

2. Phases of dense matter

Several theoretical approaches to the EoS for the interior of a neutron star have been considered. Over the past two decades many authors [10] have considered the existence of quark matter in neutron stars. Assuming a first-order phase transition one has, depending on the equation of states, found either complete strange quark matter stars or neutron stars with a core of quark matter surrounded by a mantle of nuclear matter and a crust on top. Recently, the possibility of a mixed phase of quark and nuclear matter was considered [6] and found to be energetically favorable. Including surface and Coulomb energies this mixed phase was still found to be favored for reasonable bulk and interface properties [11]. The structure of the mixed phase of quark matter

embedded in nuclear matter with a uniform background of electrons was studied and resembles that in the neutron drip region in the crust. Starting from the outside, the crust consists of the outer layer, which is a dense solid of neutron-rich nuclei, and the inner layer in which neutrons have dripped and form a neutron gas coexisting with the nuclei. The structure of the latter mixed phase has recently been calculated in detail [27] and is found to exhibit rod-, plate- and bubble-like structures. At nuclear saturation density $\rho_0 \simeq 2.8 \times 10^{14} \text{ g/cm}^3$ there is only one phase of uniform nuclear matter consisting of mainly neutrons, a small fraction of protons and the same amount of electrons to achieve charge neutrality. A mixed phase of quark matter (QM) and nuclear matter (NM) appears already around a few times nuclear saturation density – lower than the phase transition in hybrid stars. In the beginning only few droplets of quark matter appear but at higher densities their number increase and they merge into: QM rods, QM plates, NM rods, NM bubbles, and finally pure QM at very high densities if the neutron stars have not become unstable towards gravitational collapse.

In this section we review various attempts at describing the above possible phases of dense neutron star matter. For the part of the neutron star that can be described in terms of nucleonic degrees of freedom only, i.e. β -stable matter with protons, neutrons and electrons (and also muons), we will try to shed light on recent advances within the framework of various many-body approaches. This review is presented in Section 2.2. For the more exotic states of matter such as hyperonic degrees of freedom we will point to recent studies of hyperonic matter in terms of more microscopic models in Section 2.4. The problem however with e.g. hyperonic degrees of freedom is that knowledge of the hyperon–nucleon or hyperon–hyperon interactions has not yet reached the level of sophistication encountered in the nucleon–nucleon sector. Mean fields methods have however been much favoured in studies of hyperonic matter. A discussion of pion and kaon condensation will also be presented in the two subsequent subsections. Superfluidity is addressed in Section 2.7.

In general, we will avoid a discussion of non-relativistic and relativistic mean fields methods of relevance for neutron matter studies, mainly since such aspects have been covered in depth in the literature, see e.g. Refs. [17,18,30,31]. Moreover, as pointed out by Akmal et al. [14], albeit exhibiting valuable tutorial features, the main problem with relativistic mean field methods is that they rely on the approximation $\mu r \ll 1$, with μ the inverse Compton wavelength of the meson and r the interparticle spacing. For nuclear and neutron matter densities ranging from saturation density to five times saturation density, μr is in the range 1.4 to 0.8 for the pion and 7.8 to 4.7 for vector mesons. Clearly, these values are far from being small. The relativistic mean field approximation can however be based on effective values for the coupling constants, taking thereby into account correlation effects. These coupling constants have however a density dependence and a more microscopic theory is needed to calculate them.

Our knowledge of quark matter is however limited, and we will resort to phenomenological models in Section 2.8 in our description of this phase of matter. Typical models are the so-called Bag model [32] or the Color-Dielectric model [33].

However, before proceeding with the above more specific aspects of neutron star matter, we need to introduce some general properties and features which will enter our description of dense matter. These are introduced in the first subsection. The reader should also note that we will omit a discussion of the properties of matter in the crust of the star since this is covered in depth by the review of Ravenhall and Pethick [27]. Moreover, for neutron stars with masses $\approx 1.4M_\odot$ or greater,

the mass fraction contained in the crust of the star is less than about 2%. We will therefore in our final EoS employ results from earlier works [34,35] for matter at densities $\leq 0.05 \text{ fm}^{-3}$.

2.1. Prerequisites and definitions

At densities of 0.1 fm^{-3} and greater, we will in this work require properties of charge neutral uniform matter to be made of mainly neutrons, protons, electrons and muons in beta equilibrium, although the presence of other baryons will be discussed as well.¹

In this section we will merely focus on distinct phases of matter, such as pure baryonic matter or quark matter. The composition of matter is then determined by the requirements of chemical and electrical equilibrium. Furthermore, we will also consider matter at temperatures much lower than the typical Fermi energies. The equilibrium conditions are governed by the weak processes (normally referred to as the processes for β -equilibrium)

$$b_1 \rightarrow b_2 + l + \bar{\nu}_l, \quad b_2 + l \rightarrow b_1 + \nu_l, \quad (1)$$

where b_1 and b_2 refer to e.g. the baryons being a neutron and a proton, respectively, l is either an electron or a muon and $\bar{\nu}_l$ and ν_l their respective anti-neutrinos and neutrinos. Muons typically appear at a density close to nuclear matter saturation density, the latter being

$$n_0 \approx 0.16 \pm 0.02 \text{ fm}^{-3},$$

with a corresponding binding energy \mathcal{E}_0 for symmetric nuclear matter (SNM) at saturation density of

$$\mathcal{E}_0 = B/A = -15.6 \pm 0.2 \text{ MeV}.$$

In this work the energy per baryon \mathcal{E} will always be in units of MeV, while the energy density ε will be in units of MeV fm^{-3} and the number density² n in units of fm^{-3} . The pressure P is defined through the relation

$$P = n^2 \partial \mathcal{E} / \partial n = n \partial \varepsilon / \partial n - \varepsilon, \quad (2)$$

with dimension MeV fm^{-3} . Similarly, the chemical potential for particle species i is given by

$$\mu_i = (\partial \varepsilon / \partial n_i), \quad (3)$$

with dimension MeV. In our calculations of properties of neutron star matter in β -equilibrium, we will need to calculate the energy per baryon \mathcal{E} for e.g. several proton fractions x_p , which corresponds to the ratio of protons as compared to the total nucleon number (Z/A), defined as

$$x_p = n_p / n, \quad (4)$$

¹ In this work we will also set $G = c = \hbar = 1$, where G is the gravitational constant.

² We will often loosely just use density in our discussions.

where $n = n_p + n_n$, the total baryonic density if neutrons and protons are the only baryons present. In that case, the total Fermi momentum k_F and the Fermi momenta k_{Fp} , k_{Fn} for protons and neutrons are related to the total nucleon density n by

$$n = (2/3\pi^2)k_F^3 = x_p n + (1 - x_p)n = (1/3\pi^2)k_{Fp}^3 + (1/3\pi^2)k_{Fn}^3 . \quad (5)$$

The energy per baryon will thus be labelled as $\mathcal{E}(n, x_p)$. $\mathcal{E}(n, 0)$ will then refer to the energy per baryon for pure neutron matter (PNM) while $\mathcal{E}(n, \frac{1}{2})$ is the corresponding value for SNM. Furthermore, in this work, subscripts n, p, e, μ will always refer to neutrons, protons, electrons and muons, respectively.

Since the mean free path of a neutrino in a neutron star is bigger than the typical radius of such a star (~ 10 km), we will assume throughout that neutrinos escape freely from the neutron star, see e.g. the work of Prakash et al. in Ref. [28] for a discussion on trapped neutrinos. Eq. (1) yields then the following conditions for matter in β equilibrium with e.g. nucleonic degrees freedom only

$$\mu_n = \mu_p + \mu_e , \quad (6)$$

and

$$n_p = n_e , \quad (7)$$

where μ_i and n_i refer to the chemical potential and number density in fm^{-3} of particle species i . If muons are present as well, we need to modify the equation for charge conservation, Eq. (7), to read

$$n_p = n_e + n_\mu ,$$

and require that $\mu_e = \mu_\mu$. With more particles present, the equations read

$$\sum_i (n_{b_i}^+ + n_{l_i}^+) = \sum_i (n_{b_i}^- + n_{l_i}^-) , \quad (8)$$

and

$$\mu_n = b_i \mu_i + q_i \mu_l , \quad (9)$$

where b_i is the baryon number, q_i the lepton charge and the superscripts (\pm) on number densities n represent particles with positive or negative charge. To give an example, it is possible to have baryonic matter with hyperons like Λ and $\Sigma^{-,0,+}$ and isobars $\Lambda^{-,0,+,++}$ as well in addition to the nucleonic degrees of freedom. In this case the chemical equilibrium condition of Eq. (9) becomes, excluding muons,

$$\begin{aligned} \mu_{\Sigma^-} &= \mu_{\Lambda^-} = \mu_n + \mu_e , \\ \mu_{\Lambda} &= \mu_{\Sigma^0} = \mu_{\Lambda^0} = \mu_n , \\ \mu_{\Sigma^+} &= \mu_{\Lambda^+} = \mu_p = \mu_n - \mu_e , \\ \mu_{\Lambda^{++}} &= \mu_n - 2\mu_e . \end{aligned} \quad (10)$$

A transition from hadronic to quark matter is expected at high densities. The high-density quark matter phase in the interior of neutron stars is also described by requiring the system to be locally neutral

$$\frac{2}{3}n_u - \frac{1}{3}n_d - \frac{1}{3}n_s - n_e = 0 , \quad (11)$$

where $n_{u,d,s,e}$ are the densities of the u , d and s quarks and of the electrons (eventually muons as well), respectively. Moreover, the system must be in β -equilibrium, i.e. the chemical potentials have to satisfy the following equations:

$$\mu_d = \mu_u + \mu_e , \quad (12)$$

and

$$\mu_s = \mu_u + \mu_e . \quad (13)$$

Eqs. (11)–(13) have to be solved self-consistently together with e.g. the field equations for quarks at a fixed density $n = n_u + n_d + n_s$. In this section we will mainly deal with distinct phases of matter, the additional constraints coming from the existence of a mixed phase of hadrons and quarks and the related thermodynamics will be discussed in Section 3.

An important ingredient in the discussion of the EoS and the criteria for matter in β -equilibrium is the so-called symmetry energy $\mathcal{S}(n)$, defined as the difference in energy for symmetric nuclear matter and pure neutron matter

$$\mathcal{S}(n) = \mathcal{E}(n, x_p = 0) - \mathcal{E}(n, x_p = \frac{1}{2}) . \quad (14)$$

If we expand the energy per baryon in the case of nucleonic degrees of freedom only in the proton concentration x_p about the value of the energy for SNM ($x_p = \frac{1}{2}$), we obtain,

$$\mathcal{E}(n, x_p) = \mathcal{E}(n, x_p = \frac{1}{2}) + \frac{1}{2}(\mathrm{d}^2\mathcal{E}/\mathrm{d}x_p^2)(n)(x_p - \frac{1}{2})^2 + \dots , \quad (15)$$

where the term $\mathrm{d}^2\mathcal{E}/\mathrm{d}x_p^2$ is to be associated with the symmetry energy $\mathcal{S}(n)$ in the empirical mass formula. If we assume that higher-order derivatives in the above expansion are small (we will see examples of this in the next subsection), then through the conditions for β -equilibrium of Eqs. (6) and (7) and Eq. (3) we can define the proton fraction by the symmetry energy as

$$\hbar c(3\pi^2 n x_p)^{1/3} = 4\mathcal{S}(n)(1 - 2x_p) , \quad (16)$$

where the electron chemical potential is given by $\mu_e = \hbar c k_F$, i.e. ultrarelativistic electrons are assumed. Thus, the symmetry energy is of paramount importance for studies of neutron star matter in β -equilibrium. One can extract information about the value of the symmetry energy at saturation density n_0 from systematic studies of the masses of atomic nuclei. However, these results are limited to densities around n_0 and for proton fractions close to $\frac{1}{2}$. Typical values for $\mathcal{S}(n)$ at n_0 are in the range 27–38 MeV. For densities greater than n_0 it is more difficult to get a reliable information on the symmetry energy, and thereby the related proton fraction. We will shed more light on this topic in the next subsection.

Finally, another property of interest in the discussion of the various equations of state is the incompressibility modulus K at non-zero pressure

$$K = 9 \partial P / \partial n . \quad (17)$$

The sound speed v_s depends as well on the density of the nuclear medium through the relation

$$\left(\frac{v_s}{c} \right)^2 = \frac{dP}{d\varepsilon} = \frac{dP}{dn} \frac{dn}{d\varepsilon} = \left(\frac{K}{9(m_n c^2 + \mathcal{E} + P/n)} \right) . \quad (18)$$

It is important to keep track of the dependence on density of v_s since a superluminal behavior can occur at higher densities for most non-relativistic EoS. Superluminal behavior would not occur with a fully relativistic theory, and it is necessary to gauge the magnitude of the effect it introduces at the higher densities. This will be discussed at the end of this section. The adiabatic constant Γ can also be extracted from the EoS by

$$\Gamma = (n/P) \partial P / \partial n . \quad (19)$$

2.2. Nucleonic degrees of freedom

A major part of the densities inside neutron stars can be well represented by nucleonic degrees of freedom only, namely the inner part of the crust to the outer part of the core, i.e. densities ranging from 0.5 to 2–3 times nuclear matter saturation density. There is a wealth of experimental and theoretical data, see e.g. Ref. [36] for an overview, which lend support to the assumption that nucleons do not lose their individuality in dense matter, i.e. that properties of the nucleon at such densities are rather close to those of free nucleons. The above density range would correspond to internucleon distances of the order of ~ 1 fm. At such interparticle distances there is little overlap between the various nucleons and we may therefore assume that they still behave as individual nucleons and that one can absorb the effects of overlap into the two nucleon interaction. The latter, when embedded in a nuclear medium, is also different from the free nucleon–nucleon interaction. In the medium there are interaction mechanisms which are obviously absent in vacuum. As an example, the one-pion exchange potential is modified in nuclear matter due to “softening” of pion degrees of freedom in matter.

In order to illustrate how the nucleon–nucleon interaction is renormalized in a nuclear medium, we will start with the simplest possible many-body approach, namely the so-called Brueckner–Hartree–Fock (BHF) approach. This is done since the Lippmann–Schwinger equation used to construct the scattering matrix T , which in turn relates to the phase shifts, is rather similar to the G -matrix which enters the BHF approach. The difference resides in the introduction of a Pauli-blocking operator in order to prevent scattering to intermediate particle states prohibited by the Pauli principle. In addition, the single-particle energies of the interacting particle are no longer given by kinetic energies only. However, several of the features seen at the level of the scattering matrix, pertain to the G -matrix as well. Therefore, if one employs different nucleon–nucleon interactions in the calculation of the energy per baryon in pure neutron matter with the BHF G -matrix, eventual differences can be retraced at the level of the T -matrix. We will illustrate these

aspects in the next subsection. More complicated many-body terms and relativistic effects will be discussed in Sections 2.2.2 and 2.2.3.

2.2.1. From the NN interaction to the nuclear G -matrix

The NN interactions we will employ here are the recent models of the Nijmegen group [37], the Argonne V_{18} potential [38] and the charge-dependent Bonn interaction (CD-Bonn [39]). In 1993, the Nijmegen group presented a phase-shift analysis of all proton–proton and neutron–proton data below 350 MeV with a χ^2 per datum of 0.99 for 4301 data entries. The above potentials have all been constructed based on these data. The CD-Bonn interaction has a χ^2 per datum of 1.03 and the same is true for the Nijm-I, Nijm-II and Reid93 potential versions of the Nijmegen group [37]. The new Argonne potential V_{18} [38] has a χ^2 per datum of 1.09.

Although all these potentials predict almost identical phase shifts, their mathematical structure is quite different. The Argonne potential, the Nijm-II and the Reid93 potentials are non-relativistic potential models defined in terms of local potential functions, which are attached to various (non-relativistic) operators of the spin, isospin and/or angular momentum operators of the interacting pair of nucleons. Such approaches to the NN interaction have traditionally been quite popular since they are numerically easy to use in configuration space calculations. The Nijm-I model is similar to the Nijm-II model, but it includes also a \mathbf{p}^2 term, see Eq. (13) of Ref. [37], which may be interpreted as a non-local contribution to the central force. The CD-Bonn potential is based on the relativistic meson-exchange model of Ref. [40] which is non-local and cannot be described correctly in terms of local potential functions.

For a given NN interaction V , the R -matrix (or K -matrix) for free-space two-nucleon scattering is obtained from the Lippmann–Schwinger equation, which reads in the center-of-mass (c.m.) system and in a partial-wave decomposition

$$R_{ll'}^{zT_z}(kk'\omega) = V_{ll'}^{zT_z}(kk') + \sum_{l''} \int \frac{d^3q}{(2\pi)^3} V_{ll''}^{zT_z}(kq) \frac{1}{\omega - H_0} R_{l'l''}^{zT_z}(qk'\omega), \quad (20)$$

with ll' and kk' the orbital angular momentum and the linear momentum of the relative motion, respectively. T_z is the total isospin projection. The angular momentum J and total spin S are represented by the variable α . The term H_0 represents the kinetic energy of the intermediate states. The phase-shifts for a given partial wave can be calculated from the on-shell matrix element of R , which is obtained by setting $q = q' = q_0$ with $\omega = q_0^2/m_n$, m_n being the mass of the nucleon. Since all of the above interactions reproduce the same phase-shifts, the corresponding on-shell matrix elements of R calculated from these various potentials are identical as well. However, due to the way the potentials are constructed, their off-shell properties may be different. This was discussed in detail in Refs. [41,42]. In those works the authors showed that especially for the 1S_0 and 3S_1 – 3D_1 channels, the CD-Bonn and Nijm-I interactions which include the effects of non-localities, yield a more attractive interaction for the free scattering case. For D -waves and higher partial waves the various potentials were almost equal while there were still differences for P -waves.

We now turn the attention to the application of such NN interactions in a nuclear medium. First we will therefore employ a as simple as possible many-body scheme, in order to preserve a link between the preceding discussion on the NN interaction and the solution of the Lippmann–Schwinger equation. As stated above, it will thus suffice to employ the BHF method.

Following the conventional many-body approach, we divide the full Hamiltonian $H = T + V$, with T being the kinetic energy and V the bare NN interaction, into an unperturbed part $H_0 = T + U$ and an interacting part $H_I = V - U$, such that

$$H = T + V = H_0 + H_I ,$$

where we have introduced an auxiliary single-particle (sp) potential U . If U is chosen such that H_I becomes small, then perturbative many-body techniques can presumably be applied. A serious obstacle to any perturbative treatment is the fact that the bare NN interaction V is very large at short inter-nucleonic distances, which renders a perturbative approach highly prohibitive. To overcome this problem, we introduce the reaction matrix G given by the solution of the Bethe–Goldstone equation (in operator form)

$$G(\omega) = V + VQ[1/(\omega - QH_0Q)]QG , \quad (21)$$

where ω is the unperturbed energy of the interacting nucleons and Q is the Pauli operator which prevents scattering into occupied states. The Pauli operator is given by

$$Q(k_m\tau_m, k_n\tau_n) = \begin{cases} 1, & k_m > k_F^{\tau_m}, k_n > k_F^{\tau_n}, \\ 0 & \text{otherwise,} \end{cases} \quad (22)$$

in the laboratory system, where $k_F^{\tau_i}$ defines the Fermi momenta of the proton ($\tau_i = \frac{1}{2}$) and neutron ($\tau_i = -\frac{1}{2}$). For notational economy, we set $|\mathbf{k}_m| = k_m$.

The above expression for the Pauli operator is in the laboratory frame. In the calculations of the G -matrix, we will employ a Pauli operator in the center-of-mass and relative coordinate system. Further, this Pauli operator will be given by the so-called angle-average approximation, for details see Ref. [43]. Eq. (21) reads then (in a partial wave representation)

$$G_{ll'}^{\alpha T_z}(kk'K\omega) = V_{ll'}^{\alpha T_z}(kk') + \sum_{l''} \int \frac{d^3q}{(2\pi)^3} V_{ll''}^{\alpha T_z}(kq) \frac{Q^{T_z}(q, K)}{\omega - H_0} G_{l'l''}^{\alpha T_z}(qk'K\omega) . \quad (23)$$

The variable K is the momentum of the center-of-mass motion. Since we are going to use an angular average for the Pauli operator, the G -matrix is diagonal in total angular momentum J . Further, the G -matrix is diagonal in the center-of-mass orbital momentum L and the total spin S , all three variables represented by the index α . The variable α differs therefore from the definition of the R -matrix, where $K = 0$. Three different G -matrices have to be evaluated, depending on the individual isospins ($\tau_1 \tau_2$) of the interacting nucleons ($\frac{1}{2} \frac{1}{2}$, $-\frac{1}{2} -\frac{1}{2}$ and $-\frac{1}{2} \frac{1}{2}$). These quantities are represented by the total isospin projection T_z in Eq. (23). The different G -matrices originate from the discrimination between protons and neutrons in Eq. (22). The term H_0 in the denominator of Eq. (23) is the unperturbed energy of the intermediate states and depends on k, K and the individual isospin of the interacting particles. Only ladder diagrams with intermediate two-particle states are included in Eq. (21). The structure of the G -matrix equation in Eq. (23) can then be directly compared to the R -matrix for free NN scattering, Eq. (20). Therefore, as discussed below, eventual differences between various potentials in a finite medium should be easily retraced to the structure of the R -matrix. It is also obvious that one expects the matrix elements of G to be rather close to

those of R with only small deviations. These deviations originate from two effects which reduce the contributions of second and higher order in V to the G -matrix as compared to their contributions to R . One is the above-mentioned Pauli quenching effect: the Pauli operator Q in Eq. (23) restricts the intermediate particle states to states above the Fermi energy. The second one is the dispersive effect: the energy denominators in Eq. (23) are defined in terms of the single-particle energies of nucleons in the medium while the corresponding denominators of Eq. (20) are differences between the energies of free nucleons. Since the absolute values for the energy differences between nucleons, which feel the mean field of the nuclear system, are larger than the energy differences between the kinetic energies, also this dispersive correction reduces the attractive contributions of the non-Born terms. As a result, the matrix elements of G tend to be less attractive than the corresponding matrix elements of R , see e.g. Refs. [41,42] for further details.

We use a continuous single-particle (sp) spectrum advocated by Mahaux et al. [44]. It is defined by the self-consistent solution of the following equations:

$$\varepsilon_i = t_i + u_i = (k_i^2/2m) + u_i, \quad (24)$$

where m is the bare nucleon mass, and

$$u_i = \sum_{h \leq k_F} \langle ih | G(E = \varepsilon_i + \varepsilon_h) | ih \rangle_{AS}. \quad (25)$$

In Eqs. (24) and (25), the subscripts i and h represent the quantum numbers of the single-particle states, such as isospin projections τ_i and τ_h , momenta k_i and k_h , etc. The sp kinetic energy is given by t_i and similarly the sp potential by u_i .

Finally, the non-relativistic energy per nucleon \mathcal{E} is formally given as

$$\mathcal{E} = \frac{1}{A} \sum_{h \leq k_F} \frac{k_h^2}{2m} + \frac{1}{2A} \sum_{h \leq k_F, h' \leq k_F} \langle hh' | G(E = \varepsilon_h + \varepsilon_{h'}) | hh' \rangle_{AS}. \quad (26)$$

In this equation we have suppressed the isospin indices for the Fermi momenta. Eq. (26) is actually calculated for various proton fractions x_p , and is thereby a function of both density n and x_p . We will therefore in the following discussion always label the energy per particle as $\mathcal{E}(n, x_p)$.

In the limit of pure neutron matter only those partial waves contribute where the pair of interacting nucleons is coupled to isospin $T = 1$. Due to the antisymmetry of the matrix elements this implies that only partial waves with even values for the sum $l + S$, like 1S_0 , 3P_0 , etc. need to be considered in this case. For proton fractions different from zero, in particular the case of symmetric nuclear matter, also the other partial waves, like 3S_1 – 3D_1 and 1P_1 contribute. In a BHF calculation the kinetic energy is independent of the NN interaction chosen. We will then restrict the following discussion to the potential energy per nucleon \mathcal{U} , the second term in the RHS of Eq. (26). Putting the contributions from various channels together,³ one obtains the total potential energy per nucleon \mathcal{U} for symmetric nuclear matter and neutron matter. These results are displayed in

³ In our calculations we include all partial waves with $l < 10$.

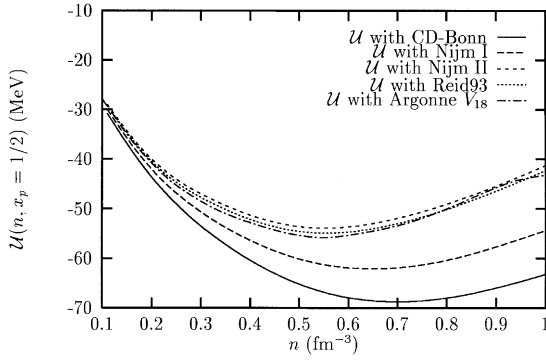


Fig. 2. Potential energy per particle \mathcal{U} for symmetric nuclear matter as function of total baryonic density n .

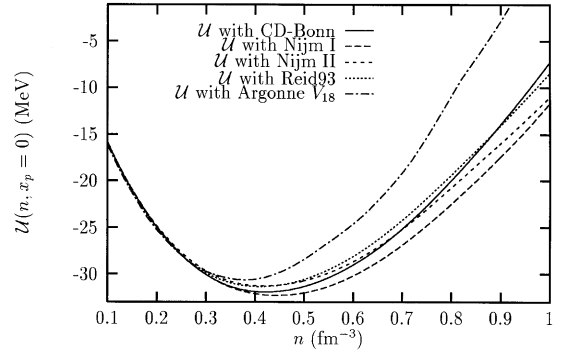
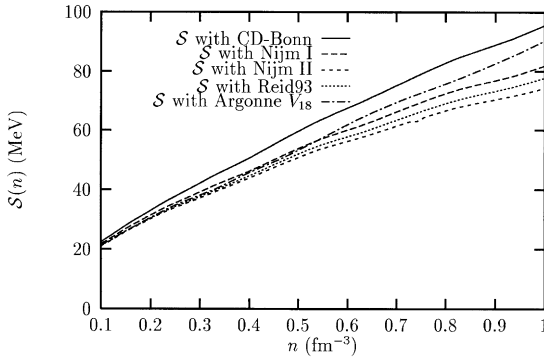
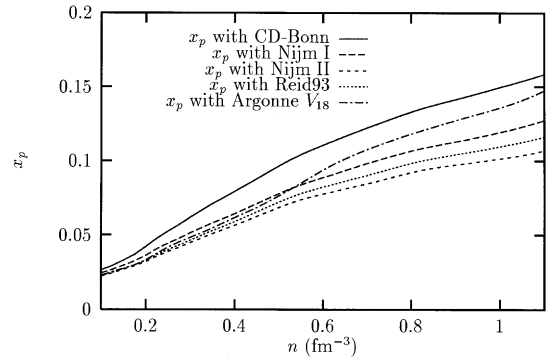
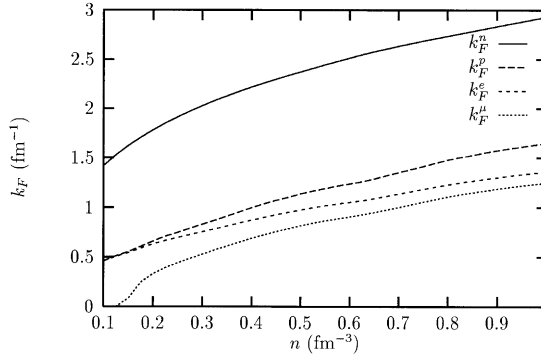


Fig. 3. Potential energy per particle \mathcal{U} for pure neutron matter.

Figs. 2 and 3 as functions of density n for the CD-Bonn interaction [39] (solid line), the three Nijmegen potentials, Nijm-I (long dashes), Nijm-II (short dashes) and Reid93 (dotted line) [37] and the Argonne V_{18} [38] (dot-dashed line).

The differences between the various potentials are larger for the energy in nuclear matter. This is mainly due to the importance of the 3S_1 – 3D_1 contribution which is absent in pure neutron matter. This is in line with previous investigations, which showed that the predicted binding energy of nuclear matter is correlated with the strength of the tensor force, expressed in terms of the D -state probability obtained for the deuteron (see e.g. [43]). This importance of the strength of the tensor force is also seen in the calculation of the binding energy of the triton in Refs. [39,45]. The CD-Bonn interaction yields a binding energy of 8.00 MeV, the Nijm-I potential gives 7.72 MeV while the Nijm-II yields 7.62 MeV, the same as does the new Argonne potential [38]. The experimental value is 8.48 MeV. Typically, potentials with a smaller D -state probability have a weaker tensor force and exhibit therefore a smaller quenching of the non-born terms in Eq. (23). Moreover, the fact that the CD-Bonn interaction and the Nijm I potential include effects of non-localities, yields also a further attraction from the central force both in the 3S_1 – 3D_1 and the singlet 1S_0 channels. The latter explains the additional difference in nuclear matter between the Nijm I and the Nijm II, Reid93 and Argonne V_{18} potentials as well as part of the difference seen in Fig. 3 for pure neutron matter (PNM). For both SNM and PNM there are also additional differences arising from P waves, notably for the Argonne potential in PNM, where the difference between the Argonne V_{18} interaction, the Reid93 and the Nijm II potentials is mainly due to more repulsive contributions from P -waves. For higher partial waves, the differences are rather small, typically of the order of few per cent. The differences seen in Figs. 2 and 3 should also be reflected in the symmetry energy defined in Eq. (14). This is seen in Fig. 4 where we display the symmetry energy for the above potentials as function of density n . From the differences in symmetry energies one would then expect that properties like proton fractions in β -stable matter will be influenced. This in turn has important consequences for the composition of matter in a neutron star and thereby eventual phases present in dense matter. In Fig. 5 we display the corresponding proton

Fig. 4. Symmetry energy \mathcal{S} as function of density n .Fig. 5. Proton fraction x_p for β -stable matter as function of density n .Fig. 6. Fermi momenta for neutrons, protons, electrons and muons in β -stable matter with the CD-Bonn interaction.

fractions obtained by calculating the energy per particle through the G -matrix of Eq. (23) and imposing the equilibrium conditions of Eq. (6) and including muons, see again Ref. [46] for further details. From Fig. 5 one notices that the potential with the largest symmetry energy, the CD-Bonn interaction, is also the one which gives the largest proton fractions. This means in turn that the so-called direct Urca process can occur at lower densities. For the CD-Bonn interaction this happens at 0.88 fm^{-3} , for the Nijm I it starts at 1.25 fm^{-3} while for the Reid93 interaction one reaches the critical density at 1.36 fm^{-3} . The Argonne potential allows for the direct Urca process at a density of 1.05 fm^{-3} . For the Nijm II we were not able to get the direct Urca process for densities below 1.5 fm^{-3} .

It is also interesting to notice that the symmetry energy increases rather monotonously for all potentials. This means that the higher-order derivatives in Eq. (15) can be neglected and that we can, to a good approximation, associate the second derivative $d^2\mathcal{E}/dx_p^2$ with the symmetry energy $\mathcal{S}(n)$ in the empirical mass formula. With this in mind, one can calculate the proton fraction

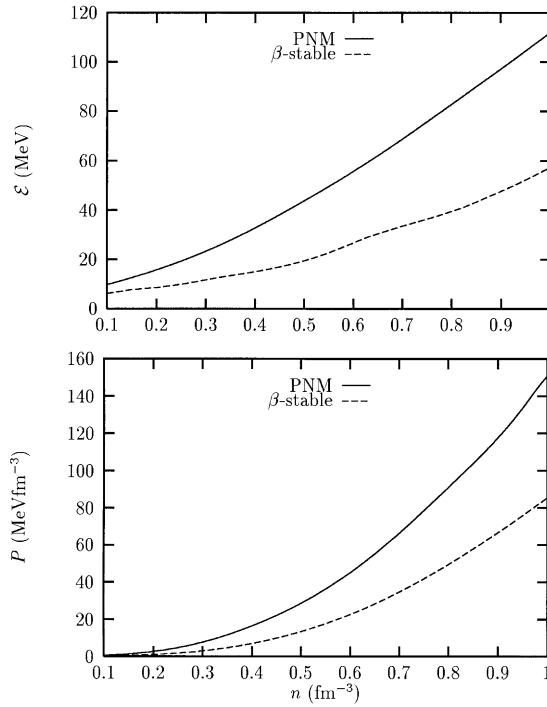


Fig. 7. Upper panel: BHF energy per nucleon for pure neutron matter and β -stable matter obtained with the CD-Bonn interaction. Lower panel: the corresponding pressure P .

employing the theoretically derived symmetry energy shown in Fig. 4 using the simple formula of Eq. (16). A good agreement is in general obtained with the above simple formula, see e.g. Ref. [46] and the parametrization in Section 2.3.

With the results for the proton fractions of Fig. 5 in mind, we plot in Fig. 6 the Fermi momenta for electrons, muons and nucleons obtained with the CD-Bonn interaction, the other potentials yield qualitatively similar results although the proton fraction is slightly smaller. From this figure one notices that muons appear at a density close to the saturation density of nuclear matter, as expected. This can easily be seen if one were to calculate β -stable matter with non-interacting particles only, see e.g. Ref. [47].

Of further interest is the difference in energy per particle $\mathcal{E}(n, x_p)$ for pure neutron matter (PNM) and matter in β -equilibrium. In Fig. 7 we display $\mathcal{E}(n, x_p)$ for PNM and β -stable matter for results with the CD-Bonn interaction only since the other potentials yield qualitatively similar results. Obviously, as seen from Fig. 7 the energy per particle for β -stable matter yields a softer EoS, since the repulsive energy per particle in PNM receives attractive contributions from the $T_z = 0$ channel. This is reflected in the corresponding pressure as well (lower panel of the same figure) and will in turn result in neutron stars with smaller total masses compared with the PNM case.

We end this subsection by plotting in Fig. 8 the energy density per baryon \mathcal{E} (including the contribution from leptons) for β -stable matter. Since the proton fractions are not too large, see Fig. 5, the most important contribution to ε and \mathcal{E} stems from the $T_z = -1$ channel and the

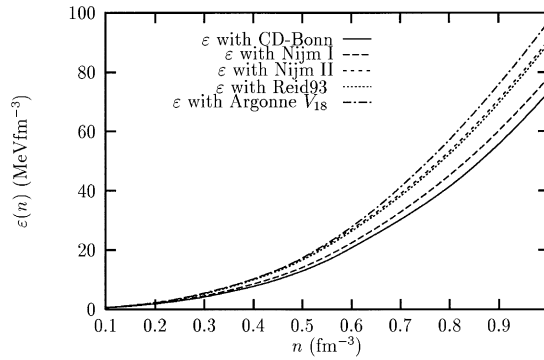


Fig. 8. The total energy in β -stable matter as function of density n . Contributions from leptons are included.

contribution from the nuclear tensor force, especially via the 3S_1 and 3S_1 – 3D_1 contributions with $T_z = 0$, plays a less significant role than what seen for the potential energy in symmetric nuclear matter in Fig. 2. Thus, the main contribution to the differences between the various potentials arises from the $T_z = 1$ channel. For the $T_z = 1$ channel, the new potentials yield also results for β -stable matter in close agreement.

It is thus gratifying that the new NN interactions yield similar energies per particle in neutron star matter. As we will see in the next subsection also, more sophisticated many-body calculations at the two-body level yield rather similar results for neutron matter, since the strong nuclear tensor force in the $T_z = 0$ channel is not present in pure neutron matter or in a less important way in β -stable matter. However, contributions coming from real three-body interaction or relativistic effects, may alter this picture. This is the topic of the next two subsections.

2.2.2. Higher-order many-body calculations

The previous subsection served to establish the connection between the nucleon–nucleon interaction and the simplest many-body approach possible, namely the summation of so-called ladder diagrams by the Brueckner–Hartree–Fock (BHF) method. We will label these calculations as lowest-order Brueckner (LOB) theory. This allowed us to see how the free NN interaction gets modified in a nuclear medium. Eventual differences in, for example, the EoS for neutron star matter could then be retraced to properties of the various NN interactions. The new high-quality NN interactions have also narrowed the differences at higher densities observed in the literature for older interaction models, see e.g. the discussion in Ref. [41]. However, it is well-known that the BHF method in its simplest form is not fully appropriate for a description of dense matter. More complicated many-body terms arising from core-polarization effects, effective three-body and many-body diagrams and eventually the inclusion of three-body forces are expected to be important at densities above n_0 . Moreover, LOB theory suffers from other pathologies like the lack of conservation of number of particles [48]. The need to include e.g. three-body interactions is seen already at the level of the triton since all the above potentials underbind the triton, albeit the discrepancies which existed earlier have been reduced. To give an example, the old Reid potential [49] gave a binding energy of -7.35 MeV while a precursor to the CD–Bonn interaction, the

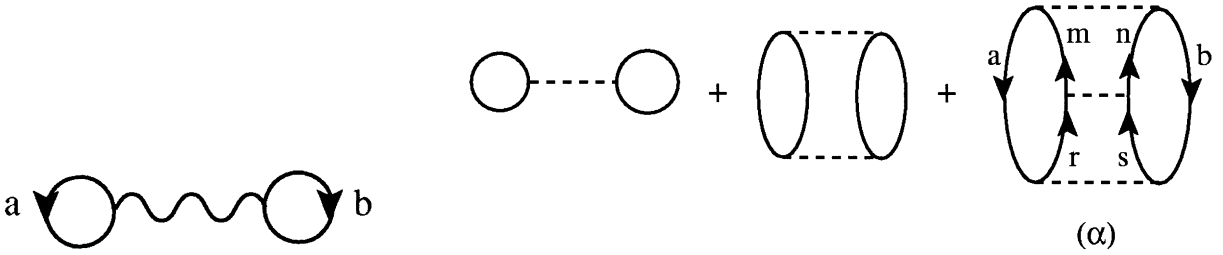


Fig. 9. First-order contribution to the ground-state energy shift ΔE_0 in BHF theory.

Fig. 10. Goldstone diagrams contained in the Brueckner–Hartree–Fock G -matrix.

Bonn A interaction [40] resulted in -8.35 MeV. The modern potentials yield results in a range from -7.6 to -8.0 MeV.

Here we will therefore review three possible improvements to LOB theory and discuss the resulting equations of state in detail. The first improvement will be to consider the summation to infinite order of the chain of particle–particle hole–hole diagrams (PPHH) [50–53]. Thereafter, we will discuss the recent three-hole line results of Baldo and co-workers [54–56] and finally the calculations with three-body forces as well by Akmal et al. [13,14].

In brief, the summation of PPHH diagrams means that the Pauli operator in Eq. (22) is extended in order to prevent scattering into intermediate hole–hole states as well. This means that in addition to summing up to infinite-order diagrams with particle–particle intermediate states, we will now sum, still to infinite order, a larger class of diagrams containing hole–hole intermediate states as well.

For LOB, as discussed in the previous subsection, the effective two-body interaction in nuclear matter is given by the G -matrix, which includes all ladder-type diagrams with particle–particle intermediate states to infinite order. The ground-state energy shift ΔE_0 in terms of the G -matrix is represented by the first-order diagram of Fig. 9 and reads

$$\Delta E_0^{\text{LOB}} = \sum_{ab} n_a n_b \langle ab | G(\omega = \varepsilon_a + \varepsilon_b) | ab \rangle. \quad (27)$$

In Eq. (27) the n 's are the unperturbed Fermi–Dirac distribution functions, namely $n_k = 1$ if $k \leq k_F$ and $= 0$ if $k > k_F$ where k_F is the Fermi momentum.

The Brueckner–Hartree–Fock G -matrix contains repeated interactions between a pair of “particle” lines, as illustrated by the diagrams of Fig. 10. Note that they are so-called Goldstone diagrams, with an explicit time ordering. The third-order diagram (α) of Fig. 10 is given by

$$\text{Diag.}(\alpha) = \left(\frac{1}{2}\right)^3 \frac{V_{abmn} V_{mnr s} V_{rsab}}{(\varepsilon_a + \varepsilon_b - \varepsilon_m - \varepsilon_n)(\varepsilon_a + \varepsilon_b - \varepsilon_r - \varepsilon_s)}. \quad (28)$$

Here m, n, r, s are all particle lines, and V_{ijkl} represents the anti-symmetrized matrix elements of the NN interaction V .

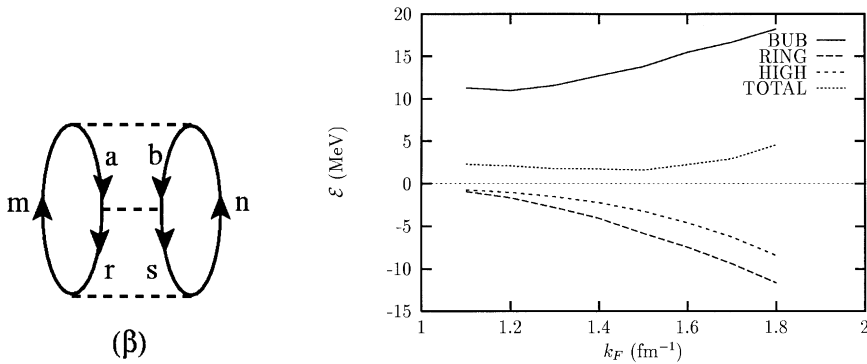


Fig. 11. Goldstone diagram with repeated interactions between hole lines.

Fig. 12. The contributions from the bubble (BUB), ring (RING), and higher-order three hole-line diagrams (HIGH) employing the continuous choice. Results are for symmetric nuclear matter, employing the Argonne V_{14} model for the NN interaction.

To the same order, there is also a diagram with hole–hole interactions, as shown by diagram (β) in Fig. 11, where a, b, r, s are all hole lines. This diagram is not included in standard LOB calculations of nuclear matter, for the following reason. In earlier times, nuclear-matter calculations were based on, by and large, the so-called hole-line-expansion. The essence of the hole-line approach is that diagrams with $(n + 1)$ hole lines are generally much smaller than those with n hole lines. With this criterion, diagram (β) which has 3 (independent) hole lines would be negligible compared with diagram (α) which has 2 hole lines. Thus the former could be neglected. To investigate the validity of this criterion, it may be useful to actually calculate diagrams like (β).

A motivation behind the PPHH-diagram method of nuclear matter is thus to include diagrams with hole–hole correlations like diagram (β) to infinite order. For further details on how to obtain an effective interaction and the energy per particle in neutron star matter, see e.g. Refs. [51,53,57].

The next set of diagrams which can be included is the summation of so-called three-hole line diagrams through the solution of the Bethe–Fadeev equations, originally pioneered by Day [58] and recently taken up again by Baldo and co-workers [54,55]. The whole set of three hole-line diagrams can be grouped into three main sets of diagrams. The so-called ring diagrams, the bubble diagram, and the so-called higher-order diagrams, with an arbitrary number of particle lines. Each of these three-hole line contributions are quite large, see Refs. [54,55] and Fig. 12, but there is a strong degree of cancellation among the various terms. Thus, the total three-hole line contribution turns out to be substantially smaller than the two-body (i.e. two hole-line) contribution. This can be seen in Fig. 12 where we plot the various three hole-line contributions and their total contribution, all with the continuous choice for the single-particle energies. The interesting feature of the calculations of Baldo et al. [55], is that the results with the continuous single-particle choice lead to three hole-line results which are rather close to the total two hole-line results. Diagrams of the PPHH type are however not included. In Ref. [59] these were estimated to be of the same sign in both the standard and the continuum choice. In spite of this methodological progress in perturbative approaches, there are still classes of diagrams which need to be summed up. As

discussed by Jackson in Ref. [60], one can prove that there is a minimal set of diagrams which need to be summed up in order to get the physics of a many-body system right. This set of diagrams is the so-called Parquet class of diagrams [61] where ring diagrams and ladder diagrams are summed up to all orders in a self-consistent way. Since it is rather hard to sum this set of diagrams in a practical way, other many-body methods like the coupled-cluster ansatz [62] and optimized hypernetted-chain theory [63] provide a systematic approximation method to sets of Feynman diagrams that cannot be calculated exactly. In the remainder of this section we will therefore focus on a variational method based on the hypernetted chain summation techniques developed by Pandharipande, Wiringa and co-workers. The approach was developed in the 1970s [64], particularly to include the effects of many-body correlations, presumably important in dense neutron star matter. Calculations performed since then have confirmed that many-body clusters make significant contributions to the binding energies of equilibrium nuclear matter and light nuclei [58,64–67]. We will base our discussion of the EoS on the recent results of Akmal, Pandharipande and Ravenhall [13,14,68]. We will refer the reader to the latter references and Ref. [64] for more details. In brief, the variational wavefunction has the form

$$\Psi_v = \left(S \prod_{i < j} F_{ij} \right) \Phi, \quad (29)$$

consisting of a symmetrized product of pair correlation operators F_{ij} operating on the Fermi gas wavefunction Φ . In symmetric nuclear matter, the function F_{ij} includes eight terms:

$$F_{ij} = \sum_{p=1,8} f^p(r_{ij}) O_{ij}^p, \quad (30)$$

representing central, spin–spin, tensor and spin–orbit correlations with and without isospin factors. In pure neutron matter, the F_{ij} reduce to a sum of four terms with only odd $p \leq 7$. The correlation operators F_{ij} are determined from Euler–Lagrange equations [69] that minimize the two-body cluster contribution of an interaction $(V - \lambda)$, where

$$V_{ij} = \sum_{p=1,14} \alpha^p V^p(r_{ij}) O_{ij}^p, \quad (31)$$

$$\lambda_{ij} = \sum_{p=1,8} \lambda^p(r_{ij}) O_{ij}^p. \quad (32)$$

The variational parameters α^p are meant to simulate the quenching of the spin–isospin interaction between particles i and j , due to flipping of the spin and/or isospin of particle i or j via interaction with other particles in matter. The NN interaction used in Refs. [13,14,68] is the recent parametrization of the Argonne group, the so-called Argonne V_{18} two-nucleon interaction discussed above. It has the form

$$V_{18,ij} = \sum_{p=1,18} V^p(r_{ij}) O_{ij}^p + V_{em}. \quad (33)$$

The electromagnetic part V_{em} consists of Coulomb and magnetic interactions in the nn , np and pp pairs, and it is omitted from all nuclear matter studies. The strong interaction part of the potential includes fourteen isoscalar terms with operators among these the central, spin–spin, spin–orbit and tensor operators. In addition, a phenomenological three-body force V_{ijk} is included, represented by the Urbana models of V_{ijk} containing two isoscalar terms:

$$V_{ijk} = V_{ijk}^{2\pi} + V_{ijk}^R . \quad (34)$$

The first term represents the Fujita–Miyazawa two-pion exchange interaction:

$$V_{ijk}^{2\pi} = \sum_{cyc} A_{2\pi} (\{\tau_i \cdot \tau_j, \tau_i \cdot \tau_k\} \{X_{ij}, X_{ik}\} + \frac{1}{4} [\tau_i \cdot \tau_j, \tau_i \cdot \tau_k] [X_{ij}, X_{ik}]) , \quad (35)$$

$$X_{ij} = S_{ij} T_{\pi}(r_{ij}) + \sigma_i \cdot \sigma_j Y_{\pi}(r_{ij}) , \quad (36)$$

with strength $A_{2\pi}$ and where the matrices σ and τ are the Pauli matrices for spin and isospin, respectively. The functions $T_{\pi}(r_{ij})$ and $Y_{\pi}(r_{ij})$ describe the radial shapes of the one-pion exchange tensor and Yukawa potentials. These functions are calculated using the average value of the pion mass and include the short-range cutoffs used in the Argonne V_{18} NN interaction. The term denoted by V_{ijk}^R is purely phenomenological, and has the form

$$V_{ijk}^R = U_0 \sum_{cyc} T_{\pi}^2(r_{ij}) T_{\pi}^2(r_{ik}) . \quad (37)$$

This term is meant to represent the modification of NA - and ΔA -contributions in the two-body interaction by other particles in the medium, and also accounts for relativistic effects. The spin–isospin dependence of these effects is neglected. The two parameters $A_{2\pi}$ and U_0 are chosen to yield the observed energy of ${}^3\text{H}$ and the equilibrium density of nuclear matter, $\rho_0 = 0.16 \text{ fm}^{-3}$. Obviously, this fitting procedure will yield different parameters if another NN interaction is employed, e.g. the CD–Bonn interaction since, see discussion above, the various potentials yield slightly different binding energies for ${}^3\text{H}$ at the two-body level. The inclusion of many-body clusters is described in Ref. [64]. Relativistic boost corrections were also evaluated in Refs. [13,14,68] but the latter will be included in our discussion of relativistic effects in Section 2.2.3 below.

In the remainder of this subsection we will henceforth discuss the consequences for the EoS from the above many-body corrections.

In Fig. 13 we plot the results for PNM and SNM obtained with two-body interactions including only PPHH diagrams or higher-order diagrams stemming from the variational cluster approach. It is noteworthy to observe that in PNM the energy per particle up to 2–3 times n_0 is rather similar for all calculations at the two-body level. To a certain extent this is expected since the strong nuclear tensor force contribution from the $T = 0$ channel is absent. This means in turn that more complicated many-body terms are not so important in PNM. We will see this also in connection with the three-hole line discussion below. For symmetric nuclear matter the situation is however different due to the strong tensor force in the np channel, leading to larger higher-order corrections. This is clearly seen in the lower panel of Fig. 13. In e.g. the PPHH calculation, where the correlations are due to hole–hole and particle–particle ladders, the tensor force plays the main role. Again this is similar to the situation for the effective interaction in finite nuclei [43]. There, to e.g. second order in the interaction, diagrams with hole–hole and particle–particle intermediate states

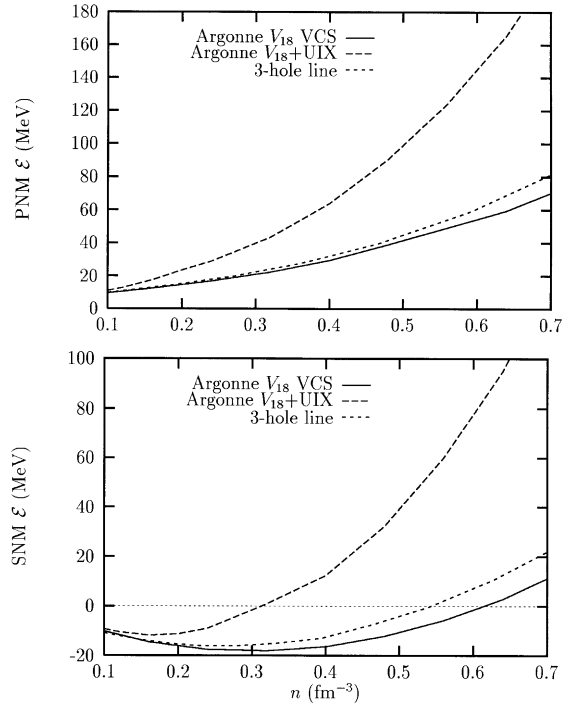
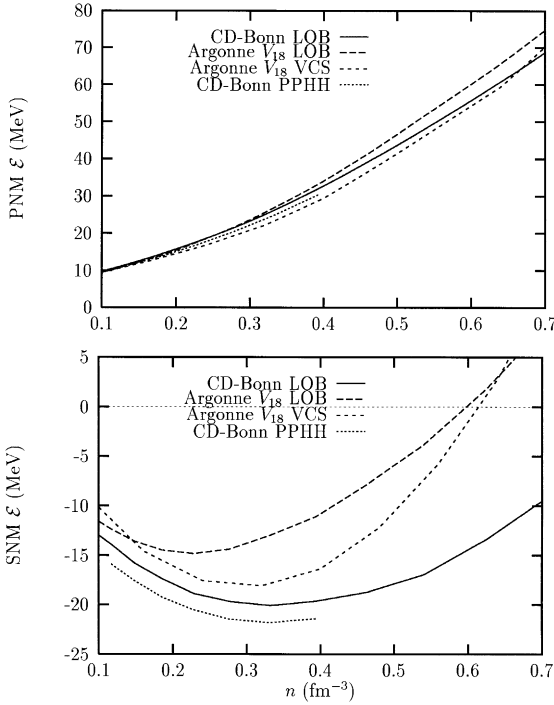


Fig. 13. Upper panel: Energy per particle in PNM for various many-body approaches with two-body interactions only, i.e. PPHH results with the CD-Bonn interaction (stable results were obtained up to densities 0.4 fm^{-3} only), LOB with the Argonne V_{18} interaction and variational cluster (VCS) results for the Argonne V_{18} interaction model. Lower panel: The corresponding results for SNM.

Fig. 14. Upper panel: Energy per particle in PNM for variational calculations with the Argonne V_{18} interaction without (VCS) and with three-body interactions ($V_{18} + \text{UIX}$). The result from the three-hole line expansion of Baldo and co-workers employing the V_{14} interaction is included as well. Lower panel: The corresponding results for SNM.

tend to be bigger than screening diagrams. In general however, none of the calculations at the two-body level reproduce properly the saturation properties of SNM.

In Fig. 14 we have then included results from calculations with effective three-body terms and the phenomenological three-body forces. The results are compared with those from LOB with the Argonne V_{18} interaction. With the inclusion of the phenomenological three-body force described in Eq. (34), which was fitted to reproduce the binding energy of the triton and the alpha particle, a clear change is seen both in PNM and SNM. The energy per particle gets more repulsive at higher densities. Three hole-line diagrams however, with the continuous choice are rather close to LOB with the continuous choice in SNM, while they are almost negligible in PNM, in line with our observation above about the tensor force component in the $T = 0$ channel.

Thus, as a summary, the inclusion of phenomenological three-body forces in non-relativistic calculations are needed in order to improve the saturation properties of the microscopically calculated EoS, whereas the inclusion of additional many-body effects, either three-hole line

diagrams or through VCS calculations yield results at low densities similar to those from LOB. However, even with the three-body force, one is not able to reproduce properly the binding energy. In the next subsection we will thence discuss further corrections stemming from relativistic effects.

2.2.3. *Relativistic effects*

The properties of neutron stars depend on the equation of state at densities up to an order of magnitude higher than those observed in ordinary nuclei. At such densities, relativistic effects certainly prevail. Among relativistic approaches to the nuclear many-body problem, the so-called Dirac–Hartree and Dirac–Hartree–Fock approaches have received much interest [31,70,71]. One of the early successes of these approaches was the quantitative reproduction of spin observables, which are only poorly described by the non-relativistic theory. Important to these methods was the introduction of a strongly attractive scalar component and a repulsive vector component in the nucleon self-energy [72,31]. Inspired by the successes of the Dirac–Hartree–Fock method, a relativistic extension of Brueckner theory was proposed by Celenza and Shakin [73], known as the Dirac–Brueckner theory. One of the appealing features of the Dirac–Brueckner approach is the self-consistent determination of the relativistic sp energies and wave functions. The Dirac–Brueckner approach differs from the Dirac–Hartree–Fock one in the sense that in the former one starts from the free NN interaction which is only constrained by a fit to the NN data, whereas the Dirac–Hartree–Fock method pursues a line where the parameters of the theory are determined so as to reproduce the bulk properties of nuclear matter. It ought, however, to be stressed that the Dirac–Brueckner approach, which starts from NN interactions based on meson exchange, is a non-renormalizable theory where the short-range part of the potential depends on additional parameters like vertex cut-offs, clearly minimizing the sensitivity of calculated results to short-distance inputs, see e.g. Refs. [73–75]. The description presented here for the Dirac–Brueckner approach follows closely that of Brockmann and Machleidt [74]. We will thus use the meson-exchange models of the Bonn group, defined in Table A.2 of Ref. [40]. There the three-dimensional reduction of the Bethe–Salpeter equation as given by the Thompson equation is used to solve the equation for the scattering matrix [76]. Hence, including the necessary medium effects like the Pauli operators discussed in the previous subsection and the starting energy, we shall rewrite Eq. (23) departing from the Thompson equation. Then, in a self-consistent way, we determine the above-mentioned scalar and vector components which define the nucleon self-energy. Note that negative energy solutions are not included. An account of these can be found in the recent work of de Jong and Lenske [77]. In order to introduce the relativistic nomenclature, we consider first the Dirac equation for a free nucleon, i.e.

$$(i\not{\partial} - m)\psi(x) = 0 ,$$

where m is the free nucleon mass and $\psi(x)$ is the nucleon field operator (x is a four-point) which is conventionally expanded in terms of plane wave states and the Dirac spinors $u(p, s)$, and $v(p, s)$, where $p = (p^0, \mathbf{p})$ is a four momentum⁴ and s is the spin projection.

⁴ Further notation is as given in Itzykson and Zuber [78].

The positive energy Dirac spinors are (with $\bar{u}u = 1$)

$$u(p, s) = \sqrt{\frac{E(p) + m}{2m}} \begin{pmatrix} \chi_s \\ \frac{\boldsymbol{\sigma} \cdot \mathbf{p}}{E(p) + m} \chi_s \end{pmatrix}, \quad (38)$$

where χ_s is the Pauli spinor and $E(p) = \sqrt{m^2 + |\mathbf{p}|^2}$. To account for medium modifications to the free Dirac equation, we introduce the notion of the self-energy $\Sigma(p)$. As we assume parity to be a good quantum number, the self-energy of a nucleon can be formally written as

$$\Sigma(p) = \Sigma_S(p) - \gamma_0 \Sigma^0(p) + \gamma \mathbf{p} \Sigma^V(p).$$

The momentum dependence of Σ^0 and Σ_S is rather weak (Serot and Walecka, 1986). Moreover, $\Sigma^V \ll 1$, such that the features of the Dirac–Brueckner–Hartree–Fock procedure can be discussed within the framework of the phenomenological Dirac–Hartree ansatz, i.e. we approximate

$$\Sigma \approx \Sigma_S \gamma_0 \Sigma^0 = U_S + U_V,$$

where U_S is an attractive scalar field, and U_V is the time-like component of a repulsive vector field. The finite self-energy modifies the free Dirac spinors of Eq. (38) as

$$\tilde{u}(p, s) = \sqrt{\frac{\tilde{E}(p) + \tilde{m}}{2\tilde{m}}} \begin{pmatrix} \chi_s \\ \frac{\boldsymbol{\sigma} \cdot \mathbf{p}}{\tilde{E}(p) + \tilde{m}} \chi_s \end{pmatrix},$$

where we let the terms with tilde represent the medium modified quantities. Here we have defined

$$\tilde{m} = m + U_S,$$

and

$$\tilde{E}_i = \tilde{E}(p_i) = \sqrt{\tilde{m}_i^2 + \mathbf{p}_i^2}. \quad (39)$$

As in the previous subsection, the subscripts i , and h below, represent the quantum numbers of the single-particle states, such as isospin projections τ_i and τ_h , momenta k_i and k_h , etc.

The sp energy is

$$\tilde{\epsilon}_i = \tilde{E}_i + U_V^i, \quad (40)$$

and the sp potential is given by the G -matrix as

$$u_i = \sum_{h \leq k_F} \frac{\tilde{m}_i \tilde{m}_h}{\tilde{E}_i \tilde{E}_h} \langle ih | \tilde{G}(\tilde{E} = \tilde{E}_i + \tilde{E}_h) | ih \rangle_{AS}, \quad (41)$$

or, if we wish to express it in terms of the constants U_S and U_V , we have

$$u_i = \frac{\tilde{m}_i}{\tilde{E}_i} U_S^i + U_V^i. \quad (42)$$

In Eq. (41), we have introduced the relativistic \tilde{G} -matrix. If the two interacting particles, with isospins τ_1 and τ_2 , give a total isospin projection T_z , the relativistic \tilde{G} -matrix in a partial wave representation is given by

$$\tilde{G}_{ll'}^{\alpha T_z}(kk'K\tilde{E}) = \tilde{V}_{ll'}^{\alpha T_z}(kk') + \sum_{l''} \int \frac{d^3q}{(2\pi)^3} \tilde{V}_{ll''}^{\alpha T_z}(kq) \frac{\tilde{m}_1 \tilde{m}_2}{\tilde{E}_1^q \tilde{E}_2^q (\tilde{E} - \tilde{E}_1^q - \tilde{E}_2^q)} \tilde{Q}^{T_z}(q, K) \tilde{G}_{l'l''}^{\alpha T_z}(qk'K\tilde{E}) , \quad (43)$$

where the relativistic starting energy is defined according to Eq. (39) as

$$\tilde{E} = \tilde{E}(\sqrt{k^2 + K^2/4}, \tau_1) + \tilde{E}(\sqrt{k^2 + K^2/4}, \tau_2) .$$

and

$$\tilde{E}_{1(2)}^q = \tilde{E}(\sqrt{q^2 + K^2/4}, \tau_{1(2)}) .$$

Eqs. (40)–(43) are solved self-consistently, starting with adequate values for the scalar and vector components U_s and U_v . This iterative scheme is continued until these parameters show little variation. Finally, the relativistic version of Eq. (26) reads

$$\mathcal{E}/A = \frac{1}{A} \sum_{h \leq k_F} \frac{\tilde{m}_h m + k_h^2}{\tilde{E}_h} + \frac{1}{2A} \sum_{h \leq k_F, h' \leq k_F} \frac{\tilde{m}_h \tilde{m}_{h'}}{\tilde{E}_h \tilde{E}_{h'}} \langle hh' | \tilde{G}(\tilde{E} = \tilde{E}_h + \tilde{E}_{h'}) | hh' \rangle_{AS} - m . \quad (44)$$

An alternative approach which we will also discuss is the inclusion of relativistic boost corrections to non-relativistic NN interactions in the VCS calculations of Akmal et al. [14,68]. In all analyses, the NN scattering data are reduced to the center-of-mass frame and fitted using phase shifts calculated from the nucleon–nucleon interaction, V , in that frame. The interaction obtained by this procedure describes the NN interaction in the c.m. frame, in which the total momentum $\mathbf{P}_{ij} = \mathbf{p}_i + \mathbf{p}_j$, is zero. In general, the interaction between particles depends upon their total momentum, and can be written as

$$v(\mathbf{P}_{ij}) = v_{ij} + \delta v(\mathbf{P}_{ij}) , \quad (45)$$

where v_{ij} is the interaction for $\mathbf{P}_{ij} = 0$, and $\delta v(\mathbf{P}_{ij})$ is the boost interaction [79] which is zero when $\mathbf{P}_{ij} = 0$.

Following the work of Krajcik and Foldy [80], Friar [81] obtained the following equation relating the boost interaction of order P^2 to the interaction in the center-of-mass frame:

$$\delta v(\mathbf{P}) = -\frac{P^2}{8m^2}v + \frac{1}{8m^2}[\mathbf{P} \cdot \mathbf{r} \mathbf{P} \cdot \nabla, v] + \frac{1}{8m^2}[(\sigma_i - \sigma_j) \times \mathbf{P} \cdot \nabla, v] . \quad (46)$$

The general validity of this equation in relativistic mechanics and field theory was recently discussed [79]. Incorporating the boost into the interaction yields a non-relativistic Hamiltonian of

the form

$$H_{NR}^* = \sum \frac{p_i^2}{2m} + \sum (v_{ij} + \delta v(\mathbf{P}_{ij})) + \sum V_{ijk}^* + \dots, \quad (47)$$

where the ellipsis denotes the three-body boost, and four and higher body interactions. This H_{NR}^* contains all terms quadratic in the particle velocities, and is therefore suitable for complete studies in the non-relativistic limit.

The authors of Refs. [66,82] find that the contribution of the two-body boost interaction to the energy is repulsive, with a magnitude which is 37% of the V_{ijk}^R contribution. The boost interaction thus accounts for a significant part of the V_{ijk}^R in Hamiltonians which fit nuclear energies neglecting δv .

In this work we will follow Refs. [13,14,68] and only keep the terms of the boost interaction associated with the static part of V , and neglect the last term in Eq. (46). That term is responsible for Thomas precession and quantum contributions that are negligibly small here [83]. The correction δv is then given by

$$\delta v(\mathbf{P}) = -\frac{P^2}{8m^2}v^s + \frac{1}{8m^2}\mathbf{P} \cdot \mathbf{r} \mathbf{P} \cdot \nabla v^s. \quad (48)$$

The two terms are due to the relativistic energy expression and Lorentz contraction, and are denoted δv^{RE} and δv^{LC} , respectively. The three-nucleon interaction used in the H_{NR}^* of Eq. (47) is denoted by V_{ijk}^* . Its parameters are obtained by fitting the binding energies of ^3H and ^4He , and the equilibrium density of SNM, including δv . The strength of V_{ijk}^{R*} is 0.63 times that of V_{ijk}^R in UIX, while that of $V_{ijk}^{2\pi}$ is unchanged. The resulting model of V_{ijk} is called UIX*.

In Fig. 15 we plot the non-relativistic BHF and DBHF energies per particle for both SNM and PNM. These results were discussed in Ref. [46] and were obtained with an older version of the Bonn interactions, namely the so-called Bonn A potential. The relativistic corrections include in an effective way a certain class of three-body corrections, the so-called Z-graphs [84], although the calculations are done only at the two-body level. The non-relativistic results are similar to those obtained with the CD-Bonn interaction discussed in the previous subsection. One notices also that the DBHF results yield saturation properties close to the empirical data, a binding energy of -15.1 MeV and saturation density of 0.19 fm^{-3} , while the non-relativistic results saturate at 0.37 fm^{-3} with a binding energy of -22.4 MeV . For comparison we have also included the results of Akmal et al. [13,14] with three-body diagrams and boost corrections. Again, one notices that at densities below n_0 all many-body schemes tend to give similar results, although in this case, the relativistic results are in better agreement with the results of the full calculation of Akmal et al. [13,14]. For completeness, we display the energy per particle for β -stable matter obtained with the DBHF and the results from the calculations of Akmal et al. [14,68] with boost corrections and three-body forces in Fig. 16. The corresponding proton fractions are also plotted. The dip in the proton fraction of Akmal et al. at $\sim 0.2 \text{ fm}^{-3}$ is due to the formation of a pion condensate. For higher densities we note that BHF and the calculations of Akmal et al. yield rather similar proton fractions. The direct Urca starts only at densities $\sim 1 \text{ fm}^{-3}$, while the DBHF calculations allow the direct Urca at much lower densities.

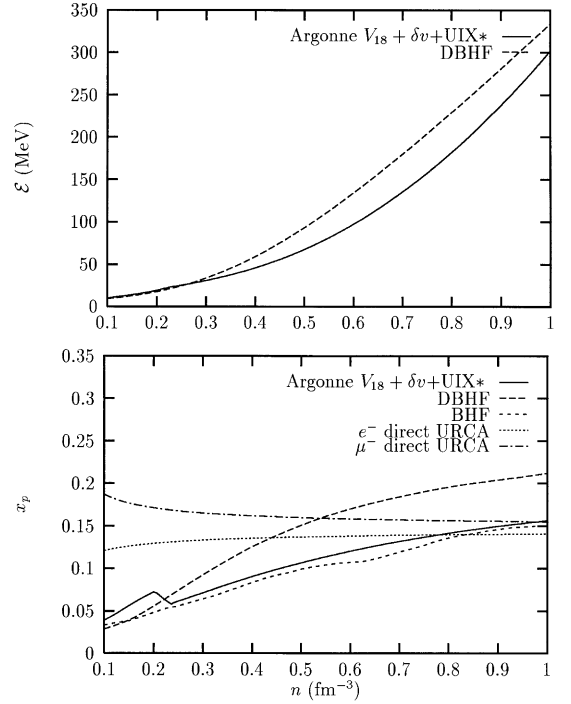
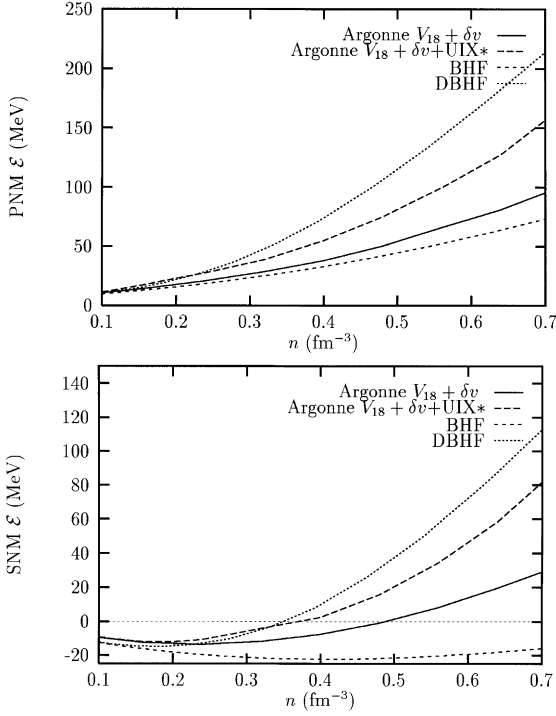


Fig. 15. Upper panel: DBHF and BHF energy per nucleon for PNM. The results with boost corrections of Akmal et al. [14] with $(V_{18} + \delta v + \text{UIX}^*)$ and without $(V_{18} + \delta v)$ three-body forces. Lower panel: the corresponding results for SNM.

Fig. 16. Upper panel: Energy per nucleon in β -stable matter for the DBHF approach and the results of Akmal et al. with boost corrections and three-body forces $(V_{18} + \delta v + \text{UIX}^*)$. Lower panel: the corresponding proton fraction x_p . For the DBHF calculation both electrons and muons are included.

2.3. A causal parametrization of the nuclear matter EoS

Since three-body forces are expected to be important (it suffices to mention studies of the Triton [45]), we will in our discussions of the mixed phase in the next section and in connection with the structure of a neutron star, employ the recent EoS of Akmal et al. [14]. A non-relativistic EoS (although with the inclusion of boost corrections) is preferred here. The EoS for nuclear matter is thus known to some accuracy for densities up to a few times nuclear saturation density, $n_0 = 0.16 \text{ fm}^{-3}$. Detailed knowledge of the EoS is crucial for the existence of, e.g. pion condensates [13,14] or the delicate structures in the inner crust of neutron stars [27]. However, for the gross properties and our discussion of properties of neutron stars we will adopt a simple form for the binding energy per nucleon in nuclear matter consisting of a compressional term and a symmetry term

$$\mathcal{E} = E_{\text{comp}}(n) + S(n)(1 - 2x_p)^2 = \mathcal{E}_0 u \frac{u - 2 - \delta}{1 + \delta u} + S_0 u^2 (1 - 2x_p)^2. \quad (49)$$

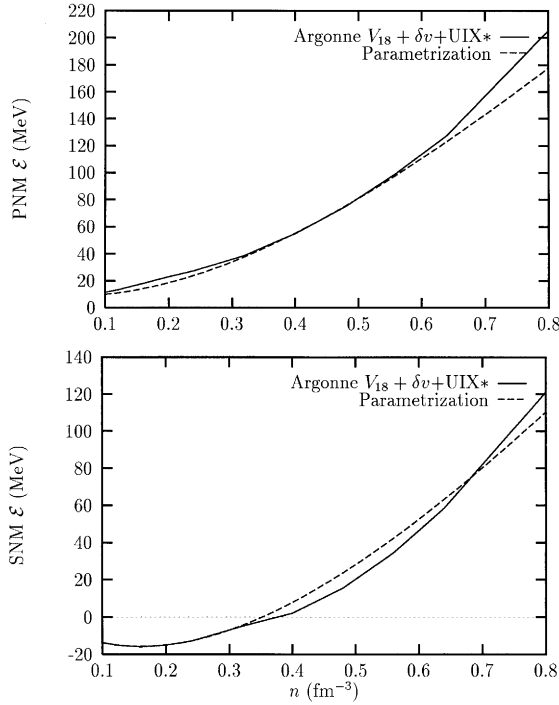


Fig. 17. Upper panel: Comparison of the parametrized EoS of Eq. (49) and the results of Akmal et al. [14] with boost corrections and three-body forces ($V_{18} + \delta v + \text{UIX*}$) for PNM. Lower panel: the corresponding results for SNM.

Here $u = n/n_0$ is the ratio of the baryon density to nuclear saturation density and we have defined the proton fraction $x_p = n_p/n$. The compressional term is in (49) parametrized by a simple form which reproduces the saturation density, binding energy and compressibility. The binding energy per nucleon at saturation density excluding Coulomb energies is $\mathcal{E}_0 = -15.8$ MeV and the parameter $\delta = 0.2$ is determined by fitting the energy per nucleon at high density to the EoS of Akmal et al. [14] with three-body forces and boost corrections, but taking the corrected values from Table 6 of Ref. [14]. The reason behind the choice of $\delta = 0.2$ will be explained below in connection with the discussion of Figs. 18 and 19. Further discussions will be presented in Section 5. The corresponding compressibility is $K_0 = 18\mathcal{E}_0/(1 + \delta) \simeq 200$ MeV in agreement with the experimental value. For the symmetry term we obtain $S_0 = 32$ MeV and $\gamma = 0.6$ for the best fit. The quality of this simple functional exhibits a χ^2 per datum close to 1 and is compared with the results of Akmal et al. [14] for both PNM and SNM in Fig. 17. As can be seen from this figure, the agreement is rather good except at the very high densities where the EoS of Akmal et al. [14] becomes superluminal and therefore anyway must be wrong. A much more sophisticated fit which reproduces the data in terms of Skyrme functional approach is given by the Akmal et al. [14]. However, it is amazing that such a simple quadratic formula fits so well the data coming from a microscopic calculation. In view of the uncertainties which pertain to the EoS at higher densities, we feel that our parametrization is within present error margins. The agreement between the

microscopic calculation of Akmal et al. [14] and the simple parametrization of Eq. (49) may imply that the essential many-body physics close to the equilibrium density arises from two-body and three-body terms to \mathcal{E} only. The reason being⁵ that three-body terms are proportional with n^3 while the two-body terms are proportional with n^2 . With three-body terms we obviously intend both effective interactions and contributions from real three-body forces. The evaluation of the latter is, as discussed above, still an unsettled problem.

If we now restrict the attention to matter with electrons only, one can easily obtain an analytic equation for the proton fraction through the asymmetry parameter x . Recalling the equilibrium conditions for β -stable matter of Eqs. (6) and (7) and using the definitions of the chemical potentials for particle species i of Eq. (3) one finds that

$$\mu_e = (1/n) \partial \varepsilon / \partial x_p , \quad (50)$$

and from the latter it is rather easy to show that the proton fraction is given by (assuming ultra-relativistic electrons)

$$nx_p = \frac{(4S_0 u^\gamma (1 - 2x_p))^3}{3\pi^2} . \quad (51)$$

Defining

$$a = 2(4S_0 u^\gamma)^3 / \pi^2 n , \quad (52)$$

Eq. (51) reduces to

$$3x^3 + ax - a = 0 , \quad (53)$$

where $x = 1 - 2x_p$. Since we will always look at solutions for densities greater than zero, the cubic equation for x has actually an analytical solution which is real and given by

$$x = -2\sqrt{a}/\tan(2\psi) , \quad (54)$$

with $\tan \psi = (\tan \frac{\phi}{2})^{1/3}$ and $\tan \phi = -2\sqrt{a}/3$. Note well that x depends on the total baryon density n only. This means in turn that our parametrization of the EoS can now be rewritten for β -stable matter as

$$\mathcal{E} = \mathcal{E}_0 u \frac{u - 2 - \delta}{1 + \delta u} + S_0 u^\gamma \left(\frac{2\sqrt{a}}{\tan(2\psi)} \right)^2 . \quad (55)$$

and is an analytical function of density only.

The quality of our approximation to the EoS of Akmal et al. [14] for other observables than the energy per particle is shown in Fig. 18 for the proton fractions derived from the simple expression in Eq. (54). In the same figure we display also the resulting energy per nucleon in β -stable matter and compare it with the results of Akmal et al. [14] for various values of δ . Note well that the

⁵ This argument is for the energy density, i.e. $\varepsilon = \mathcal{E}n$.

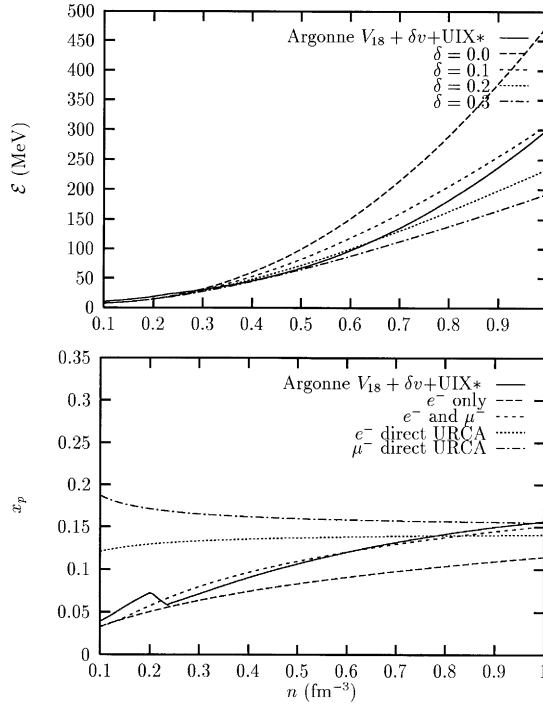


Fig. 18. Upper panel: Energy per nucleon (no leptonic contribution) in β -stable matter for the parametrized EoS of Eq. (49) for $\delta = 0, 0.13, 0.2, 0.3$ and the results of Akmal et al. [14] with boost corrections and three-body forces ($V_{18} + \delta v + \text{UIX}^*$). Lower panel: the corresponding proton fraction x_p .

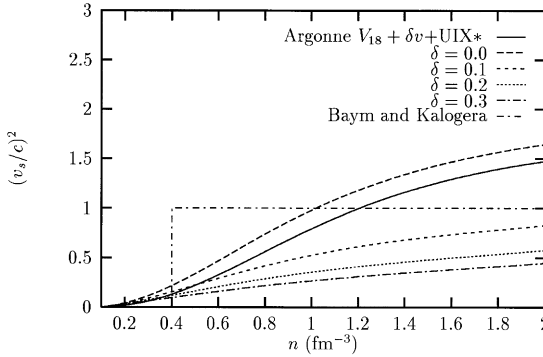


Fig. 19. $(v_s/c)^2$ for $\delta = 0, 0.1, 0.2, 0.3$, the results of Akmal et al. [14], and for Baym and Kalogera's [85] patched EoS which shows a discontinuous $(v_s/c)^2$.

proton fraction does not depend on the value of δ , see Eq. (51). As can be seen from this picture, the EoS with $\delta = 0$ yields the stiffest EoS, and as a consequence it results in a superluminal behavior at densities greater than $n \approx 1.0 \text{ fm}^{-3}$. This is seen in Fig. 19 where we plot the sound speed $(v_s/c)^2$ for various δ values and that resulting from the microscopic calculation of Akmal et al. [14]. The form

of (49), with the inclusion of the parameter δ , provides therefore a smooth extrapolation from small and large densities with the correct behavior in both limits, i.e. the binding energy per nucleon $E/A = \mathcal{E}$ is linear in number density. In the dilute limit this is the Lenz (optical) potential. At high densities the linearity is required by the condition that the sound speed $v_s^2 = \partial P / \partial \varepsilon$ does not exceed the speed of light. This justifies the introduction of the parameter δ in our parametrization and explains also our deviation from the results of Akmal et al. at densities greater than $0.6\text{--}0.7\text{ fm}^{-3}$, see Figs. 17 and 18. For $\delta = 0.1$ the EoS becomes superluminal at densities of the order of 6 fm^{-3} . From the definition of $(v_s/c)^2$ in Eq. (18) and the EoS of Eq. (49) that for

$$\delta \geq \sqrt{\mathcal{E}_0/m_n} \simeq 0.13, \quad (56)$$

the EoS remains causal for all densities. The EoS of Akmal et al. becomes superluminal at $n \approx 1.1\text{ fm}^{-3}$. With this caveat we have an EoS that reproduces the data of Akmal et al. at densities up to $0.6\text{--}0.7\text{ fm}^{-3}$ and has the right causal behavior at higher densities. Furthermore, the differences at higher densities will also not be of importance in our analysis of the dynamics and structure of neutrons stars, since the mixed baryon-quark phase, with realistic values for the bag parameter and the coupling constant α_s starts at densities around $0.5\text{--}0.8\text{ fm}^{-3}$.

Finally, in Fig. 19 we have also plotted the sound speed following the approach of Baym and Kalogera [85], where the sound speed is allowed to jump discontinuously at a chosen density in order to keep the EoS causal. With this prescription, Baym and Kalogera were also able to obtain an upper bound for neutron star masses of $2.9M_\odot$. The approach of Baym and Kalogera differs from ours since their EoS is discontinuously stiffened by taking $v_s = c$ at densities above a certain value n_c which, however, is lower than $n_s = 5n_0$ where their nuclear EoS becomes superluminal. This stiffens the nuclear EoS for densities $n_c < n < n_s$ but softens it at higher densities. Their resulting maximum masses lie in the range $2.2M_\odot < M < 2.9M_\odot$. Our approach incorporates causality by reducing the sound speed smoothly towards the speed of light at high densities. Our approach will most likely not yield an absolute upper bound on the maximum mass of a neutron star. Therefore our maximum mass never exceeds that of nuclear EoS of Akmal et al. [14]. In fact, one may argue that at very high densities particles become relativistic and the sound speed should be even lower, $v_s^2 \simeq c^2/3$, and therefore the softening we get from incorporating causality is even on the low side.

2.4. Hyperonic matter

At nuclear matter density the electron chemical potential is $\sim 110\text{ MeV}$, see e.g. Fig. 6. Once the rest mass of the muon is exceeded, it becomes energetically favorable for an electron at the top of the e^- Fermi surface to decay into a μ^- . We then develop a Fermi sea of degenerate negative muons, see again Fig. 6. In a similar way, as soon as the chemical potential of the neutron becomes sufficiently large, energetic neutrons can decay via weak strangeness non-conserving interactions into Λ hyperons leading to a Λ Fermi sea with $\mu_\Lambda = \mu_n$. However, if we neglect interactions, or assume that their effects are small, one would expect the Σ^- to appear via

$$e^- + n \rightarrow \Sigma^- + \nu_e, \quad (57)$$

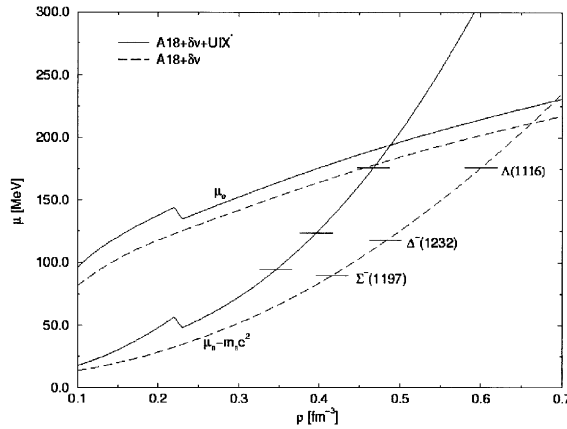


Fig. 20. The neutron and electron chemical potentials in beta stable matter according to models $V_{18} + \delta v + \text{UIX}^*$ (full line) and $V_{18} + \delta v$ (dashed line). Threshold densities for the appearance of non-interacting hyperons are marked by horizontal line segments. Taken from Ref. [14].

at lower densities than the Λ , even though Σ^- is more massive the reason being that the above process removes both an energetic neutron and an energetic electron, whereas the decay to a Λ , being neutral, removes only an energetic neutron. Stated differently, the negatively charged hyperons appear in the ground state of matter when their masses equal $\mu_e + \mu_n$, while the neutral hyperon Λ appears when μ_n equals its mass. Since the electron chemical potential in matter is larger than the mass difference $m_{\Sigma^-} - m_{\Lambda} = 81.76$ MeV, the Σ^- will appear at lower densities than the Λ . We show this in Fig. 20 where we plot the chemical potentials for electrons and neutrons in β -stable matter. The threshold densities for Σ^- , Λ and the isobar Δ^- are indicated by the horizontal lines.

Since this work has an emphasis on many-body approaches, we will try to delineate here as well how to obtain properties of hyperons in dense nuclear matter within the framework of microscopic theories. The main problem we have to face in our case is that the hyperon–nucleon interaction and especially the hyperon–hyperon interaction are less constrained by the data as is the case in the nucleonic sector. Our many-body scheme starts thus with the most recent parametrization of the free baryon–baryon potentials for the complete baryon octet as defined by Stoks and Rijken in Ref. [19]. This potential model, which aims at describing all interaction channels with strangeness from $S = 0$ to $S = -4$, is based on SU(3) extensions of the Nijmegen potential models [86] for the $S = 0$ and $S = -1$ channels, which are fitted to the available body of experimental data and constrain all free parameters in the model. In our discussion we employ the interaction version NSC97e of Ref. [19], although we have also carried out calculations with version NSC97a. Since the results for β -stable matter are not significantly altered, we will present results with version NSC97e only.

The next step is to introduce effects from the nuclear medium. Here we will construct the G -matrix, which takes into account short-range correlations for all strangeness sectors, and solve the equations for the single-particle energies of the various baryons self-consistently. The G -matrix

is formally given by

$$\begin{aligned} \langle B_1 B_2 | G(\omega) | B_3 B_4 \rangle &= \langle B_1 B_2 | V | B_3 B_4 \rangle \\ &+ \sum_{B_5 B_6} \langle B_1 B_2 | V | B_5 B_6 \rangle \frac{1}{\omega - \varepsilon_{B_5} - \varepsilon_{B_6} + i\eta} \langle B_5 B_6 | G(\omega) | B_3 B_4 \rangle . \end{aligned} \quad (58)$$

Here B_i represents all possible baryons $n, p, \Lambda, \Sigma^-, \Sigma^0, \Sigma^+, \Xi^-, \Xi^0$ and their quantum numbers such as spin, isospin, strangeness, linear momenta and orbital momenta. The intermediate states $B_5 B_6$ are those which are allowed by the Pauli principle and the energy variable ω is the starting energy defined by the single-particle energies of the incoming external particles $B_3 B_4$. The G -matrix is solved using relative and centre-of-mass coordinates, see e.g., Refs. [20,89] for computational details. The single-particle energies are given by

$$\varepsilon_{B_i} = t_{B_i} + u_{B_i} + m_{B_i} \quad (59)$$

where t_{B_i} is the kinetic energy and m_{B_i} the mass of baryon B_i . The single-particle potential u_{B_i} is defined by

$$u_{B_i} = \text{Re} \sum_{B_j \leq F_j} \langle B_i B_j | G(\omega = \varepsilon_{B_j} + \varepsilon_{B_i}) | B_i B_j \rangle . \quad (60)$$

The linear momentum of the intermediate single-particle state B_j is limited by the size of the Fermi surface F_j for particle species B_j . The last equation is displayed in terms of Goldstone diagrams in Fig. 21. Diagram (a) represents contributions from nucleons only as hole states, while diagram (b) has only hyperons as hole states in case we have a finite hyperon fraction in β -stable neutron star matter. The external legs represent nucleons and hyperons.

In order to satisfy the equations for β -stable matter summarized in Eq. (10), we need to solve Eqs. (58) and (59) to obtain the single-particle energies of the particles involved at the corresponding Fermi momenta. Typically, for every total baryonic density $n = n_N + n_Y$, the density of nucleons plus hyperons, Eqs. (58) and (59) were solved for five nucleon fractions and five hyperons fractions and, for every nucleon and hyperon fraction, we computed three proton fractions and three fractions for the relevant hyperons. The set of equations in Eq. (10) were then solved by interpolating between different nucleon and hyperon fractions.

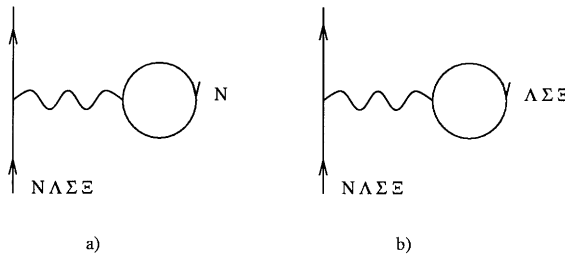


Fig. 21. Goldstone diagrams for the single-particle potential u . (a) represents the contribution from nucleons only as hole states while (b) includes only hyperons as hole states. The wavy line represents the G -matrix.

The many-body approach outlined above is the lowest-order Brueckner–Hartree–Fock (BHF) method extended to the hyperon sector. This means also that we consider only two-body interactions. However, it is well-known from studies of nuclear matter and neutron star matter with nucleonic degrees of freedom only that three-body forces are important in order to reproduce the saturation properties of nuclear matter, see e.g., Ref. [14] for the most recent approach. In order to include such effects, we replace the contributions to the proton and neutron self-energies arising from intermediate nucleonic states only, see diagram (a) of Fig. 21, with those derived from Ref. [14] where the Argonne V_{18} nucleon–nucleon interaction [38] is used with relativistic boost corrections and a fitted three-body interaction, model. Here we employ the parametrization of Eq. (49) with $\delta = 0.2$. In the discussions below we will thus present two sets of results for β -stable matter, one where the nucleonic contributions to the self-energy of nucleons is derived from the baryon–baryon potential model of Stoks and Rijken [19] and one where the nucleonic contributions are replaced with the results from Ref. [14] following the parametrization discussed in Eq. (49). In the discussion in this subsection we will label these results with APR98. Hyperonic contributions will however all be calculated with the baryon–baryon interaction of Stoks and Rijken [19].

These models for the pure nucleonic part combined with the hyperon contribution yield the composition of β -stable matter, up to total baryonic number density $n = 1.2 \text{ fm}^{-3}$, shown in Fig. 22. The corresponding energies per baryon are shown in Fig. 23 for both pure nucleonic (BHF and APR98 pn-matter) and hyperonic matter (BHF and APR98 with hyperons) in β -equilibrium for the same baryonic densities as in Fig. 22.

For both types of calculations Σ^- appears at densities $\sim 2\text{--}3n_0$. Since the EoS of APR98 for nucleonic matter yields a stiffer EoS than the corresponding BHF calculation, Σ^- appears at $n = 0.27 \text{ fm}^{-3}$ for the APR98 EoS and $n = 0.35 \text{ fm}^{-3}$ for the BHF EoS. These results are in fair agreement with results obtained from mean field calculations, see e.g., Refs. [6,17,18,28,30,87,88]. The introduction of hyperons leads to a considerable softening of the EoS. Moreover, as soon as hyperons appear, the leptons tend to disappear, totally in the APR98 case whereas in the BHF calculation only muons disappear. This result is related to the fact that Λ does not appear at the densities considered here for the BHF EoS. For the APR98 EoS, Λ appears at a density $n = 0.67 \text{ fm}^{-3}$. Recalling $\mu_\Lambda = \mu_n = \mu_p + \mu_e$ and that the APR98 EoS is stiffer due to the inclusion of three-body forces, this clearly enhances the possibility of creating a Λ with the APR98 EoS. However, the fact that Λ does not appear in the BHF calculation can also, in addition to the softer EoS, be retraced to a delicate balance between the nucleonic and hyperonic hole state contributions (and thereby to features of the baryon–baryon interaction) to the self-energy of the baryons considered here, see diagrams (a) and (b) in Fig. 21. Stated differently, the contributions from Σ^- , proton and neutron hole states to the Λ chemical potential are not attractive enough to lower the chemical potential of the Λ so that it equals that of the neutron. Furthermore, the chemical potential of the neutron does not increase enough since contributions from Σ^- hole states to the neutron self-energy are attractive. We illustrate the role played by the two different choices for nucleonic EoS in Fig. 24 in terms of the chemical potentials for various baryons for matter in β -equilibrium. We also note that, using the criteria in Eq. (10), neither the Σ^0 nor Σ^+ do appear for both the BHF and the APR98 equations of state. This is due to the fact that none of the Σ^0 -baryon and Σ^+ -baryon interactions are attractive enough. A similar argument applies to Ξ^0 and Ξ^- . In the latter case the mass of the particle is $\sim 1315 \text{ MeV}$ and almost 200 MeV in attraction is needed in

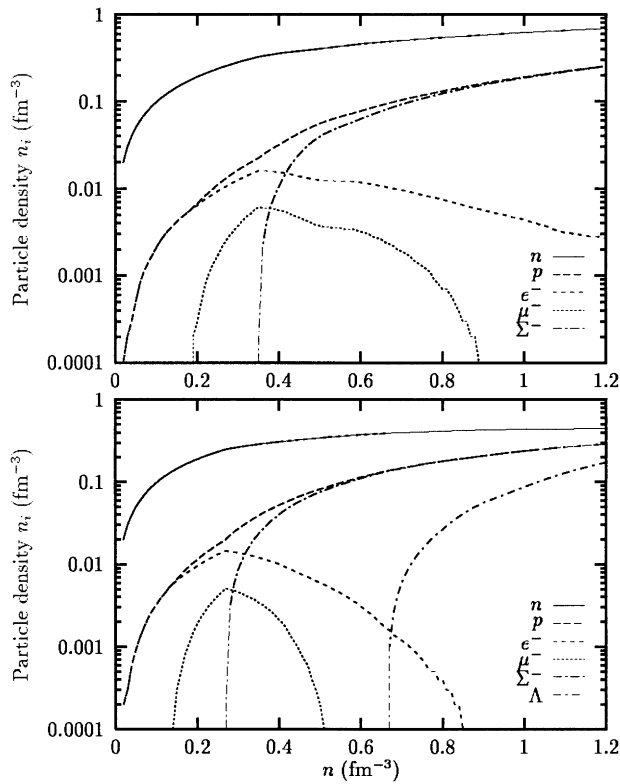


Fig. 22. Particle densities in β -stable neutron star matter as functions of the total baryonic density n . The upper panel represents the results obtained at the Brueckner–Hartree–Fock level with the potential of Stoks and Rijken [19]. In the lower panel the nucleonic part of the self-energy of the nucleons has been replaced with the EoS of Eq. (49) with $\delta = 0.2$.

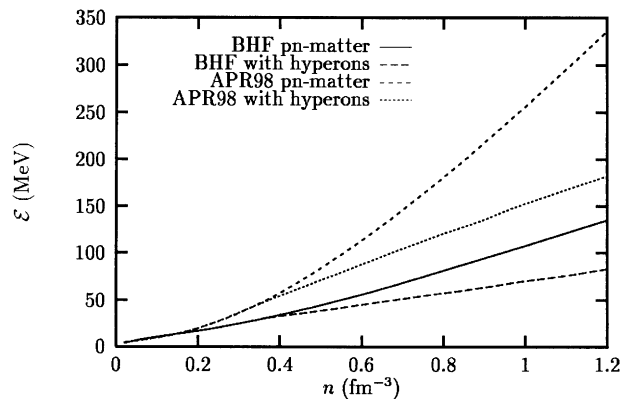


Fig. 23. Energy per baryon in β -stable neutron star matter for different approaches as function of the total baryonic density n . See text for further details.

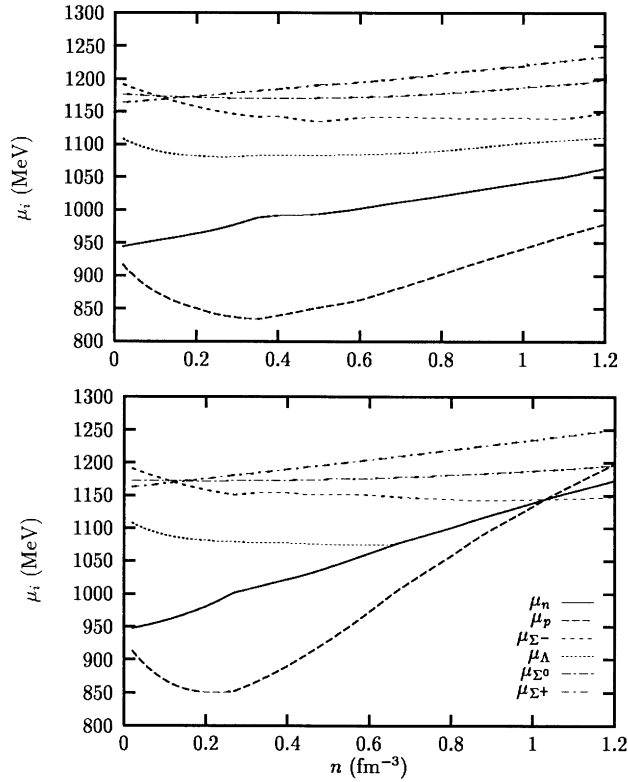


Fig. 24. Chemical potentials in β -stable neutron star matter as functions of the total baryonic density n . The upper panel represents the results obtained at the Brueckner-Hartree-Fock level with the potential of Stoks and Rijken [19]. The lower panel includes results obtained with the EoS of Eq. (49) with $\delta = 0.2$.

order to fulfill e.g., the condition $\mu_\Lambda = \mu_{\Sigma^0} = \mu_n$. From the bottom panel of Fig. 24 we see however that Σ^0 could appear at densities close to 1.2 fm^{-3} .

In summary, using the parametrized EoS of Akmal et al. [14] from Eq. (49) for the nucleonic sector and including hyperons through the most recent model for the baryon-baryon interaction of the Nijmegen group [19], we find through a many-body calculation for matter in β -equilibrium that Σ^- appears at a density of $n = 0.27 \text{ fm}^{-3}$ while Λ appears at $n = 0.67 \text{ fm}^{-3}$. Due to the formation of hyperons, the matter is deleptonized at a density of $n = 0.85 \text{ fm}^{-3}$. Within our many-body approach, no other hyperons appear at densities below $n = 1.2 \text{ fm}^{-3}$. Although the EoS of Akmal et al. [14] may be viewed as the currently most realistic approach to the nucleonic EoS, our results have to be gauged with the uncertainty in the hyperon-hyperon and nucleon-hyperon interactions. Especially, if the hyperon-hyperon interactions tend to be more attractive, this may lead to the formation of hyperons such as the Λ , Σ^0 , Σ^+ , Ξ^- and Ξ^0 at lower densities. The hyperon-hyperon interaction and the stiffness of the nucleonic contribution play crucial roles in the formation of various hyperons. These results differ from present mean field

calculations [6,17,18,28,30,87,88], where all kinds of hyperons can appear at the densities considered here.

In Section 5.3 we will discuss the implications on neutron star observables, however in our discussions on phase transitions in neutron stars, we will make life somewhat easier by just including quark degrees of freedom through a simplified model, namely the bag model, in order to account for degrees of freedom beyond the nucleonic ones. This is discussed in Section 2.8.

2.5. Kaon condensation

Kaon condensation in dense matter was suggested by Kaplan and Nelson [12], and has been discussed in many recent publications [91,92]. Due to the attraction between K^- and nucleons its energy decreases with increasing density, and eventually if it drops below the electron chemical potential in neutron star matter in β -equilibrium, a Bose condensate of K^- will appear. It is found that K^- 's condense at densities above $\sim 3\text{--}4\rho_0$, where $\rho_0 = 0.16\text{ fm}^{-3}$ is normal nuclear matter density. This is to be compared to the central density of $\sim 4\rho_0$ for a neutron star of mass $1.4M_\odot$ according to the estimates of Wiringa et al. [90] using realistic models of nuclear forces.

In neutron matter at low densities, when the interparticle spacing is much larger than the range of the interaction, $r_0 \gg R$, the kaon interacts strongly many times with the same nucleon before it encounters and interacts with another nucleon. Thus one can use the scattering length as the “effective” kaon–neutron interaction, $a_{K^-N} \simeq -0.41\text{ fm}$, where we ignore the minor proton fraction in nuclear matter. The kaon energy deviates from its rest mass by the Lenz potential

$$\omega_{\text{Lenz}} = m_K + \frac{2\pi}{m_R} a_{K^-N} n_{\text{NM}} , \quad (61)$$

which is the optical potential obtained in the impulse approximation. If hadron masses furthermore decrease with density the condensation will occur at lower densities [91].

At high densities when the interparticle spacing is much less than the range of the interaction, $r_0 \ll R$, the kaon will interact with many nucleons on a distance scale much less the range of the interaction. The kaon thus experiences the field from many nucleons and the kaon energy deviates from its rest mass by the Hartree potential:

$$\omega_{\text{Hartree}} = m_K + n_{\text{NM}} \int V_{K^-N}(r) d^3r , \quad (62)$$

As shown in Ref. [93], the Hartree potential is considerably less attractive than the Lenz potential. Already at rather low densities, when the interparticle distance is comparable to the range of the KN interaction, the kaon–nucleon and nucleon–nucleon correlations conspire to reduce the K^-N attraction significantly [94]. This is also evident from Fig. 25 where the transition from the low density Lenz potential to the high-density Hartree potential is calculated by solving the Klein–Gordon equation for kaons in neutron matter in the Wigner–Seitz cell approximation. Results are for square well K^-N -potentials of various ranges R .

Kaon–nucleon correlations reduce the K^-N interaction significantly when its range is comparable to or larger than the nucleon–nucleon interparticle spacing. The transition from the Lenz

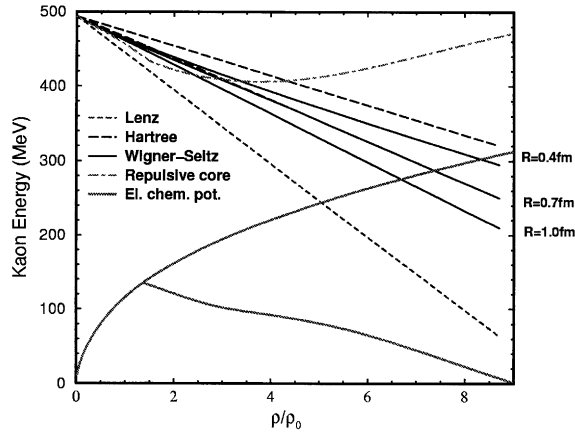


Fig. 25. Kaon energy as function of neutron density. Including nuclear correlations in the Wigner–Seltz cell approximation is shown by full curves for various ranges of the K^-n potentials $R = 0.4\text{fm}$, $R = 0.7\text{fm}$ and $R = 1.0\text{fm}$. At low densities they approach the Lenz result (Eq. (61), dotted curve) and at high densities they approach the Hartree result (Eq. (62), dashed curves). The electron chemical potential μ_e of our EoS Eq. (49) with $\delta = 0.2$ is shown with and without (lower and upper dotted curve) a transition to a mixed phase of quark matter for a Bag constant of $B = 100\text{ MeV fm}^{-3}$.

potential at low densities to the Hartree potential at high densities occurs already well below nuclear matter densities. For the measured K^-n scattering lengths and reasonable ranges of interactions the attraction is reduced by about a factor of 2–3 in cores of neutron stars. Relativistic effects further reduce the attraction at high densities. Consequently, a kaon condensate is less likely in neutron stars due to nuclear correlations. However, if kaon masses drop with densities [91] condensation will set in at lower densities.

If the kaon condensate occurs a mixed phase of kaon condensates and ordinary nuclear matter may coexist in a mixed phase [95] depending on surface and Coulomb energies involved. The structures would be much like the quark and nuclear matter mixed phases described above.

2.6. Pion condensation

Pion condensation is like kaon condensation possible in dense neutron star matter. For an in depth survey see e.g. Refs. [36,96] and references therein. If we first neglect the effect of strong correlations of pions with the matter in modifying the pion self-energy, one finds it is favorable for a neutron on the top of the Fermi sea to turn into a proton and a π^- when

$$\mu_n - \mu_p = \mu_e > m_\pi, \quad (63)$$

where $m_\pi = 139.6\text{ MeV}$ is the π^- rest mass. As discussed in the previous subsection, at nuclear matter saturation density the electron chemical potential is $\sim 100\text{ MeV}$ and one might therefore expect the appearance of π^- at a slightly higher density. One can however not neglect the interaction of the pion with the background matter. Such interactions can enhance the pion

self-energy and thereby the pion threshold density, and depending on the chosen parameters, see again Ref. [36], the critical density for pion condensation may vary from n_0 to $4n_0$. These matters are however not yet settled in a satisfying way, and models with strong nucleon–nucleon correlations tend to suppress both the πNN and $\pi\Delta N$ interaction vertices so that a pion condensation in neutron star matter does not occur. However, in addition to a charged pion condensate, one may also form a π^0 condensate through the reaction $n \rightarrow n + \pi^0$, if the π^0 effective mass in the medium is zero. The recent analysis, based on the V_{18} interaction model [38] of Akmal et al. [13,14,68] suggests such a pion condensate. The effects were partly discussed in Section 2.2 and the impact on the proton fraction was shown in Fig. 16. The π^0 condensation of Akmal et al. [14] for pure neutron matter appears at a density of $\sim 0.2 \text{ fm}^{-3}$ when the three-body interaction is included, whereas without V_{ijk} it appears at much higher densities, i.e. $\sim 0.5 \text{ fm}^{-3}$. Although it is a robust mechanism in the variational calculation of Ref. [14], the conclusion relies on both the model of the NN and three-body interactions adopted in the calculations. As noted in Ref. [41] for pure neutron matter, the V_{18} interaction resulted in a slightly different energy per particle at densities greater than 0.4 fm^{-3} when compared with the CD–Bonn and Nijmegen interactions. This topic was also discussed in Section 2.2 and shown in Fig. 3. Thus, before a firm conclusion can be reached about π^0 condensation, it is our belief that it should also be obtained at the two-body level with the other phase-shift equivalent NN interactions. That would lend strong support to the conclusions reached in Ref. [14]. The inclusion of three-body interactions introduces a further model dependence.

Due to these uncertainties, we will refrain in this work from presenting a thorough discussion of pion condensation. Rather, we will take the liberty to refer to, e.g. Refs. [14,29,36,96].

2.7. Superfluidity in baryonic matter

The presence of neutron superfluidity in the crust and the inner part of neutron stars are considered well established in the physics of these compact stellar objects. In the low-density outer part of a neutron star, the neutron superfluidity is expected mainly in the attractive 1S_0 channel. At higher density, the nuclei in the crust dissolve, and one expects a region consisting of a quantum liquid of neutrons and protons in beta equilibrium. The proton contaminant should be superfluid in the 1S_0 channel, while neutron superfluidity is expected to occur mainly in the coupled 3P_2 – 3F_2 two-neutron channel. In the core of the star any superfluid phase should finally disappear.

The presence of two different superfluid regimes is suggested by the known trend of the nucleon–nucleon (NN) phase shifts in each scattering channel. In both the 1S_0 and 3P_2 – 3F_2 channels the phase shifts indicate that the NN interaction is attractive. In particular for the 1S_0 channel, the occurrence of the well known virtual state in the neutron–neutron channel strongly suggests the possibility of a pairing condensate at low density, while for the 3P_2 – 3F_2 channel the interaction becomes strongly attractive only at higher energy, which therefore suggests a possible pairing condensate in this channel at higher densities. In recent years the BCS gap equation has actually been solved with realistic interactions, and the results confirm these expectations.

The 1S_0 neutron superfluid is relevant for phenomena that can occur in the inner crust of neutron stars, like the formation of glitches, which may to be related to vortex pinning of the superfluid phase in the solid crust [97]. The results of different groups are in close agreement on the 1S_0 pairing gap values and on its density dependence, which shows a peak value of about 3 MeV at a Fermi momentum close to $k_F \approx 0.8 \text{ fm}^{-1}$ [98–101]. All these calculations adopt the bare NN

Table 1

Collection of 3P_2 – 3F_2 energy gaps (in MeV) for the various potentials discussed in Section 2.2. BHF single-particle energies have been used. In case of no results, a vanishing gap was found

k_F (fm $^{-1}$)	CD-Bonn	V_{18}	Nijm I	Nijm II
1.2	0.04	0.04	0.04	0.04
1.4	0.10	0.10	0.10	0.10
1.6	0.18	0.17	0.18	0.18
1.8	0.25	0.23	0.26	0.26
2.0	0.29	0.22	0.34	0.36
2.2	0.29	0.16	0.40	0.47
2.4	0.27	0.07	0.46	0.67
2.6	0.21		0.47	0.99
2.8	0.17		0.49	1.74
3.0	0.11		0.43	3.14

interaction as the pairing force, and it has been pointed out that the screening by the medium of the interaction could strongly reduce the pairing strength in this channel [101–103]. However, the issue of the many-body calculation of the pairing effective interaction is a complex one and still far from a satisfactory solution.

The precise knowledge of the 3P_2 – 3F_2 pairing gap is of paramount relevance for, e.g. the cooling of neutron stars, and different values correspond to drastically different scenarios for the cooling process [29]. Generally, the gap suppresses the cooling by a factor $\sim \exp(-\Delta/T)$, see e.g. Ref. [47], which is severe for temperatures well below the gap energy. Unfortunately, only few and partly contradictory calculations of the pairing gap exist in the literature, even at the level of the bare NN interaction [104–108]. However, when comparing the results, one should note that the NN interactions used in these calculations are not phase-shift equivalent, i.e. they do not predict exactly the same NN phase shifts. Furthermore, for the interactions used in Refs. [104–107] the predicted phase shifts do not agree accurately with modern phase shift analyses, and the fit of the NN data has typically $\chi^2/\text{datum} \approx 3$. As we discussed in Section 2.2, progress has been made not only in the accuracy and the consistency of the phase-shift analysis, but also in the fit of realistic NN interactions to these data. As a result, several new NN interactions have been constructed which fit the world data for pp and np scattering below 350 MeV with high precision. Potentials like the recent Argonne V_{18} [38], the CD-Bonn [39] or the new Nijmegen potentials [37] yield a χ^2/datum of about 1 and may be called phase-shift equivalent. In Table 1 we show the recent non-relativistic pairing gaps for the 3P_2 – 3F_2 partial waves, where effective nucleon masses from the lowest-order Brueckner–Hartree–Fock calculation of Section 2.2 have been employed, see Ref. [109] for more details. These results are for pure neutron matter and we observe that up to $k_F \sim 2 \text{ fm}^{-1}$, the various potentials give more or less the same pairing gap. Above this Fermi momentum, which corresponds to a lab energy of $\sim 350 \text{ MeV}$, the results start to differ. This is simply due to the fact that the potentials are basically fit to reproduce scattering data up to this lab energy. Beyond this energy, the potentials predict rather different phase shifts for the 3P_2 – 3F_2 partial waves, see e.g. Ref. [109]. Thus, before a precise calculation of 3P_2 – 3F_2 energy gaps can be

made, one needs NN interactions that fit the scattering data up to lab energies of ~ 1 GeV. This means in turn that the interaction models have to account for the opening of inelasticities above 350 MeV due to the $N\Delta$ channel.

The reader should however note that the above results are for pure neutron matter. We end therefore this subsection with a discussion of the pairing gap for β -stable matter of relevance for the neutron star cooling discussed in Section 5. We will also omit a discussion on neutron pairing gaps in the 1S_0 channel, since these appear at densities corresponding to the crust of the neutron star. The gap in the crustal material is unlikely to have any significant effect on cooling processes [27], though it is expected to be important in the explanation of glitch phenomena. Therefore, the relevant pairing gaps for neutron star cooling should stem from the the proton contaminant in the 1S_0 channel, and superfluid neutrons yielding energy gaps in the coupled 3P_2 – 3F_2 two-neutron channel. If in addition one studies closely the phase shifts for various higher partial waves of the NN interaction, one notices that at the densities which will correspond to the core of the star, any superfluid phase should eventually disappear. This is due to the fact that an attractive NN interaction is needed in order to obtain a positive energy gap.

Since the relevant total baryonic densities for these types of pairing will be higher than the saturation density of nuclear matter, we will account for relativistic effects as well in the calculation of the pairing gaps. To do so, we resort to the Dirac–Brueckner–Hartree–Fock (DBHF) formalism discussed in Section 2.2.3.

As an example, consider the evaluation of the proton 1S_0 pairing gap using the DBHF approach. To evaluate the pairing gap we follow the scheme of Baldo et al. [98]. These authors introduced an effective interaction $\tilde{V}_{k,k'}$. This effective interaction sums up all two-particle excitations above a cutoff momentum k_M , $k_M = 3 \text{ fm}^{-1}$ in this work. It is defined according to

$$\tilde{V}_{k,k'} = V_{k,k'} - \sum_{k'' > k_M} V_{k,k''} \frac{1}{2\mathcal{E}_{k''}} \tilde{V}_{k'',k'} , \quad (64)$$

where the energy \mathcal{E}_k is given by $\mathcal{E}_k = \sqrt{(\tilde{\epsilon}_k - \tilde{\epsilon}_F)^2 + \Delta_k^2}$, $\tilde{\epsilon}_F$ being the single-particle energy at the Fermi surface, $V_{k,k'}$ is the free nucleon–nucleon potential in momentum space, defined by the three-momenta k, k' . The renormalized potential $\tilde{V}_{k,k'}$ and the free NN interaction $V_{k,k'}$ carry a factor $\tilde{m}^2/\tilde{E}_k\tilde{E}_{k'}$, due to the normalization chosen for the Dirac spinors in nuclear matter. These constants are also included in the evaluation of the G -matrix, as discussed in [43,74]. For the 1S_0 channel, the pairing gap Δ_k is [98,110,111]

$$\Delta_k = - \sum_{k' \leq k_M} \tilde{V}_{k,k'} \frac{\Delta_{k'}}{2\mathcal{E}_{k'}} . \quad (65)$$

These equations are solved self-consistently in order to obtain the pairing gap Δ for protons and neutrons for different partial waves.

In Fig. 26 we plot as function of the total baryonic density the pairing gap for protons in the 1S_0 state, together with the results from the non-relativistic approach discussed in Refs. [107,113]. The results in the latter references were also obtained with the Bonn A potential of Ref. [40]. These results are all for matter in β -equilibrium. In Fig. 27 we plot the corresponding relativistic results

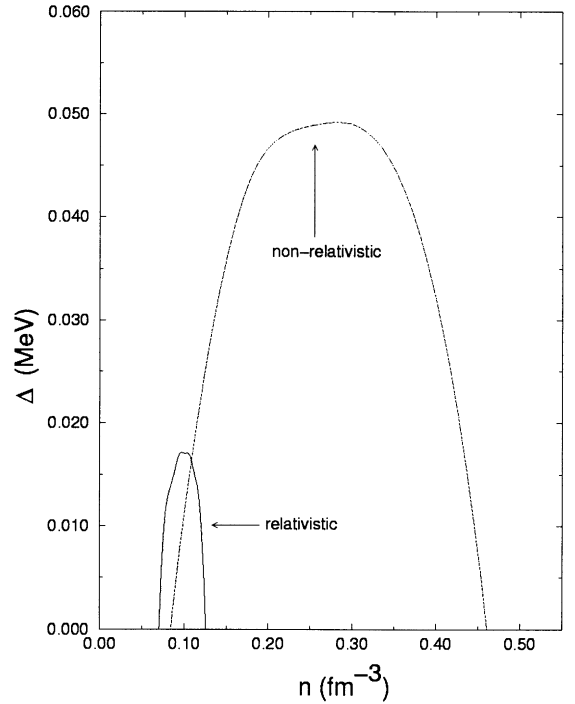
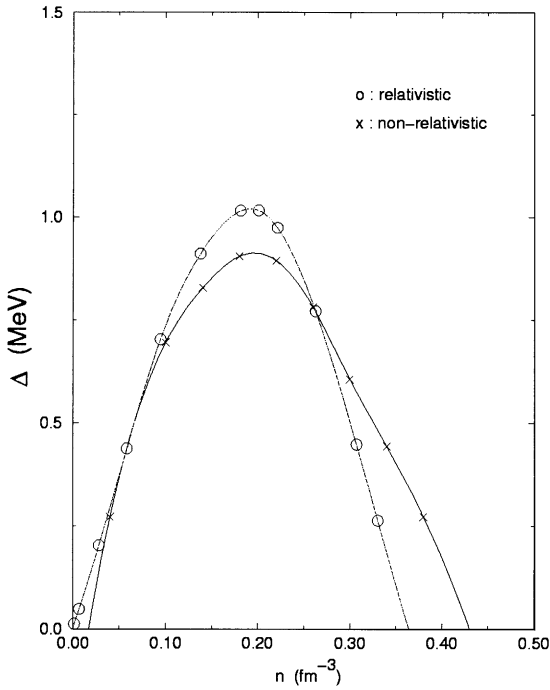


Fig. 26. Proton pairing in β -stable matter for the 1S_0 partial wave. The non-relativistic results are taken from Ref. [112].

Fig. 27. Neutron pairing in β -stable matter for the 3P_2 partial wave. The non-relativistic results are taken from Ref. [112].

for the neutron energy gap in the 3P_2 channel. For the 1D_2 channel we found both the non-relativistic and the relativistic energy gaps to vanish. The non-relativistic results for the Bonn A potential are taken from Ref. [112].

As can be seen from Fig. 26, there are only small differences (except for higher densities) between the non-relativistic and relativistic proton gaps in the 1S_0 wave.⁶ This is expected since the proton fractions (and their respective Fermi momenta) are rather small, see Fig. 6.

For neutrons however, the Fermi momenta are larger, and we would expect relativistic effects to be important. At Fermi momenta which correspond to the saturation point of nuclear matter, $k_F = 1.36 \text{ fm}^{-1}$, the lowest relativistic correction to the kinetic energy per particle is of the order of 2 MeV. At densities higher than the saturation point, relativistic effects should be even more important, as can clearly be seen in the calculations of Ref. [74]. Since we are dealing with very small proton fractions, a Fermi momentum of $k_F = 1.36 \text{ fm}^{-1}$, would correspond to a total baryonic density $\sim 0.09 \text{ fm}^{-3}$. Thus, at larger densities relativistic effects for neutrons should be

⁶ Even smaller differences are obtained for neutrons in the 1S_0 channel.

important. This is also reflected in Fig. 27 for the pairing gap in the 3P_2 channel. The relativistic 3P_2 gap is less than half the corresponding non-relativistic one, and the density region is also much smaller. This is mainly due to the inclusion of relativistic single-particle energies in the energy denominator of Eq. (65) and the normalization factors for the Dirac spinors in the NN interaction. As an example, at a neutron Fermi momentum $k_F = 1.5 \text{ fm}^{-1}$, the gap has a value of 0.17 MeV when one uses free single-particle energies and a bare NN potential. Including the normalization factors in the NN interaction, but employing free single-particle energies reduces the gap to 0.08 MeV. If we employ only DBHF single-particle energies and the bare NN interaction, the gap drops from 0.17 MeV to 0.04 MeV. Thus, the largest effect stems from the change in the single-particle energies, although, the combined action of both mechanisms reduce the gap from 0.17 MeV to 0.015 at $k_F = 1.5 \text{ fm}^{-1}$. The NN interaction in the 3P_2 channel depends also strongly on the spin–orbit force, see e.g. Fig. 3.3 in Ref. [40], and relativistic effects tend to make the NN spin–orbit interaction from the ω -meson in P -waves more repulsive [40]. This leads to a less attractive NN interaction in the 3P_2 channel and a smaller pairing gap.

The present results can be summarized as follows:

- The 1S_0 proton gap in β -stable matter is ≤ 1 MeV, and if polarization effects were taken into account [101], it could be further reduced by a factor 2–3.
- The 3P_2 gap is also small, of the order of ~ 0.1 MeV in β -stable matter. If relativistic effects are taken into account, it is almost vanishing. However, there is quite some uncertainty with the value for this pairing gap for densities above $\sim 0.3 \text{ fm}^{-3}$ due to the fact that the NN interactions are not fitted for the corresponding lab energies.
- Higher partial waves give essentially vanishing pairing gaps in β -stable matter.
- We have omitted a discussion of hyperon pairing, due to the uncertainties in the determination of the hyperon–hyperon interaction. We refer the reader here to Ref. [114] for a discussion of these gaps.

Consequences for cooling histories will be discussed in Section 5.

2.8. Quark matter

When nuclear matter is compressed to densities so high that the nucleon cores substantially overlap, one expects the nucleons to merge and undergo a phase transition to chiral symmetric and/or deconfined quark matter. Rephrased in terms of the relevant field excitations, we expect a transition from hadronic to quark degrees of freedom at high densities. Knowledge of the EOS of both hadronic and quark matter is necessary to estimate the possible effects of this transition in neutron stars.

Recent advances in the QCD phase diagram include improved lattice QCD calculations, random matrix models [115], and models addressing the possibility of color superconductivity at finite density [116]. Lattice QCD can only treat the case of zero baryon chemical potential and is therefore not useful for neutron stars. Lattice calculations suggest that QCD has a first order transition at finite temperature and zero chemical potential, provided that the strange quark is sufficiently light [117]. The transition weakens and might change to second order for large strange quark masses in the limit of QCD with two massless flavors.

Recent work using chiral random matrix models (chRMM) [115] suggests an effective thermodynamic potential of the form

$$\Omega(\phi; \mu, T)/N_f = \Omega_0(\mu, T) + \phi^2 - \frac{1}{2} \ln\{[\phi^2 - (\mu + iT)^2] \cdot [\phi^2 - (\mu - iT)^2]\} . \quad (66)$$

Here $\Omega_0(\mu, T)$ is unspecified and independent of the chiral mean field ϕ . The scale of dimensional quantities cannot be determined within the chRMM, and must be estimated by relating the variance of the Gaussian random matrix ensemble to the vacuum expectation value of the ϕ field via the Casher–Banks relation [115]. The value of ϕ at the minima of $\Omega(\phi; \mu, T)$ is related to the quark condensate, $\langle \bar{\psi}\psi \rangle$, which is the order parameter for chiral symmetry breaking. Minimization of Eq. (66) leads to a fifth-order polynomial equation for ϕ which is identical in form to the results of Landau–Ginzberg theory using a ϕ^6 potential. One solution to this equation corresponds to the restored symmetry phase with $\phi = 0$. This model predicts a second-order transition for $\mu = 0$ at a temperature, T_c , which is generally agreed to be in the range 140–170 MeV. For $T = 0$, a first-order transition occurs at some μ_0 . Since the phases in which chiral symmetry is broken and restored must be separated in the (μ, T) plane by an unbroken line of phase transitions, this implies the existence of a tricritical point in the theory of massless quarks.

There has recently been speculation regarding color superconductivity at medium densities resulting from non-perturbative attraction between quarks. At finite chemical potential, this invariably leads to the possibility of a diquark condensate which breaks global color invariance [116]. The associated color gap is ~ 100 MeV and may become the thermodynamically favorable phase at high baryon densities. When the strange quark is taken into account many different phases may exist [118] and such effects require more analysis.

2.8.1. Bag models

Since we do not have a fully reliable theory for the quark matter phase, we will for simplicity employ the simple Bag model in our actual studies of the mixed phase and neutron star properties. In the bag model the quarks in the hadrons are assumed to be confined to a finite region of space, the so-called “bag”, by a vacuum pressure B . The pressure from the quarks inside the bag is provided by the Fermi pressure and interactions computed to order $\alpha_s = g^2/4\pi$ where g is the QCD coupling constant. The pressure for quarks of flavor f , with $f = u, d$ or s is [119]

$$P_f = \frac{1}{4\pi^2} \left[\mu_f k_f (\mu_f^2 - 2.5m_f^2) + 1.5m_f^4 \ln\left(\frac{\mu_f + k_f}{m_f}\right) \right] - \frac{\alpha_s}{\pi^3} \left[\frac{3}{2} \left(\mu_f k_f - m_f^2 \ln\left(\frac{\mu_f + k_f}{m_f}\right) \right)^2 - k_f^4 \right] . \quad (67)$$

The Fermi momentum is $k_f = (\mu_f^2 - m_f^2)^{1/2}$. The total pressure, including the bag constant B simulating confinement is

$$P = P_e + \sum_f P_f - B . \quad (68)$$

The electron pressure is

$$P_e = \mu_e^4/12\pi^2 . \quad (69)$$

A Fermi gas of quarks of flavor i has density $n_i = k_{Fi}^3/\pi^2$, due to the three color states. There is no one-gluon exchange interaction energy between quarks of different flavor, while that between quarks of flavour i is given by $(2\alpha/3\pi)E_i$ per quark i [120]. Here E_i is the average kinetic energy per quark, and α is the strong interaction coupling constant, assumed to have a value of 0.5. The u and d quarks are taken to be massless, and s quarks to have a mass of 150 MeV. Typical quark chemical potentials $\mu_q \gtrsim m_N/3$ are generally much larger. The value of the bag constant B is poorly known, and we present results using three representative values, $B = 100 \text{ MeV fm}^{-3}$ [121], $B = 150 \text{ MeV fm}^{-3}$ and $B = 200 \text{ MeV fm}^{-3}$ [122]. Another possible model which has been applied to neutron star studies, and which differs from the Bag-model is a massive quark model, the so-called Color-Dielectric model (CDM) [123–125]. The CDM is a confinement model which has been used with success to study properties of single nucleons, such as structure functions [126] and form factors [127], or to describe the interaction potential between two nucleons [128], or to investigate quark matter [125,129]. In particular, it is possible, using the same set of parameters, both to describe the single nucleon properties and to obtain meaningful results for the deconfinement phase transition [125]. The latter happens at a density of the order of 2-3 times n_0 when symmetric nuclear matter is considered, and at even smaller densities for matter in β -equilibrium, as discussed below in this work. Another important feature is that effective quark masses in the CDM are always larger than a value of the order of 100 MeV. Hence chiral symmetry is broken and the Goldstone bosons are relevant degrees of freedom. This is to be contrasted with models like the MIT bag, where quarks have masses of a few MeV. We therefore expect the CDM to be relevant for computing the cooling rate of neutron stars *via* the Urca mechanism, as suggested by Iwamoto [130].

We will however stick to the Bag-model in our discussion of properties of neutron stars.

3. Thermodynamics of multi-component phase transitions

Numerous phase transitions may occur in neutron stars, e.g. the nuclear liquid–gas transition in the inner crust and in the interior quark matter and/or condensates of kaons, pions, hyperons, etc. may be present. We shall in this section briefly describe this curious phenomenon, the thermodynamics of multi-component systems and the corresponding mixed phases. It will be employed for neutron stars in the subsequent section.

3.1. Maxwell construction for one-component systems

In the usual picture the transition between two phases occurs at a unique pressure, temperature and chemical potential. Consequently, the density is expected to jump discontinuously at the boundary between the two phases. This is not only true for systems of one component as in the everyday example of water freezing or evaporating. It is also the case for some two component systems as, e.g. electrically neutral nuclear matter in β -equilibrium. Electric neutrality requires that

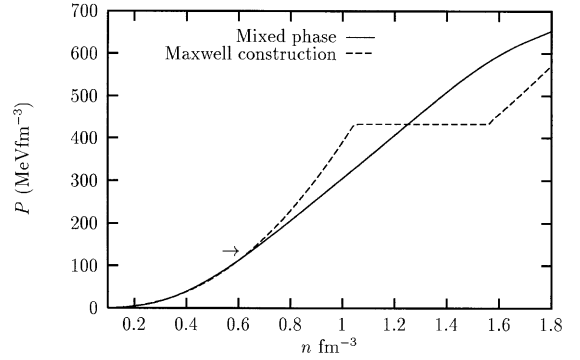
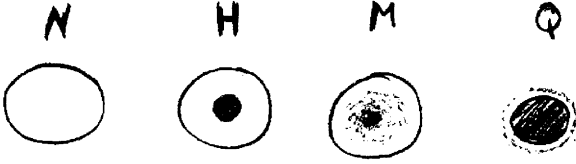


Fig. 28. Sketch of a neutron, hybrid, mixed and quark star.

Fig. 29. Pressure as function of density. Maxwell construction and mixed phase for bag parameter $B = 200 \text{ MeV fm}^{-3}$. The arrow indicates where the Maxwell construction starts.

the proton and electron densities are the same in bulk

$$n_p = n_e . \quad (70)$$

β -equilibrium requires that the chemical potentials of neutrons and protons only differ by that of the electrons

$$\mu_n = \mu_p + \mu_e^{\text{NM}} , \quad (71)$$

in nuclear matter. These two conditions restrict two of the three components leaving only one independent variable, the baryon density.

Likewise, in quark matter charge neutrality implies that

$$\frac{2}{3}n_u - \frac{1}{3}n_d - \frac{1}{3}n_s = n_e . \quad (72)$$

β -equilibrium requires analogously

$$\mu_d = \mu_s = \mu_u + \mu_e^{\text{QM}} . \quad (73)$$

Over the past two decades many authors have considered the properties of neutron stars with a core of quark matter [10]. In such “hybrid” stars (see Fig. 28) it is assumed that each of the two phases are electrically neutral separately as in Eqs. (70) and (72) and in β -equilibrium separately as in Eqs. (71) and (73). Gibb’s conditions $P_{\text{NM}} = P_{\text{QM}}$ and $\mu_n^{\text{NM}} = \mu_n^{\text{QM}}$ (the temperatures are vanishing in both phases) then determine a unique density at which the two bulk neutral phases coexist. This is the standard Maxwell construction and is seen in Fig. 29 as the double-tangent. In a gravitational field the denser phase (QM) will sink to the center whereas the lighter phase (NM) will float on top as a mantle as icebergs in the sea. At the interface of the phase transition there is a sharp density discontinuity and generally $\mu_e^{\text{NM}} \neq \mu_e^{\text{QM}}$ so that the electron densities $n_e = \mu_e^3/3\pi^2$ are

different in the two phases. This assumes that the sizes of QM structures are larger than electron screening lengths which, as discussed in [11], is *not* always the case.

For small values of the bag constants the phase transition occurs at densities lower than n_0 and the whole neutron star is a quark star except possibly for a hadronic crust [131].

Finally, to avoid confusion we emphasize that a mixed phase may have continuous pressures and (average) densities over large scales ~ 100 fm to kilometers and the phase transition is therefore second order in a thermodynamic sense. However, microscopically on length scales of order a few Fermi's a first-order phase transition between QM and NM is assumed and densities are discontinuous between the structures containing the QM and NM phases.

3.2. Two-component systems in a mixed phase

For several coexisting components as, e.g. dissolved chemicals, there may exist a mixed phase where the various chemical potentials of the solvents vary continuously – as does the pressure and densities. A similar phenomenon was predicted for the nuclear liquid–gas phase transitions in the inner crust of neutron stars confirmed by recent detailed numerical calculations [34,35]. In the inner crust the nuclei are surrounded by a neutron gas with an interpenetrating constant background of electrons, i.e. the nuclear matter and neutron gas form a mixed phase. Going a few hundred meters down in the neutron star crust the density of nuclei and thus also the average density increase continuously. Thus there is no sharp density discontinuity in bulk, i.e. over macroscopical distances of more than hundreds of Fermi's and up to several meters (see Fig. 28). However, on microscopical distances of a few Fermi's the density varies rapidly. Another example first considered by Glendenning [6] is that of a mixed phase of nuclear and quark matter.

Contrary to the Maxwell construction described in the previous subsection, where the condition of charge neutrality applies to both phases, Eqs. (70) and (72), it is relaxed to *overall* charge neutrality only. Thus two conditions are relaxed to one – allowing for one new variable quantity, which is usually taken as the *filling fraction* f of one of the phases in their coexisting mixture. For the nuclear and quark matter mixed phase the filling fraction is defined as the fraction of the volume which is in the quark phase

$$f \equiv V_{QM}/(V_{QM} + V_{NM}) , \quad (74)$$

and so $(1 - f)$ is the filling fraction of nuclear matter. The overall charge neutrality requirement is

$$fn_p + (1 - f)(\frac{2}{3}n_u - \frac{1}{3}n_d - \frac{1}{3}n_s) = n_e . \quad (75)$$

A number of requirements must be met in order to form such a mixed phase as addressed in [11]. These will be discussed in the following section for the mixed phase of nuclear and quark matter.

4. Structure of neutron stars

The structure of the neutron star is seriously affected by phase transitions, the order of the phase transition and whether mixed phases can occur over a significant part of the star. The important

questions to be addressed are numerous. When is it legitimate to regard the electron density as uniform, what is the spatial structure of the new phase, and is it energetically favorable? In order to answer these questions one must first investigate screening lengths of the various charged particles and compare to typical size scales of structures. For that matter Coulomb and surface energies must be calculated.

We will mainly discuss the mixed phase of nuclear and quark matter in cores of neutron stars. The mixed phase of nuclei and a neutron gas is in many ways similar and has been calculated in detail in Refs. [34,35,133].

4.1. Screening lengths

As described in [11] the mixed phase of quark and nuclear matter may be regarded as droplets of quark matter immersed in nuclear matter at lower densities, usually referred to as the *droplet phase*, even though at higher densities its structure is more complicated. If droplet sizes and separations are small compared with Debye screening lengths, the electron density will be uniform to a good approximation.

The Debye screening length, λ_D is given by

$$1/\lambda_D^2 = 4\pi \sum_i Q_i^2 \left(\frac{\partial n_i}{\partial \mu_i} \right)_{n_j, j \neq i}, \quad (76)$$

where n_i , μ_i , and Q_i are the number density, chemical potential, and charge of particle species i . Considering only electrons gives a screening length

$$\lambda_D^{(e)} = \frac{\sqrt{\pi/4\alpha}}{k_{F,e}}, \quad (77)$$

where $\alpha \simeq 1/137$ and the Fermi momentum $k_{F,e} = \mu_e$ since the electrons are always relativistic at these densities. For $\mu_e \lesssim 150$ MeV we thus obtain $\lambda_D^{(e)} \gtrsim 13$ fm. The screening length for protons alone $\lambda_D^{(p)}$, is given by $(\pi v_{F,p}/c 4\alpha(1 + F_0))^{1/2}/k_{F,p}$, where F_0 is the Landau parameter which gives the energy for proton density variations. At the saturation density for symmetric nuclear matter, $F_0 \simeq 0$, whereas at higher densities $F_0 \sim 1$ [132]. Since $\mu_p \sim m$, the nucleon mass, we find $\lambda_D^{(p)} \gtrsim 10$ fm, somewhat shorter than the electron screening length, and therefore in the nuclear matter phase, protons are the particles most effective at screening. The screening length for quarks is $\lambda_D^{(q)} \simeq 7/k_{F,q}$ where $q = u, d$, and s refer to up, down and strange quarks. It depends only slightly on whether or not s -quarks are present, so for $\mu_q \simeq m/3$ we find $\lambda_D^{(q)} \simeq 5$ fm.

In a composite system, such as the one we consider, screening cannot be described using a single screening length, but it is clear from our estimates, that if the characteristic spatial scales of structures are less than about 10 fm for the nuclear phase, and less than about 5 fm for the quark phase, screening effects will be unimportant, and the electron density will be essentially uniform. In the opposite case, when screening lengths are short compared with spatial scales, the total charge densities in bulk nuclear matter and quark matter will both vanish.

4.2. Surface and Coulomb energies of the mixed phase

When screening, lengths are much larger than the spatial scale of structures. This condition implies that the electron density is uniform everywhere, and all other particle densities are uniform within a given phase. The problem is essentially identical to that of matter at subnuclear densities [133], and the structure is determined by competition between Coulomb and interface energies. When quark matter occupies a small fraction, f , of the total volume, it will form spherical droplets immersed in nuclear matter. For higher filling fractions, the quark matter will adopt shapes more like rods (“spaghetti”) and plates (“lasagna”), rather than spheres. For $f \geq 0.5$, the structures expected are the same as for a filling factor $1 - f$, but with the roles of nuclear matter and quark matter reversed. Thus, one expects for increasing f that there will be regions with nuclear matter in rod-like structures, and roughly spherical droplets.

To estimate characteristic dimensions, some special cases can be considered. The intricate structures in the general case will be discussed in Section 4.5. When f is small or close to unity, the minority phase will form spherical droplets. The surface energy per droplet is given by

$$\mathcal{E}_S = \sigma 4\pi R^2, \quad (78)$$

where σ is the surface tension, and the Coulomb energy is

$$\mathcal{E}_C = \frac{3}{5} Z^2 e^2 / R = (16\pi^2/15)(\rho_{QM} - \rho_{NM})^2 R^5. \quad (79)$$

Here Z is the excess charge of the droplet compared with the surrounding medium, $Ze = (\rho_{QM} - \rho_{NM})V_D$ where $V_D = (4\pi/3)R^3$ is the droplet volume and ρ_{QM} and ρ_{NM} are the total charge densities in bulk quark and nuclear matter, respectively. Minimizing the energy density with respect to R one obtain the usual result that $\mathcal{E}_S = 2\mathcal{E}_C$ and find a droplet radius

$$R = \left(\frac{15}{8\pi(\rho_{QM} - \rho_{NM})^2} \sigma \right)^{1/3} \simeq 5.0 \text{ fm} \left(\frac{\sigma}{\sigma_0} \right)^{1/3} \left(\frac{\rho_{QM} - \rho_{NM}}{\rho_0} \right)^{-2/3}. \quad (80)$$

In the second formula we have introduced the quantities $\rho_0 = e \cdot 0.4 \text{ fm}^{-3}$ and $\sigma_0 = 50 \text{ MeV fm}^{-2}$ which, as we shall argue below, are typical scales for the quantities. (A droplet of symmetric nuclear matter in vacuum has a surface tension $\sigma = 1 \text{ MeV fm}^{-2}$ for which (80) gives $R \simeq 4 \text{ fm}$, which agrees with the fact that nuclei like ^{56}Fe are the most stable form of matter for roughly symmetric nuclear matter at low density.) The form of Eq. (80) reflects the fact that on dimensional grounds, the characteristic length scale is $(\sigma/(\rho_{QM} - \rho_{NM})^2)^{1/3}$ times a function of f .

The total Coulomb and surface energy per unit volume is given for small f by

$$\begin{aligned} \varepsilon_{S+C} &= f 9((\pi/15)\sigma^2(\rho_{QM} - \rho_{NM})^2)^{1/3} \\ &\simeq 44 \text{ MeV fm}^{-3} f \left(\frac{\sigma}{\sigma_0} \frac{\rho_{QM} - \rho_{NM}}{\rho_0} \right)^{2/3}. \end{aligned} \quad (81)$$

The result for f close to unity is given by replacing f by $1 - f$. In the case when the volumes of quark and nuclear matter are equal, $f = \frac{1}{2}$, the structure can be approximated as alternating layers, of quark and nuclear matter and was considered in [11].

To estimate length scales and energy densities, one needs the surface tension of quark matter and the charge densities in the two phases. A rough estimate of the surface tension is the bag constant, B , times a typical hadronic length scale ~ 1 fm. Estimates of the bag constant range from 50 to 450 MeV fm^{-3} [134]. The kinetic contribution to the surface tension at zero temperature has been calculated in the bag model in Ref. [135]. Only massive quarks contribute because relativistic particles, unlike non-relativistic ones, are not excluded near the surface due to the boundary conditions. The kinetic contribution to σ from a quark species depends strongly on its mass and chemical potential. For $m_s \ll \mu_s$ it behaves as $(3/4\pi^2)\mu_s^2 m_s$, and it vanishes as m_s approaches μ_s . If we adopt for the strange quark mass the value $m_s \simeq 150 \text{ MeV}$, and for the quark chemical potentials one-third of the baryon chemical potential, which generally is slightly larger than the nucleon mass, $\mu_s \simeq \mu_B/3 \gtrsim m/3$, one obtains from Ref. [135] $\sigma \simeq 10 \text{ MeV fm}^{-2}$, which is close to the maximum value it can attain for any choice of m_s . We conclude that the surface tension for quark matter is poorly known, but lies most probably in the range $10\text{--}100 \text{ MeV fm}^{-2}$. (Lattice gauge theory estimates of σ at high temperatures and zero quark chemical potentials lie in the range $\sigma \simeq 0.14 - 0.28 T_c^3 \sim 10\text{--}60 \text{ MeV fm}^{-2}$ [136] for $T_c \sim 150\text{--}200 \text{ MeV}$, comparable to our estimates for cold quark matter, but it is unclear to what extent this agreement is accidental.)

To estimate charge densities, we consider quark matter immersed in a uniform background of electrons. β -equilibrium insures that $\mu_d = \mu_s = \mu_u + \mu_e$, and therefore in the absence of quark–quark interactions, one finds the total electric charge density in the quark matter phase is given for $\mu_e \ll \mu_u \sim \mu_d \equiv \mu_q$ and $m_s \ll \mu_q$ by

$$\rho_{\text{QM}} = \frac{e}{3}(2n_u - n_d - n_s - 3n_e) \simeq \frac{e}{\pi^2}(\frac{1}{2}m_s^2\mu_q - 2\mu_e\mu_q^2) . \quad (82)$$

Assuming $m_s \simeq 150 \text{ MeV}$ and $\mu_q \simeq m/3$ the second term dominates except for small μ_e and so the droplet is negatively charged and for $\mu_e \simeq 170 \text{ MeV}$ the density is about $-0.4e \text{ fm}^{-3}$, the characteristic scale of densities adopted in making estimates above.

Due to the high quark density, ρ_{NM} is small compared with ρ_{QM} in Eq. (80) when quark matter occupies a small fraction of the volume. The electron chemical potential in neutron stars depends strongly on the model for the nuclear equation of state, but generally one finds $\mu_e \lesssim 170 \text{ MeV}$. Consequently, for $\sigma \simeq 10 \text{ MeV fm}^{-2}$ we find from Eq. (80) a radius of $R \gtrsim 3.1 \text{ fm}$, whereas $\sigma \simeq 100 \text{ MeV fm}^{-2}$ gives $R \gtrsim 6.6 \text{ fm}$. For f close to unity one finds nuclear bubble radii which are comparable with those for quark droplets, and for the layer-like structures expected for $f \simeq 0.5$, half the layer thickness is of comparable size. Estimates of characteristic scales for rod-like structures give similar values.

Detailed calculations show that the effects of nonuniformity of the charge distribution affect estimates of Coulomb energies significantly if the characteristic lengths, R and a , exceed the Debye screening length. The estimates of screening lengths made above show that screening will not be dominant for surface tensions below about 100 MeV , if the charge density difference is ρ_0 , but for higher values the simple picture of coexisting uniform bulk phases would become invalid, and the droplet phase would resemble increasingly two electrically neutral phases in equilibrium.

For the smallest droplets of size $R \sim 5 \text{ fm}$ the charge $Z = (4\pi/3)R^3\rho_{\text{QM}}$ and baryon number $A = (4\pi/3)R^3n_{\text{QM}}$ are typically a few hundreds.

4.3. Is the mixed phase energetically favored?

If the bulk energy gained by going to the mixed phase is larger than the costs of the associated Coulomb and surface energies, then the mixed phase is energetically favored. Before going on to estimate these crucial energies we point out the basic physical reason why the bulk energy is lower in the mixed phase. As mentioned in connection with Eq. (82) the QM droplets are *negatively* charged. By immersing QM in the positively charged NM we can either remove some of the electrons from the top of the Fermi levels with energy μ_e , or we can increase the proton fraction in NM by which the symmetry energy is lowered. In equilibrium a combination of both will occur and in both cases *bulk energy is saved* and a lower energy density is achieved as seen in Fig. 29.

To calculate the bulk energy we adopt a simple form for the energy density of nuclear matter consisting of a compressional term, a symmetry term, and an electron energy density as discussed in Eq. (49)

$$\varepsilon_{\text{NM}} = nE = n[m + E_{\text{comp}}(n) + S(n)x^2] + \varepsilon_e + \varepsilon_\mu, \quad (83)$$

where, e.g., $\varepsilon_e = \mu_e^4/4\pi^2$. For quark matter the bag model equation of state gives an energy density

$$\varepsilon_{\text{QM}} = \left(1 - \frac{2\alpha_s}{\pi}\right) \left(\sum_{q=u,d,s} \frac{3\mu_q^4}{4\pi^2}\right) + B + \varepsilon_e + \varepsilon_\mu \quad (84)$$

with the QCD fine structure constant $\alpha_s \simeq 0.4$ and bag constant $B \simeq 120 \text{ MeV fm}^{-3}$. We have taken all quark masses to be zero. In the absence of surface and Coulomb effects the equilibrium conditions for the droplet phase are that the quark and nuclear matter should have equal pressures, and that it should cost no energy to convert a neutron or a proton in nuclear matter into quarks in quark matter. The last condition amounts to $\mu_n = 2\mu_d + \mu_u$ and $\mu_p = \mu_d + 2\mu_u$. The electron density is the same in quark and nuclear matter, and we assume that matter is electrically neutral and in β -equilibrium, that is $\mu_n = \mu_p + \mu_e$ and $\mu_d = \mu_u + \mu_e$. The chemical potentials are related to the Fermi momenta by $\mu_q = p_{F,q}(1 - 2\alpha_s/\pi)^{-1/3}$. Electrons contribute little to pressures, but they play an important role through the β -equilibrium and charge neutrality conditions.

Fig. 30(a) shows the density dependence of the energy density of the droplet phase calculated neglecting surface and Coulomb energies ($\sigma = 0$) for a simple quadratic EoS for nuclear matter [11]. The energy of uniform, electrically neutral, bulk nuclear matter in β -equilibrium is also shown, together with the corresponding result for quark matter. The double-tangent construction gives the energy density for densities at which the two bulk neutral phases coexist. This corresponds to the standard treatment of the phase transition between nuclear matter and quark matter, in which the pressure remains constant throughout the transition, and consequently neutron stars have a core of quark matter and a mantle of nuclear matter, with a sharp density discontinuity at the phase transition. As one sees, if surface and Coulomb effects may be ignored, the transition from nuclear matter to the droplet phase occurs at a lower density than the transition to two bulk neutral phases, a feature also apparent in Ref. [6]. In addition, droplets of nuclear matter survive up to densities above those at which bulk neutral phases can coexist. We also observe that bulk contributions to the energy density of the droplet phase are always lower than those for coexisting bulk neutral phases. While detailed properties of the droplet phase depend strongly on the bulk

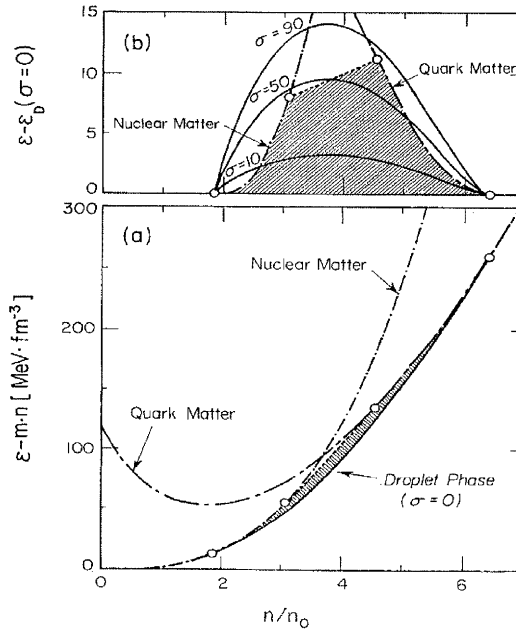


Fig. 30. (a) The full line gives the energy density of the droplet phase without surface and Coulomb energies ($\sigma = 0$). Also shown are the energy densities of electrically neutral bulk nuclear matter, quark matter in β -equilibrium, and the double tangent construction (dashed line) corresponding to the coexistence of bulk electrically neutral phases. (b) Energy densities of the droplet phase relative to its value for $\sigma = 0$ for $\sigma = 10, 50$, and 90 MeV fm^{-2} . When the energy density of the droplet phase falls within the hatched area it is energetically favored. From [11].

energies, the qualitative picture we find persists over a wide range of possible bulk matter properties.

When quark matter occupies a small fraction of space, f , one observes in Fig. 30 that the difference in energy between the droplet phase and bulk neutral nuclear matter varies as f^2 . This is a general result for mixed phases which follows directly from the 1st law of thermodynamics. Consider the energy in a fixed volume at zero temperature. The change in energy by converting some of the quarks into nucleons at fixed volume is

$$dE = \sum_i \mu_i dN_i = dN_{\text{NM}}(\mu_{\text{NM}} - \mu_{\text{QM}}). \quad (85)$$

In the latter equation we have used that at constant average density and fixed volume, the number of extra nucleons is exactly the baryon number removed from the quark phase (a third of the number of quarks removed), $dN_{\text{NM}} = -dN_{\text{QM}}$. This applies to both neutrons and protons. To obtain the energy difference between the mixed phase and NM at the same density, we need to convert all QM into nucleons. For small filling fraction f this number is small and we can apply Eq. (85). In fact both dN_N and the difference between chemical potentials, $\mu_{\text{NM}} - \mu_{\text{QM}}$ is small as they both vanish right at the onset of the mixed phase, $f \simeq 0$. Therefore, they must both grow

linearly with f and thus the difference between the mixed and NM phase at the same density must scale with f^2 according to Eq. (85). By inversion the same results apply for f close to unity.

In contrast to the quadratic dependence on f of the bulk energy difference, the contributions to the energy density from surface and Coulomb energies are linear in f , see Eq. (81). This shows that the transitions to the droplet phase must occur via a first-order transition after all. Pressures and densities are continuous in the mixed phase only when surface and Coulomb energies can be completely neglected. Even for a small surface tension they will change the second order to multiple (small) first-order phase transitions whenever the dimensionality of the structures change.

If the surface and Coulomb energies are sufficiently large, the droplet phase may never be favorable. The energy-density difference between the droplet phase, neglecting surface and Coulomb effects, and two coexisting neutral phases is at most 10 MeV fm^{-3} , as may be seen from Fig. 30. This is very small compared with characteristic energy densities which are of order 1000 MeV fm^{-3} . In Fig. 30(b) we show the energy density of the droplet phase for various values of the surface tension, relative to the value for $\sigma = 0$. In these calculations the geometry of the droplets was characterized by a continuous dimensionality, d , as described in Ref. [133], with $d = 3, 2$ and 1 corresponding to spheres, rods and plates, respectively. For the droplet phase to be favorable, its energy density must lie below those of nuclear matter, quark matter, and coexisting electrically neutral phases of nuclear and quark matter. That is the droplet phase will be favored if its energy lies within the hatched region in Fig. 30(a) and (b). We see that whether or not the droplet phase is energetically favorable depends crucially on properties of quark matter and nuclear matter. For our model the droplet phase is energetically favorable at some densities provided $\sigma \lesssim 70 \text{ MeV fm}^{-2}$. However, given the large uncertainties in estimates of bulk and surface properties one cannot at present claim that the droplet phase is definitely favored energetically.

4.4. Melting temperatures

Should the quark-droplet phase exist in neutron stars, it could have important observational consequences. First, the pressure difference across the droplet phase can be large, of order 250 MeV fm^{-3} as seen from Fig. 30(a), since the pressure is the negative intercept of the tangent to the curve. Consequently, a large portion of a neutron star could consist of matter in the droplet phase. Secondly, phases with isolated droplets would be expected to be solid. The melting temperature for a body centered cubic lattice is [137]

$$T_c \sim (Z^2 e^2 / 170R) f^{1/3}, \quad (86)$$

where $R/f^{1/3}$ is the lattice spacing. The melting temperature is typically some tens of MeV for the smallest lattices and decreasing with increasing lattice spacing ($f \rightarrow 0$). While spaghetti- and lasagna-like structures would exhibit anisotropic elastic properties, being rigid to some shear strains but not others in much the same way as liquid crystals. This could be important for quake phenomena, which have been invoked to explain observations in a number of different contexts. Third, neutrino generation, and hence cooling of neutron stars could be influenced. This could come about because nuclear matter in the droplet phase has a higher proton concentration than bulk, neutral nuclear matter, and this could make it easier to attain the threshold condition for the nucleon direct Urca process [138]. Another is that the presence of the spatial structure of the droplet phase might allow processes to occur which would be forbidden in a translationally

invariant system. Finally, one should bear in mind the possibility that even if the droplet phase were favored energetically, it would not be realized in practice if the time required to nucleate is too long.

4.5. Funny phases

Surface and Coulomb energies determine the topology and length scales of the structures. Denoting the dimensionality of the structures by d ($d = 3$ for droplets and bubbles, $d = 2$ for rods and $d = 1$ for plates) the surface and Coulomb energies are generally [27,34]

$$\mathcal{E}_S = d\sigma(4\pi/3)R^2 \quad (87)$$

$$\mathcal{E}_C = \frac{8\pi^2}{3(d+2)}(\rho_{QM} - \rho_{NM})^2 R^5 \left[\frac{2}{d-2} \left(1 - \frac{d}{2} f^{1-2/d} \right) + f \right], \quad (88)$$

where ρ_{QM} and ρ_{NM} are the total charge densities in bulk QM and NM, respectively. For droplets ($f \simeq 0$) or bubbles ($f \simeq 1$) $d = 3$ and the Coulomb energies reduce to the usual term $\mathcal{E}_C = (3/5)Z^2 e^2 / R$ where Z is the excess charge of the droplet compared with the surrounding medium, $Ze = (4\pi/3)(\rho_{QM} - \rho_{NM})R^3$. Minimizing the energy density with respect to R we obtain the usual result that $\mathcal{E}_S = 2\mathcal{E}_C$.⁷ Minimizing with respect to the continuous dimensionality as well thus determines both R and d .

For the Walecka model the droplet phase is energetically favorable at some densities provided $\sigma \lesssim 20 \text{ MeV/fm}^2$ [139]. For comparison, using a quadratic EoS for NM [11], one finds instead the more favorable condition $\sigma \lesssim 70 \text{ MeV/fm}^2$. Given the large uncertainties in estimates of bulk and surface properties one cannot at present claim that the droplet phase is definitely favored energetically.

The mixed phase in the inner crust of neutron stars consists of nuclear matter and a neutron gas in β -equilibrium with a background of electrons such that the matter is overall electrically neutral [34,35]. Likewise, quark and nuclear matter can have a mixed phase [6] and possible also nuclear matter with and without condensate of any negatively charged particles such as K^- [95], π^- , Σ^- , etc. The quarks are confined in droplet, rod- and plate-like structures [11] (see Fig. 31) analogous to the nuclear matter and neutron gas structures in the inner crust of neutron stars [34,35]. Depending on the equation of state, normal nuclear matter exists only at moderate densities, $\rho \sim 1 - 2\rho_0$. With increasing density, droplets of quark matter form in nuclear matter and may merge into rod- and later plate-like structures. At even higher densities the structures invert forming plates, rods and droplets of nuclear matter in quark matter. Finally, pure quark matter is formed at very high densities unless the star already has exceeded its maximum mass.

A necessary condition for forming these structures and the mixed phase is that the additional surface and Coulomb energies of these structures are sufficiently small. Excluding them makes the mixed phase energetically favored [6]. That is also the case when surface energies are small (see [11] for a quantitative condition). If they are too large the neutron star will have a core of pure quark matter with a mantle of nuclear matter surrounding and the two phases are coexisting by an ordinary first-order phase transition.

⁷ The condition for fission instability is contrarily: $2\mathcal{E}_S \leq \mathcal{E}_C$.

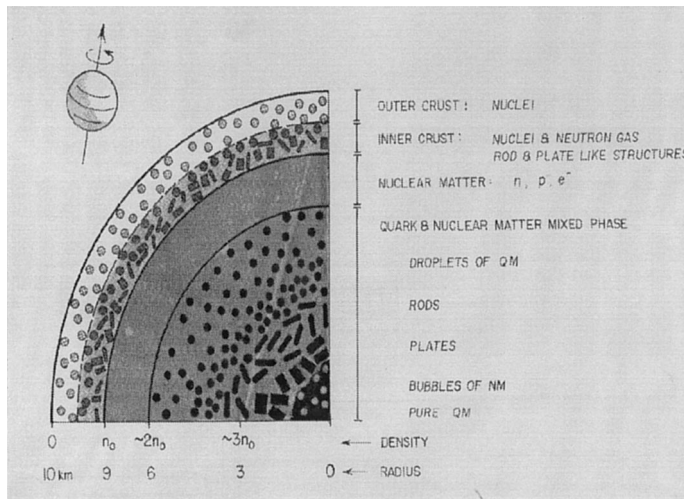


Fig. 31. Nuclear and quark matter structures in a $\sim 1.4M_{\odot}$ neutron star. Typical sizes of structures are $\sim 10^{-14}$ m but have been scaled up to be seen.

The quark and nuclear matter mixed phase has continuous pressures and densities [6] when surface and Coulomb energies are excluded. There are at most two second-order phase transitions. Namely, at a lower density, where quark matter first appears in nuclear matter, and at a very high density, where all nucleons are finally dissolved into quark matter, if the star is gravitationally stable at such high central densities. However, due to the finite Coulomb and surface energies associated with forming these structures, the transitions change from second to first order at each topological change in structure [11]. If the surface and Coulomb energies are very small the transitions will be only weakly first order but there may be several of them.

4.6. Summary of neutron star structures

To summarize, we have shown that whether or not a droplet phase consisting of quark matter and nuclear matter can exist in neutron stars depends not only on bulk properties, but also on the surface tension. In order to make better estimates, it is important to improve our understanding of the transition between bulk nuclear matter and bulk quark matter. For the droplet phase to be possible, this must be first-order. If the transition is indeed first-order, better estimates of the surface tension are needed to determine whether the droplet phase is favored energetically.

In these analyses several restrictions were made: the interfaces were sharp, the charge densities constant in both NM and QM and the background electron density was also assumed constant. Relaxing these restrictions generally allow the system to minimize its energy further. Constant charge densities may be a good approximation when screening lengths are much larger than spatial length scales of structures but since they are only slightly larger [11] the system may save significant energy by rearranging the charges.

5. Observational consequences for neutron stars

In this section we first briefly review the observational status of neutron star masses from binary pulsars and X-ray binaries. Subsequently, we revisit the equations for calculating the structure of rotating neutron stars and calculate masses, radii, moments of inertia, etc. for rotating neutron stars with the equations of state described in the previous sections with and without phase transitions. Glitches are then discussed in Sections 5.6 and 5.7 while a discussion on neutron star cooling is given in Section 5.8. In the last two subsections we discuss supernovae and gamma-ray-bursts.

5.1. Masses from radio pulsars, X-ray binaries and QPO's

The measurements of masses and radii of neutron stars (as well as detailed study of their cooling histories and rotational instabilities) may provide a unique window on the behavior of matter at densities well above that found in atomic nuclei. The most precisely measured physical parameter of any rotating neutron star, or pulsar, is its spin frequency. The frequencies of the fastest observed pulsars (PSRB1937 + 21 at 641.9 Hz and B1957 + 20 at 622.1 Hz) have already been used to set constraints on the nuclear equation of state at high densities under the assumption that these pulsars are near their maximum (breakup) spin frequency. However, the fastest observed spin frequencies may be limited by complex accretion physics rather than fundamental nuclear and gravitational physics. A quantity more directly useful for comparison with physical theories is the neutron star mass. In Fig. 32 we show the latest compilation of Thorsett and Chakrabarty [140] of

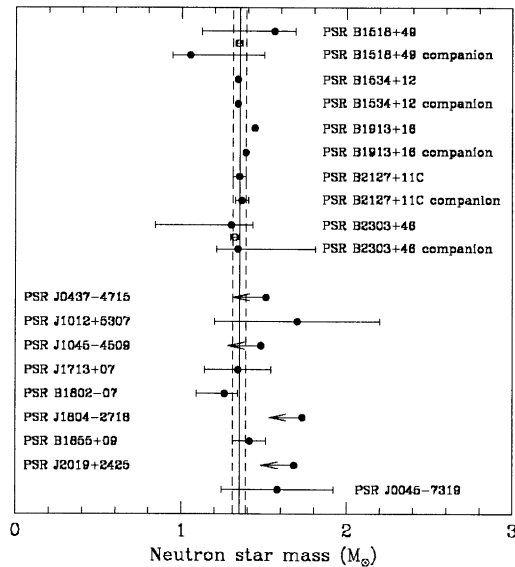


Fig. 32. Neutron star masses from observations of radio pulsar systems. Error bars indicate central 68% confidence limits, except upper limits are one-sided 95% confidence limits. The vertical lines are drawn at a mass $1.35 \pm 0.04 M_{\odot}$. Taken from Ref. [140].

neutron star masses in binary radio pulsar systems. As can be seen from this figure, most of observed binary pulsars exhibit masses around $1.4M_{\odot}$. One exception may be PSR J1012 + 5307 with mass $M = (2.1 \pm 0.8)M_{\odot}$ [141]. However, its mass is less well determined as the system is non-relativistic. The masses are determined from pulse delays of the millisecond pulsar as well as radial-velocity curves and spectral lines of the white dwarf companion.

The recent discovery of high-frequency brightness oscillations from 11 neutron stars in low-mass X-ray binaries may provide us with a new promising method for determining masses and radii of neutron stars. These quasi-periodic oscillations (QPO) are observed in both the persistent X-ray emission and in bursts. According to the most successful model of Miller et al. [142] the QPO's are most likely the orbital frequencies of accreting gas in Keplerian orbits around neutron stars. The orbital frequency of the gas at distance r from the neutron star is

$$v_{\text{QPO}} = (1/2\pi)(M/r)^{1/2} . \quad (89)$$

As the QPO last many periods, the gas has to be in a stable orbit. The innermost stable orbit R_{ms} for a slowly rotating neutron star is related to its mass as

$$M = (c^2/6G)R_{\text{ms}} . \quad (90)$$

Thus we obtain the limits on the non-rotating neutron star masses and radii:

$$M \leq 2.2M_{\odot} \text{ kHz}/v_{\text{QPO}} , \quad (91)$$

$$R \leq 20 \text{ km kHz}/v_{\text{QPO}} . \quad (92)$$

For example, the 1220 Hz QPO observed in the atoll source 4U 1636-536 limits the neutron star mass to $M \leq 1.8M_{\odot}$ and its radius to $R \leq 16 \text{ km}$. It was predicted by Miller et al. [142] that as the accretion flux increases towards the innermost stable orbit the QPO frequency should stop increasing. This was subsequently observed by Zhang et al. [4] and Kaaret et al. [143] for 4U 1820-30 which has $v_{\text{QPO}} = 0.8\text{--}0.9 \text{ kHz}$. The resulting neutron star mass is $M \simeq 2.3M_{\odot}$ when rotation is included. The deduced mass is consistent with the hypothesis that these neutron stars were born with $M \simeq 1.4M_{\odot}$ and have been accreting matter at a fraction of the Eddington limit for 10^8 yr . The QPO's provide an important tool for determining neutron star masses or at least restricting them and for limiting radii. Due to accretion they are expected to be heavier than X-ray binaries and therefore potentially more interesting for restricting maximum masses and the EoS.

In Fig. 33 we show the mass–radius relations for the various equations of state to be discussed in Section 5.3 (see also [144]). The shaded area represents the allowed masses and radii for $v_{\text{QPO}} = 1060 \text{ Hz}$ of 4U 1820-30. Generally,

$$2GM < R < \left(\frac{GM}{4\pi^2 v_{\text{QPO}}^2} \right)^{1/3} , \quad (93)$$

where the lower limit ensures that the star is not a black hole, and the upper limit that the accreting matter orbits outside the star, $R < R_{\text{orb}}$. Furthermore, for the matter to be outside the innermost stable orbit, $R > R_{\text{ms}} = 6GM$, sets an upper limit on the mass, Eq. (91). The mass–radius relations for the specific EoS's will be discussed in the following subsections.

A new determination of the mass of the accretion powered X-ray pulsar Vela X-1 [145] gives the mass (95% confidence limit)

$$M = 1.93_{-0.17}^{+0.23} M_{\odot} . \quad (94)$$

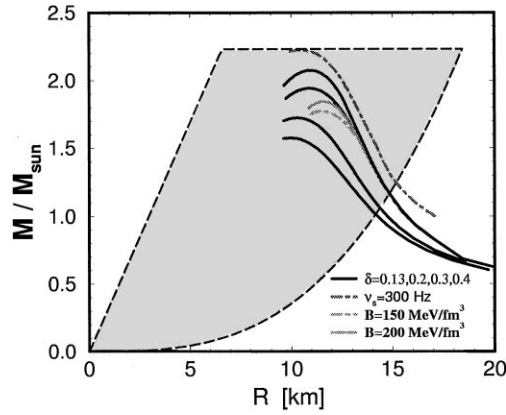


Fig. 33. Neutron star masses vs. radius for the EoS of Eq. (49) with softness $\delta = 0.13, 0.2, 0.3, 0.4$, with increasing values of δ from top to bottom for the full curves. Phase transitions decrease the maximum mass whereas rotation increases it. The shaded area represents the neutron star radii and masses allowed (see Eq. (93)) for orbital QPO frequencies 1060 Hz of 4U 1820-30.

The mass could be determined from the velocities of the binaries from pulse timing of the neutron star and doppler shifts in the spectral lines of its companion as well as the inclination from orbital flux variations.

Recently, also the mass of the low mass X-ray binary Cygnus X-2 has been estimated from U–B–V light curves [146]

$$M = (1.8 \pm 0.4)M_{\odot} . \quad (95)$$

The existence of such large neutron star masses will require a rather stiff EoS for nuclear matter and restricts the softening due to phase transitions severely, as will be discussed in the following subsection.

5.2. TOV and Hartle's equations

The theoretical description of a neutron star is governed by conditions imposed by general relativity. General relativity has to be taken into account for the determination of the gross properties of a star with approximately one solar mass M_{\odot} and a radius R of approximately 10 km, since relativistic effects are of the order [47]

$$M/R \sim 0.1\text{--}0.2 . \quad (96)$$

The starting point for such studies is how to determine Einstein's curvature tensor $G_{\mu\nu}$ for a massive star ($R_{\mu\nu}$, $g_{\mu\nu}$, and R denote the Ricci tensor, metric tensor, and Ricci scalar, respectively).

$$G_{\mu\nu} \equiv R_{\mu\nu} - \frac{1}{2}g_{\mu\nu}R = 8\pi T_{\mu\nu}(\varepsilon, P(\varepsilon)) . \quad (97)$$

A necessary ingredient for solving this equation is the energy-momentum tensor density $T_{\mu\nu}$, for which knowledge of the EoS, i.e. pressure P as function of the energy density ε is necessary.

For a spherically symmetric and static star, the metric has the Schwarzschild form

$$ds^2 = -e^{2\phi(r)} dt^2 + e^{2\lambda(r)} dr^2 + r^2(d\theta^2 + \sin^2\theta d\phi^2), \quad (98)$$

where the metric functions are given by

$$e^{2\lambda(r)} = (1 - \gamma(r))^{-1}, \quad (99)$$

$$e^{2\phi(r)} = e^{-2\lambda(r)} = (1 - \gamma(r)) \quad \text{for } r > R_{\text{star}}, \quad (100)$$

with

$$\gamma(r) = \begin{cases} 2M(r)/r, & r \leq R_s, \\ 2M_s/r, & r \geq R_s. \end{cases} \quad (101)$$

Einstein's equations for a static star reduce then to the familiar Tolman–Oppenheimer–Volkoff equation (TOV) [47,147,148]:

$$dP(r)/dr = -(1/r^2)(\varepsilon(r) + P(r))(M(r) + 4\pi r^3 P(r))e^{2\lambda(r)}, \quad (102)$$

where the gravitational mass $M(r)$ contained in a sphere with radius r is determined via the energy-density $\varepsilon(r)$ by

$$M(r) = 4\pi \int_0^r \varepsilon(r) r^2 dr. \quad (103)$$

The metric function $\phi(r)$ obeys the differential equation

$$\frac{d\phi}{dr} = -\frac{1}{\varepsilon(r) + P(r)} \frac{dP}{dr}, \quad (104)$$

with the boundary condition

$$\phi(r = R_s) = \frac{1}{2} \ln(1 - \gamma(R_s)). \quad (105)$$

For a given EoS, i.e. $P(\varepsilon)$, one can now solve the TOV equation by integrating them for a given central energy density ε_c from the star's centre to the star's radius, defined by $P(R_s) = 0$.

More complicated is the case of rotating stars, where due to the rotation changes occur in the pressure, energy density, etc. The energy-momentum density tensor $T_{\mu\nu}$ takes the form ($g^{\mu\nu}u_\mu u_\nu = -1$) [131,149,150]:

$$T_{\mu\nu} = T_{\mu 0}^0 + \Delta T_{\mu\nu}, \quad (106)$$

with

$$T_{\mu\nu}^0 = (\varepsilon + P)u_\mu u_\nu + P g_{\mu\nu}, \quad (107)$$

$$\Delta T_{\mu\nu} = (\Delta\varepsilon + \Delta P)u_\mu u_\nu + \Delta P g_{\mu\nu}. \quad (108)$$

P , ε , and ρ are quantities in a local inertial frame comoving with the fluid at the instant of measurement. For the rotationally deformed, axially symmetric configurations one assumes a multipole expansion up to second order (P_2 denotes the Legendre polynomial):

$$\Delta P = (\varepsilon + P)(p_0 + p_2 P_2(\cos \theta)) , \quad (109)$$

$$\Delta \varepsilon = \Delta P \frac{\partial \varepsilon}{\partial P} , \quad (110)$$

$$\Delta \rho = \Delta P \frac{\partial \rho}{\partial P} . \quad (111)$$

For the rotating and deformed star with the rotational frequency Ω one has now to deal with a generalized Schwarzschild metric, given by [151,152]

$$ds^2 = -e^{2\nu(r,\theta,\phi)} dt^2 + e^{2\psi(r,\theta,\Omega)} (d\phi - \omega(r, \Omega) dt)^2 + e^{2\mu(r,\theta,\phi)} d\theta^2 + e^{2\lambda(r,\theta,\phi)} dr^2 + \mathcal{O}(\Omega^3). \quad (112)$$

Here, $\omega(r)$ denotes the angular velocity of the local inertial frame, which, due to the dragging of the local system is proportional to Ω .

The metric functions of Eq. (112) which correspond to stationary rotation and axial symmetry with respect to the axis of rotation are expanded up to second order as (independent of ϕ and t)

$$e^{2\nu(r,\theta,\Omega)} = e^{2\phi(r)} [1 + 2(h_0(r, \Omega) + h_2(r, \Omega) P_2(\cos \theta))] , \quad (113)$$

$$e^{2\psi(r,\phi,\Omega)} = r^2 \sin^2 \theta [1 + 2(v_2(r, \Omega) - h_2(r, \Omega)) P_2(\cos \theta)] , \quad (114)$$

$$e^{2\mu(r,\theta,\Omega)} = r^2 [1 + 2(v_2(r, \Omega) - h_2(r, \Omega)) P_2(\cos \theta)] , \quad (115)$$

$$e^{2\lambda(r,\theta,\Omega)} = e^{2\wedge(r)} \left[1 + \frac{2}{r} \frac{m_0(r, \Omega) G + m_2(r, \Omega) P_2(\cos \theta)}{1 - \gamma(r)} \right] . \quad (116)$$

The angular velocity in the local inertial frame is determined by the differential equation

$$\frac{d}{dr} \left(r^4 j(r) \frac{d\omega}{dr} \right) + 4r^3 \frac{dj(r)}{dr} \omega(r) = 0, \quad r < R_s , \quad (117)$$

where $\omega(r)$ is regular for $r = 0$ with $d\omega/dr = 0$. $j(r)$ abbreviates

$$j(r) \equiv e^{-\phi(r)} \sqrt{1 - \gamma(r)} . \quad (118)$$

Outside the star $\omega(r, \Omega)$ is given by

$$\omega(r, \Omega) = \Omega - \frac{2}{r^3} J(\Omega), \quad r > R_s . \quad (119)$$

The total angular momentum is defined by

$$J(\Omega) = \frac{R_s^4}{6} \left(\frac{d\omega}{dr} \right)_{r=R_s} . \quad (120)$$

From the last two equations one obtains then an angular frequency Ω as a function of central angular velocity $\omega_c = \omega(r=0)$ (starting value for the iteration):

$$\Omega(\omega_c) = \omega(R_s) + \frac{2}{R_s^3} J(\Omega) . \quad (121)$$

Due to the linearity of Eq. (117) for $\omega(r)$ new values for $\omega(r)$ emerge simply by rescaling of ω_c . The momentum of inertia, defined by $I = J/\Omega$, is given by

$$I = \frac{J(\Omega)}{\Omega} = \frac{8\pi}{3} \int_0^{R_s} dv r^4 \frac{\varepsilon + P}{\sqrt{1-\gamma(r)}} \frac{\omega - \Omega}{\Omega} e^{-\phi} . \quad (122)$$

Relativistic changes from the Newtonian value are caused by the dragging of the local systems, i.e. $\bar{\omega}/\Omega$, the redshift ($e^{-\phi}$), and the space-curvature ($(1-\gamma(r))^{-1/2}$). For slowly rotating stars with low masses, one can neglect the dragging ($(\omega/\Omega) \rightarrow 1$) and rotational deformations, but we would like to emphasize that the described treatment is not restricted by low masses and/or slow rotations.

With $\omega(r)$, one can also solve the coupled mass monopole equations ($\ell = 0$) for m_0, p_0 , where the latter represents the monopole pressure perturbation, and h_0 , Refs. [131,149]. The quadrupole distortions h_2 and v_2 ($\ell = 2$) determine the star's shape (see Refs. [131,149]). We will here just state the equations for the monopole functions m_0 and p_0 in order to obtain the corrections to the mass due to rotation. We will not deal with quadrupole corrections in this work. The equations read

$$\frac{dm_0}{dr} = 4\pi^2 \frac{\partial \varepsilon}{\partial P} (\varepsilon + P) p_0 + \frac{1}{12} j^2 r^4 \left(\frac{d\omega}{dr} \right)^2 + \frac{8\pi}{3} r^4 j^2 \frac{\varepsilon + P}{1-\gamma} \omega^2 , \quad (123)$$

and

$$\frac{dp_0}{dr} = -\frac{1 + 8\pi^2 P}{r^2(1-\gamma)^2} m_0 - 4\pi \frac{(\varepsilon + P)}{1-\gamma} p_0 + \frac{1}{12} \frac{j^2 r^3}{1-\gamma} \left(\frac{d\omega}{dr} \right)^2 + \frac{1}{3} \frac{d}{dr} \left(\frac{r^2 j^2 \omega^2}{1-\gamma} \right) . \quad (124)$$

The boundary conditions are $m_0 \rightarrow 0$ and $p_0 \rightarrow 0$ when $r \rightarrow 0$. Outside the star one has

$$m_0 = \Delta M - (1/r^3) J(\Omega)^2 , \quad r > R_s ,$$

with ΔM being the rotational correction to the gravitational mass. This corrections is given by

$$\Delta M = m_0 + (1/R_s^3) J(\Omega)^2 , \quad (125)$$

at the surface of the star. Thus, when we solve the monopole equations we know also the correction to the gravitational mass. These two equations, together with Eqs. (102)–(104) and (117) form the starting point for our numerical procedure for obtaining the total mass, radius, moment of Inertia and rotational mass. Results for various approaches to the EoS are discussed in the next subsection.

5.3. Neutron star properties from various equations of state

For a given EoS we obtain the mass and radii of the neutron star by solving the equations for a weakly rotating neutron star as given by Hartle [147] and discussed in Eqs. (102)–(104), (117), (123) and (124). Various results with and without rotational corrections are displayed in Figs. 34–42, where we show total masses, mass–radius relations and moments of inertia for various approximations to the EoS. The following possible properties pertain to the various approximations to the EoS.

- For the EoS parametrization of Akmal et al. [14] with just pn degrees of freedom, the EoS with $\delta = 0.13$ gives the stiffest EoS and thereby the largest neutron star mass. For $\delta < 0.13$ the EoS is superluminal. See also the discussion in connection with Figs. 18 and 19. For $\delta = 0.3$ or $\delta = 0.4$

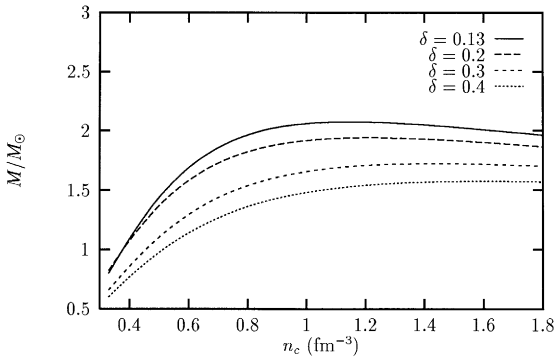


Fig. 34. Total mass M for various values of δ . See text for further details.

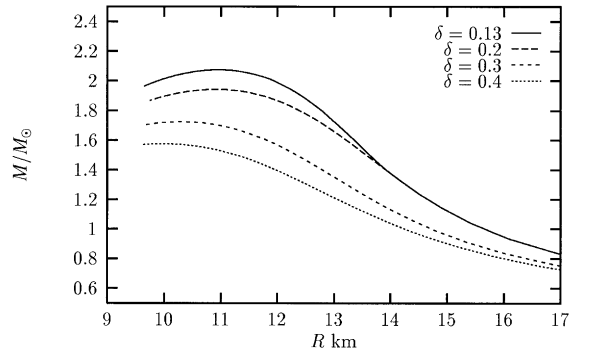


Fig. 35. Mass–radius relation for various values of δ .

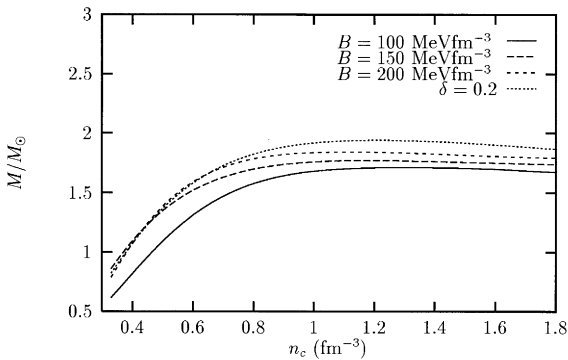


Fig. 36. Total mass M for various values of the bag parameter B for the mixed phase EoS. For comparison we include also the results from the pn -matter EoS for β -stable with $\delta = 0.2$.

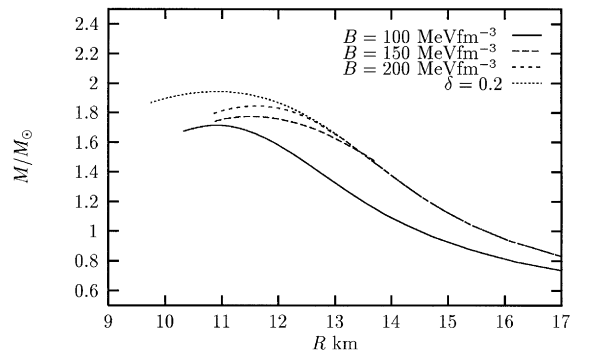


Fig. 37. Mass–radius relation for various values of the bag parameter B for the mixed phase EoS. For comparison we include also the results from the pn -matter EoS for β -stable with $\delta = 0.2$.

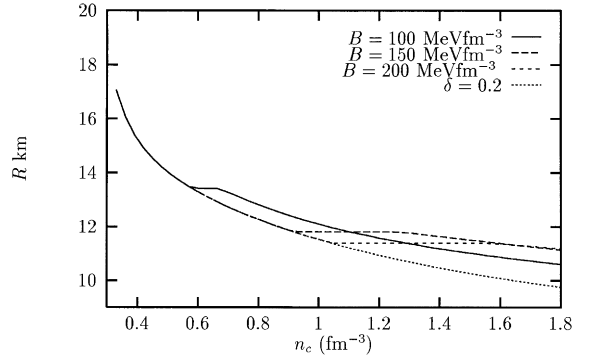
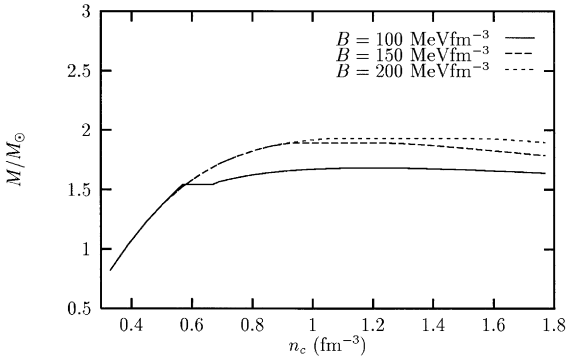


Fig. 38. Total mass M for various values of the bag parameter B for the Maxwell constructed EoS. For $B = 100 \text{ MeV fm}^{-3}$, the pure pn phase ends at 0.58 fm^{-3} and the pure quark phase starts at 0.67 fm^{-3} . For $B = 150 \text{ MeV fm}^{-3}$, the numbers are 0.92 and 1.215 fm^{-3} , while the corresponding numbers for $B = 200 \text{ MeV fm}^{-3}$ are 1.04 and 1.57 fm^{-3} . In the density regions where the two phases coexist, the pressure is constant, a fact reflected in the constant value of the neutron star mass.

Fig. 39. Radius as function of central density n_c for various values of the bag parameter B for the Maxwell constructed EoS. For comparison we include also the results from the pn -matter EoS for β -stable with $\delta = 0.2$. The region where R is constant reflects the density region where the pressure is constant in the Maxwell construction. See also the figure caption to the previous figure.

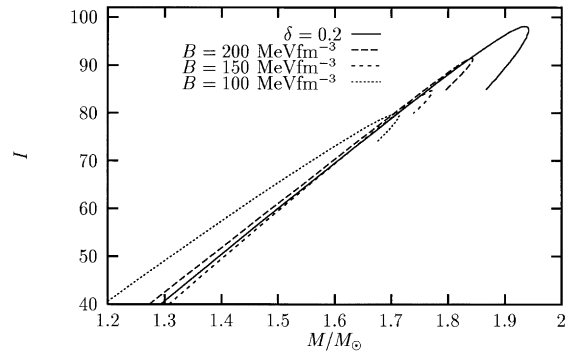
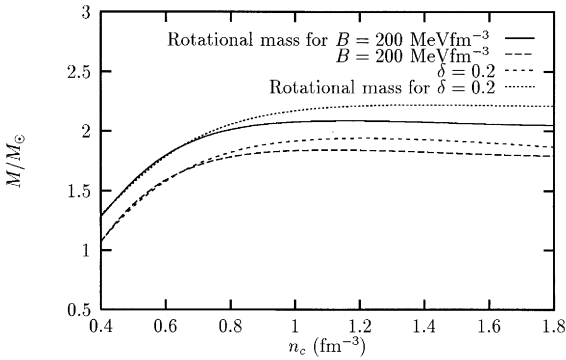


Fig. 40. Rotational mass M and gravitational mass for the pure pn EoS with $\delta = 0.2$ and equations of state based on the mixed phase construction for different values of B .

Fig. 41. Moment of Inertia I in units of $M_\odot \text{ km}^2$ as function of M_\odot for the pure pn EoS with $\delta = 0.2$ and for the mixed phase construction with $B = 200 \text{ MeV fm}^{-3}$.

the EoS differs from that with $\delta = 0.2$ or $\delta = 0.13$ at densities below $n = 0.3 \text{ fm}^{-3}$. This explains the differences in masses seen at low central densities in Fig. 34. The reader should also recall that in Section 2, the best fit to the results of Ref. [14] was obtained with $\delta = 0.2$.

- We have selected three representative values for the Bag-model parameter B , namely, 100 , 150 and 200 MeV fm^{-3} . For $B = 100 \text{ MeV fm}^{-3}$, the mixed phase starts already at 0.22 fm^{-3} and

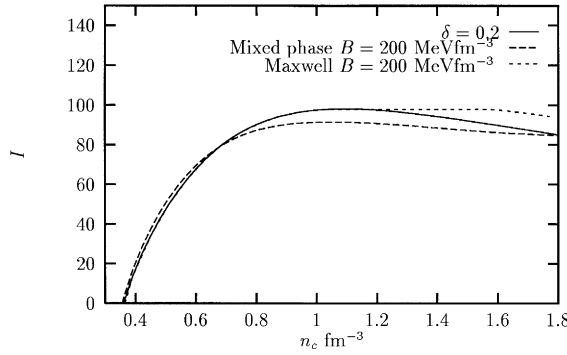


Fig. 42. Moment of Inertia I in units of $M_\odot \text{ km}^2$ as function of central density n_c for the pn EoS with $\delta = 0.2$ and with quark degrees of freedom with $B = 200 \text{ MeV fm}^{-3}$ for the mixed phase and Maxwell constructions. Note well that the Maxwell construction yields a constant I since the pressure is constant in this case in the density region from 1.04 to 1.57 fm^{-3} .

the pure quark phase starts at 1.54 fm^{-3} . For $B = 150 \text{ MeV fm}^{-3}$, the mixed phase begins at 0.51 fm^{-3} and the pure quark matter phase begins at 1.89 fm^{-3} . Finally, for $B = 200 \text{ MeV fm}^{-3}$, the mixed phase starts at 0.72 MeV fm^{-3} while the pure quark phase starts at 2.11 fm^{-3} .

- In case of a Maxwell construction, in order to link the hadronic and the quark matter EoS, we obtain for $B = 100 \text{ MeV fm}^{-3}$ that the pure pn phase ends at 0.58 fm^{-3} and that the pure quark phase starts at 0.67 fm^{-3} . For $B = 150 \text{ MeV fm}^{-3}$, the numbers are 0.92 and 1.215 fm^{-3} , while the corresponding numbers for $B = 200 \text{ MeV fm}^{-3}$ are 1.04 and 1.57 fm^{-3} .

As can be seen from Figs. 34, 36, 38, 40 and 42, none of the equations of state from either the pure pn phase or with a mixed phase construction with quark degrees of freedom, result in stable configurations for densities above $\approx 10n_0$, implying thereby, see e.g. Figs. 36 and 40, that none of the stars have cores with a pure quark phase. The EoS with pn degrees of freedom only results in the largest mass $\approx 2.2M_\odot$ when the rotational correction of Eq. (125) is accounted for, see Fig. 40. With the inclusion of the mixed phase, the total mass is reduced since the EoS is softer.

Several interesting conclusions can be inferred from the results displayed in Figs. 34–42. Firstly, to obtain neutron star masses of the order $M \sim 2.2M_\odot$ as may now have been observed in QPO's, we need the stiffest EoS allowed by causality (i.e. $\delta \simeq 0.13\text{--}0.2$) and to include rotation, see Figs. 34 and 40. Furthermore, a phase transition to quark matter below densities of order $\sim 5n_0$ can be excluded, corresponding to restricting the Bag constant to $B \gtrsim 200 \text{ MeV fm}^{-3}$. This can be seen in Fig. 36 where we plot star masses as function of the central density n_c and bag-model parameter B . These results differ from those of Akmal et al. and Kalogera and Baym [14,85] due to the very different recipes we use to incorporate causality at high densities. In Refs. [14,85] the EoS is discontinuously stiffened by taking $v_s = c$ at densities above a certain value n_c which, however, is lower than $n_s = 5n_0$ where their nuclear EoS becomes superluminal. This stiffens the nuclear EoS for densities $n_c < n < n_s$ but softens it at higher densities. Their resulting maximum masses are in the range $2.2M_\odot < M < 3M_\odot$. Our approach incorporates causality by reducing the sound speed smoothly towards the speed of light at high densities. Therefore, our maximum mass never exceeds

Table 2

Maximum gravitational mass in M_\odot and the corresponding radius R , in units of km, for the given central density n_c , in units of fm^{-3} , for various equations of state. The maximum moment of Inertia I , in units of $M_\odot \text{ km}^2$, is also listed. Note that this occurs for another central density than listed below. All results are for β -stable matter and rotational corrections have not been included in the total mass

EoS	Max mass	Max I	R	n_c
$pn \ \delta = 0.13$	2.07	110.1	11.0	1.1
$pn \ \delta = 0.2$	1.94	98.0	10.8	1.2
$pn \ \delta = 0.3$	1.72	78.7	10.3	1.4
$pn \ \delta = 0.4$	1.58	66.9	10.0	1.6
Mixed phase with $\delta = 0.2$				
$B = 200 \text{ MeV fm}^{-3}$	1.84	91.5	11.6	1.1
$B = 150 \text{ MeV fm}^{-3}$	1.77	84.7	11.5	1.2
$B = 100 \text{ MeV fm}^{-3}$	1.71	79.9	10.9	1.3

that of the nuclear EoS of Akmal et al. [14]. In fact, one may argue that at very high densities particles become relativistic and the sound speed should be even lower, $v_s^2 \simeq c^2/3$. On the other hand, if it turns out that the QPOs are not from the innermost stable orbits and that even accreting neutron stars have small masses, say like the binary pulsars $M \lesssim 1.5M_\odot$, this may indicate that heavier neutron stars are not stable. Therefore, the EoS is soft at high densities $\delta \gtrsim 0.4$ or that a phase transition occurs at a few times nuclear matter densities. For the nuclear to quark matter transition this would require $B \lesssim 80 \text{ MeV fm}^{-3}$ for $\delta = 0.2$. For such small Bag parameters there is an appreciable quark and nuclear matter mixed phase in the neutron star interior but even in these extreme cases a pure quark matter core is not obtained for stable neutron star configurations.

Finally, we end this subsection by listing in Table 2 the maximum values for masses, radii and moments of inertia for several of the equations of state discussed in Figs. 34–42. From this table we see that the pn EoS with the lowest value of δ gives also the stiffest EoS, and thereby largest mass and smallest central density. Similarly, the largest value for the bag constant results also in the stiffest EoS. In connection with the discussion of QPO's, it is worth pointing out that in Kerr space the relation between the Keplerian orbital frequency ν_K and the mass of the star is $2.198M_\odot (\nu_K \text{ kHz})^{-1} (1 - 0.748j)^{-1}$ with $j = I\omega/M^2$ a dimensionless measure of the angular momentum of the star.⁸ Following Ref. [143] and inserting the 1171 Hz QPO from 4U 1636-536, a rotational frequency $\omega/2\pi = 272 \text{ Hz}$ and an assumed moment of inertia of $\sim 100M_\odot \text{ km}^2$ results in a mass of $2.02M_\odot$ and a radius of $9.6 \pm 0.6 \text{ km}$. From the above table, we see that these results are fairly close to those which we get for the pure pn EoS with $\delta = 0.2$, i.e. for the δ value which gave the best fit to the EoS of Akmal et al. [14]. Thus, if QPO's occur near the innermost stable orbits, then neutron star masses are $M \simeq 2.2M_\odot$. This constrains the nuclear EoS including

⁸ Recall that in all equations $G = c = \hbar = 1$.

causality in a smooth way to only the stiffest ones – specifically $\delta \lesssim 0.2$ in the EoS of Eq. (49). Phase transitions in cores of neutron stars softens the EoS and strong transitions can therefore be ruled out except at very high densities $n \gtrsim 5n_0$. On the other hand, if it turns out that the QPO are not from the innermost stable orbits and that even accreting neutron stars have small masses, say like the binary pulsars $M \lesssim 1.5M_\odot$, this indicates that heavier neutron stars are not stable. Therefore, the EoS must be soft at high densities, i.e. $\delta \gtrsim 0.4$ or that a phase transition occurs at a few times nuclear matter densities.

We end this subsection with a discussion on hyperon degrees of freedom, see Section 2.4. Compared with the EoS of Eq. (49) with $\delta = 0.2$, the softening of the EoS due to the presence of hyperons lowers the maximum mass of a neutron star from $\sim 2M_\odot$ to $1.3M_\odot$. Including rotational corrections to the total mass leads to a maximum mass of $1.4M_\odot$. The hyperon formation mechanisms is perhaps the most robust one and is likely to occur in the interior of a neutron star, unless the hyperon self-energies are strongly repulsive due to repulsive hyperon–nucleon and hyperon–hyperon interactions, a repulsion which would contradict present data on hypernuclei [153]. The EoS with hyperons yields however neutron star masses without rotational corrections which are even below $\sim 1.4M_\odot$. This means that our EoS with hyperons needs to be stiffer, a fact which may in turn imply that more complicated many-body terms not included in our calculations, such as three-body forces between nucleons and hyperons and/or relativistic effects, are needed.

The role of phase transitions and its possible link with observation will be discussed in the following subsections.

5.4. Maximum masses

A stellar object of mass $\sim 1.4M_\odot$ can either be an ordinary star of type F, a white dwarf, a neutron star, a black hole, or possibly a quark star, see Fig. 43. As shown by Fechner and Joss [10] a second branch of quark stars are possible for certain equation of states (EoS) – specifically

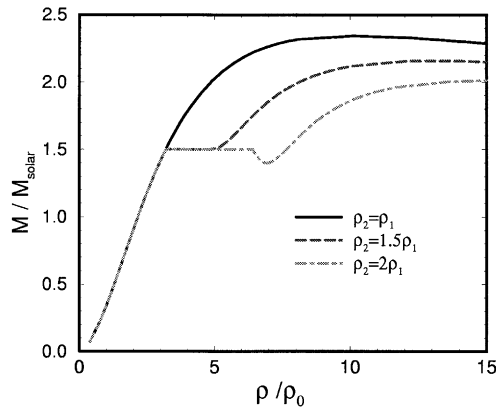


Fig. 43. Mass vs. central density for the Bethe–Johnson polytrope ($\Gamma = 2.54$) [157] with first-order phase transitions at $\varepsilon_1 = 3.2\varepsilon_0$ to ε_2 . A region of instability occurs when Eq. (129) is fulfilled.

for some parameter values of the Bag constant. The stars considered were hybrid stars consisting of a quark matter core with a mantle of nuclear matter around. A double maximum mass in the mass-density plot for neutron and mixed phase quark stars have also been found in [154] (see also [155,156]).

The occurrence of a second maximum is a curious phenomenon that occurs under specific conditions that can be quantified. For that purpose we first consider a simple model that can be solved analytically, namely an EoS consisting of two incompressible fluids with a first-order phase transition between energy density ε_1 and ε_2 ($\varepsilon_1 < \varepsilon_2$) coexisting at a pressure P_0 . We shall also first ignore effects of general relativity, i.e. take the Newtonian limit.

The mass, $M(r) = 4\pi \int_0^r \varepsilon(r') r'^2 dr'$, is very simple in the Newtonian limit and the boundary condition $M(R) = M$ relates the star mass M and radius R to the radius of the dense core, R_0 , as

$$M(R) = (4\pi/3)(\varepsilon_1 R^3 + (\varepsilon_2 - \varepsilon_1)R_0^3), \quad (126)$$

where R_0 is the radius of the dense core. From Newton's equation for hydrostatic equilibrium

$$dP/dr = -\varepsilon M(r)/r^2, \quad (127)$$

the pressure is easily obtained. From the boundary condition $P(R) = 0$ we obtain

$$P_0 = (4\pi/3)\varepsilon_1^2(R^2 + (2\varepsilon_2/\varepsilon_1 - 3)R_0^2 - (\varepsilon_2/\varepsilon_1 - 1)R_0^3/R). \quad (128)$$

When the dense core is small, $R_0 \ll R$, the R_0^3 terms in Eqs. (126) and (128) can be ignored. From Eq. (128) we therefore observe that when $2\varepsilon_2 > 3\varepsilon_1$, the radius R of the star *decreases* with increasing size of the dense core R_0 . Correspondingly, its mass $M(R)$ of Eq. (126) decreases. In other words, as the average density of the star increases, its mass decreases and a stability analysis reveals that the star is unstable. It will contract until R_0 is comparable to R such that the R_0^3 terms in Eqs. (126) and (128) stabilizes the star and its mass again increases with increasing size. We can therefore conclude that when

$$\varepsilon_2 \geq \frac{3}{2}\varepsilon_1 \Rightarrow \text{instability region}, \quad (129)$$

a second maximum mass appears.

Another case, that can be solved analytically, is the $\Gamma = 2$ polytropic EoS, $P \propto \varepsilon^2$. In this case the Newtonian version of the TOV equation is equivalent to the Schrödinger equation in a square well (or the Klein–Gordon equation) with solution $\varepsilon(r) \propto \sin(\pi r/R)/r$. Including a first-order phase transition leads to a phase shift in the corresponding sine solution for the outer mantle at densities $\varepsilon \leq \varepsilon_1$. Curiously, one finds exactly the same instability criteria as Eq. (129). However, varying the polytropic index around $\Gamma = 2$ does change this condition slightly. Also, including general relativity affects the instability condition of Eq. (129) when ε_2 is close to the maximum central density where the star becomes unstable with respect to a collapse to a black hole, see Fig. 43. A second-order phase transition as, e.g. the mixed nuclear and quark matter phase, can also lead to instabilities and second maximum masses when the EoS is sufficiently softened [154].

5.5. Phase transitions in rotating neutron stars

During the last years, and as discussed in the preceding sections, interesting phase transitions in nuclear matter to quark matter, mixed phases of quark and nuclear matter [6,11], kaon [12] or pion condensates [14], neutron and proton superfluidity [9], hyperonic matter [15,17,18] crystal-line nuclear matter, magnetized matter, etc., have been considered. Recently, Glendenning et al. [7] have considered rapidly rotating neutron stars and what happens as they slow down when the decreasing centrifugal force leads to increasing core pressures. They find that a drastic softening of the equation of state, e.g. by a phase transition to quark matter, can lead to a sudden contraction of the neutron star at a critical angular velocity and shows up in a backbending moment of inertia as function of frequency. Here we consider another interesting phenomenon namely how the star and in particular its moment of inertia behaves near the critical angular velocity where the core pressure just exceeds that needed to make a phase transition. We calculate the moment of inertia, angular velocities, braking index, etc. near the critical angular velocity and discuss observational consequences for first- and second-order phase transitions.

Here we will make the standard approximation of slowly rotating stars, i.e. the rotational angular velocity is $\Omega^2 \ll M/R^3$. For neutron stars with mass $M = 1.4M_\odot$ and radius $R \sim 10$ km their period should thus be larger than a few milliseconds, a fact which applies to all measured pulsars insofar. The general relativistic equations for slowly rotating stars were presented by Hartle [147] and reviewed in Section 5.2. Hartle's equations are quite elaborate to solve as they consist of six coupled differential equations as compared to the single Tolman–Oppenheimer–Volkoff equation in Eq. (102) in the non-rotating case. In order to be able to analytically extract the qualitative behavior near the critical angular velocity Ω_0 , where a phase transition occurs in the center, we will first solve the Newtonian equations for a simple equation of state. This will allow us to make general predictions on properties of rotating neutrons stars when phase transitions occur in the interior of a star. The corrections from general relativity are typically of order $M/R \simeq 10$ –20% for neutron stars of mass $M \simeq 1.4M_\odot$. The extracted analytical properties of a rotating star are then checked below by actually solving Hartle's equations numerically for a realistic equation of state.

The simple Newtonian equation of motion expresses the balance between the pressure gradient and the gravitational and centrifugal forces

$$\nabla P = -\varepsilon(\nabla V + \Omega \times \Omega \times \mathbf{r}) . \quad (130)$$

Here, $V(\mathbf{r})$ is the gravitational potential for the deformed star and ε the energy (\sim mass) density. We assume that friction in the (non-superfluid) matter insures that the star is uniformly rotating. Since cold neutron stars are barotropes, i.e. the pressure is a function of density, the pressure, density and effective gravitational potential, $\Phi = V - \frac{1}{2}(\Omega \times \mathbf{r})^2$, are all constants on the *same* isobaric surfaces for a uniformly rotating star [147]. We denote these surfaces by the effective radius, a , and for slowly rotating stars it is related to the distance r from the center and the polar angle θ from the rotation axis along Ω by [147]

$$r(a, \theta) = a[1 - \varepsilon(a)P_2(\cos \theta)] , \quad (131)$$

where $P_2(\cos \theta)$ is the 2nd Legendre polynomial and $\varepsilon(a)$ is the deformation of the star from spherical symmetry.

Inserting Eq. (131) in Eq. (130) one obtains for small deformations [147] the $l = 0$ Newtonian hydrostatic equation

$$(1/\varepsilon)dP/da = -M(a)/a^2 + \frac{2}{3}\Omega^2 a, \quad (132)$$

where $M(a) = 4\pi \int_0^a \varepsilon(a') a'^2 da'$ is the mass contained inside the mean radius a . The factor $\frac{2}{3}$ in the centrifugal force arises because it only acts in two of the three directions. The equation ($l = 2$) for the deformation $\varepsilon(a)$ is [158]

$$\left(\frac{1}{a^2} \frac{d\varepsilon}{da}\right) M(a) - 4\pi \int_a^R \rho(a') \frac{d\varepsilon(a')}{da'} da' = \frac{5}{3}\Omega^2. \quad (133)$$

The deformation generally increases with decreasing density, i.e. the star is more deformed in its outer layers.

In order to discuss the qualitative behavior near critical angular velocities we first consider a simple EoS with phase transitions for which Eq. (132) can be solved analytically namely that of two incompressible fluids with a first-order phase transition between energy density ε_1 and ε_2 ($\varepsilon_1 < \varepsilon_2$) coexisting at a pressure P_0 . The mass $M(a)$ is very simple in the Newtonian limit and the boundary condition $M(R) = M$ relates the star radius R to the radius of the dense core, R_0 , as

$$R = (\bar{R}^3 - (\varepsilon_2/\varepsilon_1 - 1)R_0^3)^{1/3}, \quad (134)$$

where $\bar{R} = (3M/4\pi\varepsilon_1)^{1/3}$ is the star radius in the absence of a dense core. Solving Eq. (132) gives the pressure

$$P(a) = P_0 + \frac{1}{2}(R_0^2 - a^2)\varepsilon_2((4\pi/3)\varepsilon_2 - \frac{2}{3}\Omega^2), \quad (135)$$

for $0 \leq a \leq R_0$ and

$$P(a) = P_0 + \frac{1}{2}(R_0^2 - a^2)\varepsilon_1((4\pi/3)\varepsilon_1 - \frac{2}{3}\Omega^2) - (4\pi/3)R_0^2(\varepsilon_2 - \varepsilon_1)\varepsilon_1(1 - (R_0/a)), \quad (136)$$

for $R_0 \leq a \leq R$ [8]. The boundary condition at the surface $P(R) = 0$ in Eq. (136) gives

$$\omega^2 \equiv \frac{\Omega^2}{2\pi\varepsilon_1} = 1 - 2\left(\frac{3}{4\pi\varepsilon_1^2} \frac{P_0}{R^2} + \left(\frac{\varepsilon_2}{\varepsilon_1} - 1\right) \frac{R_0^2}{R^2}(1 - R_0/R)\right)(1 - R_0^2/R^2)^{-1}. \quad (137)$$

The phase transition occurs right at the center when $R_0 = 0$ corresponding to the *critical angular velocity* $\Omega_0 = \omega_0 \sqrt{2\pi\varepsilon_1}$, where [8]

$$\omega_0^2 = 1 - 2P_0\bar{R}/M. \quad (138)$$

Generally, for any EoS the critical angular velocity depends on P_0 , M , and ε_1 but not on ε_2 .

For angular velocities just below ω_0 very little of the high-density phase exists and $R_0 \ll R$. Expanding (137) we obtain

$$\frac{R_0}{\bar{R}} \simeq \sqrt{\frac{\omega_0^2 - \omega^2}{3 - 2\varepsilon_2/\varepsilon_1 - \omega_0^2}}. \quad (139)$$

For $\omega \geq \omega_0$ the dense phase disappears and $R_0 = 0$. Generally, one can interpret R_0 as an order parameter in analogy to, e.g. magnetization, the BCS gap, or the Higgs field in the standard model, however, as function of angular velocity instead of temperature. Note, that for large density differences, $\varepsilon_2/\varepsilon_1 \geq (3 - \omega_0^2)/2$, Eq. (139) is not valid. This is related to an instability (see Eq. (129)) and will be discussed in the following subsection.

The corresponding moment of inertia is for $R_0 \ll R$

$$I = (4\pi/5)(\varepsilon_2 R_0^5 + \varepsilon_1 (R^5 - R_0^5))(1 + \frac{2}{5}\varepsilon) \\ \simeq \frac{2}{5}M\bar{R}^2(1 - \frac{5}{3}((\varepsilon_2/\varepsilon_1) - 1)R_0^3/\bar{R}^3)(1 + \frac{1}{2}\omega^2), \quad (140)$$

where we used that the deformation from Eq. (133) is $\varepsilon = \frac{5}{4}\omega^2$ in the low density phase [158]. However, for the qualitative behavior near Ω_0 only the contraction of the star radius R with the appearance of the dense core R_0 is important whereas the deformations can be ignored. The contraction is responsible for the term in the moment of inertia and is proportional to $R_0^3 \propto (\omega_0^2 - \omega)^{3/2}$ near the critical angular velocity. Consequently, the derivative $dI/d\omega^2$ displays the same non-analytic square root dependence as R_0 (see Eq. (139)).

Latent heat is generated in the phase transition can be ignored because of rapid neutrino cooling which will be even faster than in supernova explosions. Thus temperatures will drop below ~ 1 MeV in seconds. Such temperatures are negligible compared to typical Fermi energies of nucleons or quarks and the timescales are also much smaller than t_0 .

Let us subsequently consider a more realistic EoS for dense nuclear matter at high densities such as the Bethe–Johnson EoS [157]. At high densities it can be approximated by a polytropic relation between the pressure and energy density: $P = K_1 \varepsilon^{2.54}$, where $K_1 = 0.021\varepsilon_0^{-1.54}$ and $\varepsilon_0 = m_n 0.15 \text{ fm}^{-3}$ is normal nuclear matter mass density. As we are only interested in the dense core we will for simplicity employ this Bethe–Johnson polytrope (BJP) EoS. The central density of a non-rotating $1.4M_\odot$ mass neutron star with the BJP EoS is $\sim 3.4\varepsilon_0$. Furthermore, we assume that a first-order phase transition occurs at density $\varepsilon_1 = 3.2\varepsilon_0$ to a high-density phase of density $\varepsilon_2 = 4\varepsilon_0$ with a similar polytropic EoS $P = K_2 \varepsilon^{2.54}$. From the Maxwell construction the pressure is the same at the interface, P_0 , which determines $K_2 = K_1(\varepsilon_1/\varepsilon_2)^{2.54}$. We now generalize Eq. (132) by including effects of general relativity. From Einstein’s field equations for the metric we obtain from the $l = 0$ part

$$\frac{1}{\varepsilon + P} \frac{dP}{da} = - \frac{M(a) + 4\pi a^3 P}{a^2(1 - 2M(a)/a)} + \frac{2}{3}\Omega^2 a, \quad (141)$$

where $m(a) = 4\pi \int_0^a \varepsilon(a') a'^2 da'$. In the centrifugal force term we have ignored frame dragging and other corrections of order $\Omega^2 M/R \sim 0.1\Omega^2$ for simplicity and since they have only minor effects in our case. By expanding the pressure, mass and gravitational potential in the difference between the rotating and non-rotating case, Eq. (141) reduces to the $l = 0$ part of Hartle’s equations (cf. Eq. (100) in [147]). Note also that Hartle’s full equations cannot be used in our case because the first-order phase transition causes discontinuities in densities so that changes are not small locally. This shows up, for example, in the divergent thermodynamic derivative $d\varepsilon/dP$.

The rotating version of the Tolman–Oppenheimer–Volkoff Equation (141) is now solved for a rotating neutron star of mass $M = 1.4M_\odot$ with the BJP EoS including a first-order phase

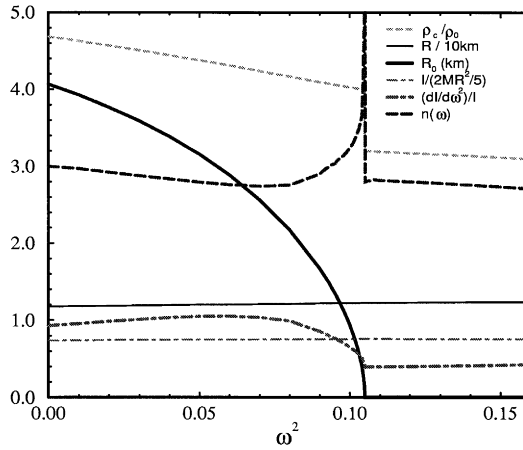


Fig. 44. Central density (in units of ε_0), radii of the neutron star R and its dense core R_0 , moment of inertia, its derivative $I'/I = dI/d\omega^2/I$ and the braking index are shown as function of the scaled angular velocity $\omega^2 = \Omega^2/(2\pi\varepsilon_1)$. The rotating neutron star has mass $1.4M_\odot$ and a Bethe–Johnson-like polytropic equation of state with a first-order phase transition taking place at density $\varepsilon_1 = 3.2\varepsilon_0$ to $\varepsilon_2 = 4\varepsilon_0$.

transition. In Fig. 44 we show the central density, moment of inertia, braking index, star radius and radius of the interface (R_0) as function of the scaled angular velocity. It is important to note that $R_0 \propto \sqrt{\Omega_0^2 - \Omega^2}$ for angular velocities just below the critical value Ω_0 . The qualitative behavior of the neutron star with the BJP EoS and a first-order phase transition is the same as for our simple analytic example of two incompressible fluids examined above. Generally, it is the finite density difference between the phases that is important and leads to a term in the moment of inertia proportional to $(\Omega_0^2 - \Omega^2)^{3/2}$ as in Eq. (140).

The moment of inertia increases with angular velocity. Generally, for a first-order phase transition we find for $\Omega \lesssim \Omega_0$ (see also Eq. (140) and Fig. 44)

$$I = I_0(1 + \frac{1}{2}c_1\Omega^2/\Omega_0^2 - \frac{2}{3}c_2(1 - (\Omega^2/\Omega_0^2))^{3/2} + \dots). \quad (142)$$

For the two incompressible fluids with momentum of inertia given by Eq. (140), the small expansion parameters are $c_1 = \omega_0^2$ and $c_2 = (5/2)\omega_0^3(\varepsilon_2/\varepsilon_1 - 1)/(3 - 2\varepsilon_2/\varepsilon_1 - \omega_0^2)^{3/2}$; for $\Omega > \Omega_0$ the c_2 term is absent. For the BJP we find from Fig. 1 that $c_2 \simeq 0.07 \simeq 2.2\omega_0^3$. Generally, we find that the coefficient c_2 is proportional to the density difference between the two coexisting phases and to the critical angular velocity to the third power, $c_2 \sim (\varepsilon_2/\varepsilon_1 - 1)\omega_0^3$. The scaled critical angular velocity ω_0 can at most reach unity for submillisecond pulsars.

To make contact with observation we consider the temporal behavior of angular velocities of pulsars. The pulsars slow down at a rate given by the loss of rotational energy which we shall assume is proportional to the rotational angular velocity to some power (for dipole radiation $n = 3$)

$$(d/dt)(\frac{1}{2}I\Omega^2) = -C\Omega^{n+1}. \quad (143)$$

With the moment of inertia given by Eq. (142) the angular velocity will then decrease with time as

$$\begin{aligned}\frac{\dot{\Omega}}{\Omega} &= -\frac{C\Omega^{n-1}}{I_0}\left(1 - c_1\frac{\Omega^2}{\Omega_0^2} - c_2\sqrt{1 - \frac{\Omega^2}{\Omega_0^2}}\right) \\ &\simeq -\frac{1}{(n-1)t}\left(1 - c_2\sqrt{1 - \left(\frac{t_0}{t}\right)^{2/(n-1)}} + \dots\right),\end{aligned}\quad (144)$$

for $t \geq t_0$. Here, the time after formation of the pulsar is, using Eq. (143), related to the angular velocity as $t \simeq t_0(\Omega_0/\Omega)^{n-1}$ and $t_0 = I_0/((n-1)C\Omega_0^{n-1})$ for $n > 1$, is the critical time where a phase transition occurs in the center. For earlier times $t \leq t_0$ there is no dense core and Eq. (144) applies when setting $c_2 = 0$. The critical angular velocity is $\Omega_0 = \omega_0\sqrt{2\pi\epsilon_1} \simeq 6$ kHz for the BJP EoS, i.e. comparable to a millisecond binary pulsar. Applying these numbers to, for example, the Crab pulsar we find that it would have been spinning with critical angular velocity approximately a decade after the Crab supernova explosion, i.e. $t_0 \sim 10$ years for the Crab. Generally, $t_0 \propto \Omega_0^{1-n}$ and the timescale for the transients in $\dot{\Omega}$ as given by Eq. (144) may be months or centuries. In any case, it would not require continuous monitoring which would help a dedicated observational program.

The braking index depends on the second derivative $I'' = dI/d^2\Omega$ of the moment of inertia and thus diverges (see Fig. 44) as Ω approaches Ω_0 from below

$$n(\Omega) \equiv \frac{\ddot{\Omega}\Omega}{\dot{\Omega}^2} \simeq n - 2c_1\frac{\Omega^2}{\Omega_0^2} + c_2\frac{\Omega^4/\Omega_0^4}{\sqrt{1 - \Omega^2/\Omega_0^2}}. \quad (145)$$

For $\Omega \geq \Omega_0$ the term with c_2 is absent. The *observational* braking index $n(\Omega)$ should be distinguished from the *theoretical* exponent n appearing in Eq. (143). Although the results in Eqs. (144) and (145) were derived for the pulsar slow down assumed in Eq. (143) both $\dot{\Omega}$ and $n(\Omega)$ will generally display the $\sqrt{t - t_0}$ behavior for $t \geq t_0$ as long as the rotational energy loss is a smooth function of Ω . The singular behavior will, however, be smeared on the pulsar glitch “healing” time which in the case of the Crab pulsar is of order weeks only.

We now discuss possible phase transitions in interiors of neutron stars. The quark and nuclear matter mixed phase described in [6] has continuous pressures and densities. There are no first-order phase transitions but at most two second-order phase transitions. Namely, at a lower density, where quark matter first appears in nuclear matter, and at a very high density (if gravitationally stable), where all nucleons are finally dissolved into quark matter. In second-order phase transitions the pressure is a continuous function of density and we find a continuous braking index. This mixed phase does, however, not include local surface and Coulomb energies of the quark and nuclear matter structures. As shown in [11,139] there can be an appreciable surface and Coulomb energy associated with forming these structures and if the interface tension between quark and nuclear matter is too large, the mixed phase is not favored energetically. The neutron star will then have a core of pure quark matter with a mantle of nuclear matter surrounding it and the two phases are coexisting by a first order phase transition. For a small or moderate interface

tension the quarks are confined in droplet, rod- and plate-like structures [11,139] as found in the inner crust of neutron stars [34]. Due to the finite Coulomb and surface energies associated with forming these structures, the transitions change from second order to first order at each topological change in structure. If a Kaon condensate appears it may also have such structures [95]. Pion condensates [161], crystalline nuclear matter [13,14], hyperonic or magnetized matter, etc. may provide other first-order phase transitions.

If a neutron star cools continuously, the temperature will decrease with time and the phase transition boundary will move inwards. The two phases could, e.g. be quark-gluon/nuclear matter or a melted/solid phase. In the latter case the size of the hot (melted) matter in the core is slowly reduced as the temperature drops freezing the fluid into the solid mantle. Melting temperatures have been estimated in [34,137] for the crust and in [11] for the quark matter mixed phase. When the very core freezes we have a similar situation as when the star slows down to the critical angular velocity, i.e. a first-order phase transition occurs right at the center. Consequently, a similar behavior of moment of inertia, angular velocities, braking index may occur as in Eqs. (142), (144) and (145) replacing $\Omega(t)$ with $T(t)$.

Thus, if a first-order phase transitions is present at central densities of neutron stars, it will show up in moments of inertia and consequently also in angular velocities in a characteristic way. For example, the slow down of the angular velocity has a characteristic behavior $\dot{\Omega} \sim c_2 \sqrt{1 - t/t_0}$ and the braking index diverges as $n(\Omega) \sim c_2 / \sqrt{1 - \Omega^2/\Omega_0^2}$ (see Eqs. (144) and (145)). The magnitude of the signal generally depends on the density difference between the two phases and the critical angular velocity $\omega_0 = \Omega_0 / \sqrt{2\pi\epsilon_1}$ such that $c_2 \sim (\epsilon_2/\epsilon_1 - 1)\omega_0^3$. The observational consequences depend very much on the critical angular velocity Ω_0 , which depends on the equation of state employed, at which density the phase transition occurs and the mass of the neutron star.

We encourage a dedicated search for the characteristic transients discussed above. As the pulsar slows down over a million years, its central densities spans a wide range of order $1n_0$ (see Fig. 44). As we are interested in time scales of years, we must instead study all ~ 1000 pulsars available. By studying the corresponding range of angular velocities for the sample of different star masses, the chance for encountering a critical angular velocity increases. Eventually, one may be able to cover the full range of central densities and find all first-order phase transitions up to a certain size determined by the experimental resolution. Since the size of the signal scales with Ω_0^3 the transition may be best observed in rapidly rotating pulsars such as binary pulsars or pulsars recently formed in supernova explosion and which are rapidly slowing down. Carefully monitoring such pulsars may reveal the characteristic behavior of the angular velocity or braking index as described above which is a signal of a first-order phase transition in dense matter.

5.6. Core quakes and glitches

The glitches observed in the Crab, Vela, and a few other pulsars are probably due to quakes occurring in solid structures such as the crust, superfluid vortices or possibly the quark matter lattice in the core [139]. As the rotating neutron star gradually slows down and becomes less deformed, the rigid component is strained and eventually cracks/quakes and changes its structure towards being more spherical.

The moment of inertia of the rigid component, I_c , decreases abruptly and its rotation and pulsar frequency increases due to angular momentum conservation resulting in a glitch. The observed

glitches are very small $\Delta\Omega/\Omega \sim 10^{-8}$. The two components slowly relaxate to a common rotational frequency on a timescale of days (healing time) due to superfluidity of the other component (the neutron liquid). The *healing parameter* $Q = I_c/I_{\text{tot}}$ measured in glitches reveals that for the Vela and Crab pulsar about $\sim 3\%$ and $\sim 96\%$ of the moment of inertia is in the rigid component respectively.

If the crust were the only rigid component the Vela neutron star should be almost all crust. This would require that the Vela is a very light neutron star – much smaller than the observed ones which all are compatible with $\sim 1.4M_\odot$. If we by the lattice component include not only the solid crust but also the protons in nuclear matter (NM) (which is locked to the crust due to magnetic fields), superfluid vortices pinned to the crust [162] and the solid QM mixed phase

$$I_c = I_{\text{crust}} + I_p + I_{sv} + I_{\text{QM}} , \quad (146)$$

we can better explain the large I_c for the Crab. The moment of inertia of the mixed phase is sensitive to the EoS's used. For example, for a quadratic NM EoS [11] decreasing the Bag constant from 110 to 95 MeV fm $^{-3}$ increases I_c/I_{total} from $\sim 20\%$ to $\sim 70\%$ for a $1.4M_\odot$ neutron star – not including possible vortex pinning. The structures in the mixed phase would exhibit anisotropic elastic properties, being rigid to some shear strains but not others in much the same way as liquid crystals. Therefore, the whole mixed phase might not be rigid.

The energy released in glitches every few years are too large to be stored in the crust only. The recurrence time for large quakes, t_c , is inversely proportional to the strain energy [162], which again is proportional to the lattice density and the Coulomb energy

$$t_c^{-1} \propto (1/a^3)Z^2e^2/a . \quad (147)$$

Since the lattice distance a is smaller for the quark matter droplets and their charge larger than for atoms in the crust, the recurrence time is shorter in better agreement with measurements of large glitches.

Detecting core and crust quakes separately or other signs of three components in glitches, indicating the existence of a crust, superfluid neutrons and a solid core, would support the idea of the mixed quark and nuclear matter mixed phase. However, magnetic field attenuation is expected to be small in neutron stars and therefore magnetic fields penetrate through the core. Thus, the crust and core lattices as well as the proton liquid should be strongly coupled and glitch simultaneously.

5.7. Backbending and giant glitches

In [7] the moment of inertia is found to “backbend” as function of angular velocity. The moment of inertia of some deformed nuclei [159,160] may also backbend when the coriolis force exceeds the pairing force breaking the pairing whereby the nucleus reverts from partial superfluidity to a rigid rotor. However, in the limit of large nuclear mass number such backbending would disappear. Instead pairing may lead to superfluidity in bulk [162]. A backbending phenomenon in neutron stars, that appears to be similar to backbending in nuclei, can occur in neutron stars although the physics behind is entirely different. If we soften the EoS significantly at a density near the central

density of the neutron star, a non-rotating neutron star can have most of its core at high densities where the soft EoS determines the profile. A rapidly rotating star may instead have lower central densities only probing the hard part of the EoS. Thus, the star may at a certain angular velocity revert from the dense phase to a more dilute one and at the same time change its structure and moment of inertia discontinuously. Such a drastic change in moment of inertia at some angular velocity will cause a giant glitch as found in [7].

The phenomenon of neutron star backbending is related to the double maximum mass for a neutron and quark star respectively as shown in Fig. 44. The instabilities given in Eq. (129) are also evident when rotation is included as seen from Eq. (139)

$$\varepsilon_2 \geq \frac{1}{2}\varepsilon_1(3 - \omega_0^2) \Rightarrow \text{Giant glitch when } \omega \simeq \omega_0 . \quad (148)$$

The Bethe–Johnson EoS discussed in Section 5.4 also has this discontinuity in the moment of inertia when $\rho_2/\rho_1 \gtrsim 3/2$. The neutron star may continue to slow down in its unstable structure, i.e. “super-rotate”, before reverting to its stable configuration with a dense core. As for the instabilities of Eq. (129) this condition changes slightly for a more general EoS and when general relativity is included. Neutron stars with a mixed phase do not have a first-order phase transition but may soften their EoS sufficiently that a similar phenomenon occurs [7]. We emphasize, however, that the discontinuous jump in moment of inertia is due to the drastic and sudden softening of the EoS near the central density of neutron stars. It is not important whether it is a phase transition or another phenomenon that causes the softening.

5.8. Cooling and temperature measurements

The thermal evolution of a neutron star may provide information about the interiors of the star, and in recent years much effort has been devoted to measuring neutron star temperatures, especially with the Einstein Observatory and ROSAT, see e.g. Ref. [163]. Neutron stars are born with interior temperatures of the order 20–50 MeV, but cool rapidly via neutrino emission to temperatures of the order 1 MeV within minutes. The only information on neutron star temperatures stems from surface temperatures, which typically are of the order 10^6 K for about 10^5 yr, observed in X-ray or UV bands. However, the thermal radiation from a neutron star has yet to be identified unambiguously. Most observations are for pulsars, and it is unclear how much of the observed radiation is due to pulsar phenomena, to a synchrotron-emitting nebula or to the neutron star itself. Surface temperatures of neutron stars have been measured in a few cases or upper limits have been set. Table 3 collects some of these.

The cooling history of the star, and energy loss mechanisms from the interior are thus to be determined through various theoretical models. The generally accepted picture is that the long-term cooling of a neutron star consists of two periods: a neutrino cooling epoch which can last until 10^6 yr and a photon cooling period. If we now assume that the main cooling mechanism in the early life of a neutron star is believed to go through neutrino emissions in the core, the most powerful energy losses are expected to be given by the so-called direct Urca mechanism

$$n \rightarrow p + l + \bar{\nu}_l, \quad p + l \rightarrow n + \nu_l , \quad (149)$$

Table 3
Luminosities, L , and spin-down ages, τ , of pulsars

Pulsar	Name	$\log \tau$ (yr)	$\log L$ (erg/s)
1706 – 44		4.25	32.8 ± 0.7 [164]
1823 – 13		4.50	33.2 ± 0.6 [165]
2334 + 61		4.61	33.1 ± 0.4 [166]
0531 + 21	Crab	3.09	33.9 ± 0.2 [167]
1509 – 58	SNR MSH 15-52	3.19	33.6 ± 0.4 [168]
0540 – 69		3.22	36.2 ± 0.2 [169]
1951 + 32	SNR CTB 80	5.02	33.8 ± 0.5 [170]
1929 + 10		6.49	28.9 ± 0.5 [171,163]
0950 + 08		7.24	29.6 ± 1.0 [172]
J0437 – 47		8.88	30.6 ± 0.4 [173]
0833 – 45	Vela	4.05	32.9 ± 0.2 [174]
0656 + 14		5.04	32.6 ± 0.3 [175]
0630 + 18	Geminga	5.51	31.8 ± 0.4 [176]
1055 – 52		5.73	33.0 ± 0.6 [177]

as rediscussed recently by several authors [178–180]. The label l refers to the leptons considered here, electrons and muons. However, in order to fulfill the momentum conservation $k_F^n < k_F^p + k_F^e$ and energy conservation requirements, the process can only start at densities n several times nuclear matter saturation density $n_0 = 0.16 \text{ fm}^{-3}$, see e.g. Fig. 18, where the proton fraction exceeds $x_p \gtrsim 0.14$, see e.g. [47,178–180].

Thus, for long time the dominant processes for neutrino emission have been the so-called modified Urca processes first discussed by Chiu and Salpeter [181], in which the two reactions

$$n + n \rightarrow p + n + l + \bar{\nu}_l, \quad p + n + l \rightarrow n + n + \nu_l, \quad (150)$$

occur in equal numbers. These reactions are just the usual processes of neutron β -decay and electron and muon capture on protons of Eq. (149), with the addition of an extra bystander neutron. They produce neutrino-antineutrino pairs, but leave the composition of matter constant on average. Eq. (150) is referred to as the neutron branch of the modified Urca process. Another branch is the proton branch

$$n + p \rightarrow p + p + l + \bar{\nu}_l, \quad p + p + l \rightarrow n + p + \nu_l, \quad (151)$$

pointed out by Itoh and Tsuneto [182] and recently reanalyzed by Yakovlev and Levenfish [183]. The latter authors showed that this process is as efficient as Eq. (150). In addition one also has the possibility of neutrino-pair bremsstrahlung. These processes form the basis for what is normally called the *standard cooling scenario*, i.e. no direct Urca processes are allowed.

A *fast cooling scenario* would involve the direct Urca process, similar direct processes with baryons more massive than the nucleon participating, such as isobars or hyperons [179,180], or neutrino emission from more exotic states like pion and kaon condensates [91,36,96] or quark

matter [30,130]. Actually, Prakash et al. [179] showed that the hyperon direct Urca processes gave a considerable contribution to the emissivity, without invoking exotic states or the large proton fractions needed in Eq. (149).

If we now consider the neutron stars discussed in Section 5.3, we note that a typical star with mass $\sim 1.4\text{--}2.0M_{\odot}$ has central densities ranging from ~ 0.5 to 1.2 fm^{-3} . Depending on the value of the bag constant, the mixed phase could start already at $\sim 0.2\text{--}0.3\text{ fm}^{-3}$. No pure quark phase was found with the bag-model for stable neutron star configurations. If one also recalls that our β -stable EoS allows for the direct Urca process at densities starting from 0.8 fm^{-3} , see Fig. 18, one clearly sees that, depending on the EoS and the adopted model for dense matter, there is a considerable model dependence. To give an example, the cooling could be strongly influenced by the mixed phase. This could come about because nuclear matter in the droplet phase has a higher proton concentration than bulk neutral nuclear matter and this could make it easier to attain the threshold condition for the nucleon direct Urca process. Another possibility is that the presence of the spatial structure of the droplet phase might allow processes to occur which would be forbidden in a translationally invariant system. Also, the mere presence of quark matter can lead to fast cooling [130] when $\alpha_s \neq 0$. All these mechanisms would lead to faster cooling.

However, in order to compare with observation, the structure of the star has to be computed in detail. In particular the possible presence of superfluidity in the interior has to be considered. The superfluid would suppress the $\nu, \bar{\nu}$ emissivity and would allow for reheating through friction with the crust. In the analysis of Page as well [184], it is hard to discriminate between fast and slow cooling scenarios, though in both cases agreement with the observed temperature of Geminga is obtained if baryon pairing is present in most, if not all of the core of the star. The recent analyses of Schaab et al. [185,186] also seem to confirm the importance of superfluidity in the interior of stars. There are also indications [187,188] that temperatures of young ($\sim 10^4$ years old) neutron stars lie below that obtained through the so-called modified Urca processes. One has also to note [184] that the modified Urca processes are weakly dependent on the mass of the star, i.e. on the central density, while faster cooling mechanisms like the above direct Urca processes are in general strongly dependent on it. Thus, the detection of two coeval stars, whose temperatures differ by a factor of the order of 2 or larger would allow to distinguish between traditional cooling scenarios, like those discussed by Page [184], and more exotic ones. Such a huge variation in the temperature of coeval stars could indicate the presence of a threshold in the cooling mechanism, triggered by the density of the star.

In Fig. 45 we display results from various cooling calculations by Schaab et al. [186]. All calculations employ a superfluidity scenario which is described in Section 2.7. This corresponds to label 4 in the above figure, while the letters A, B, C, D represent different equations of state employed to calculate the mass of the star. Label A corresponds to the non-relativistic equations of state from Wiringa et al. [90], and is similar to that of Akmal et al. [14] in Section 2, and non-relativistic equations of state based on two-body interactions only. The models encompassed by class A allow for the standard cooling scenario only at higher densities. These densities however, are beyond the central density of a $1.4M_{\odot}$ neutron star. Models B and C allow for faster cooling scenarios and the equations of state are based on relativistic mean field models. Typically, see also the discussion of relativistic effects and the proton fractions in Fig. 16, these models allow for the direct Urca for nucleons at lower densities than the non-relativistic models. Pion and kaon condensation could also lead to faster cooling scenarios. Model D allows for direct hyperon

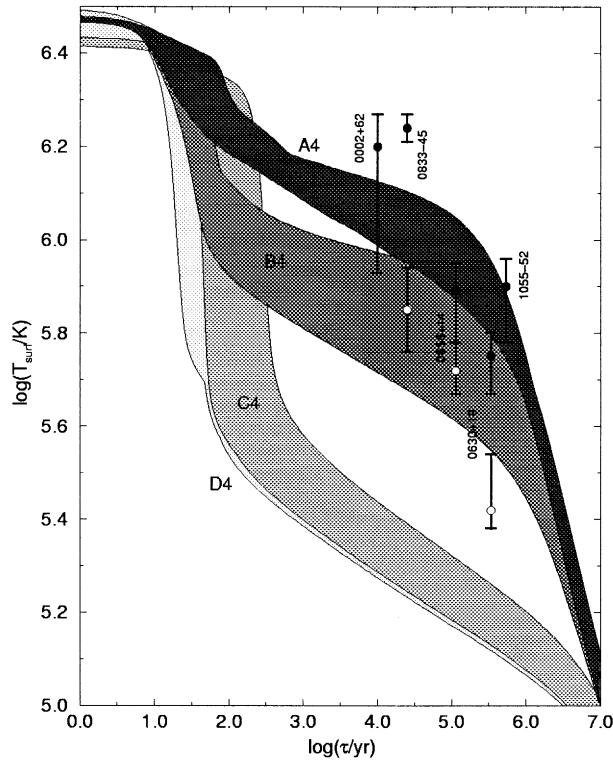


Fig. 45. Thermal evolution of a $1.4M_{\odot}$ neutron star with superfluidity. See text for further details. Taken from Ref. [186].

cooling as well but does not include hyperon pairing, which reduces strongly the direct Urca for hyperons, see Ref. [114].

The problem with most cooling calculations is that there is no consistent calculation of properties entering the neutrino emissivities within the framework of say one given EoS and many-body approach. Typically, see e.g. Refs. [185,186] and Fig. 45, the EoS is taken from one source, while the pairing gap is taken from another calculation, with even entirely different NN interactions or many-body approaches. In addition, the expressions for the emissivities of e.g. the modified Urca processes calculated by Friman and Maxwell [189] treat in a rather cavalier way the role of many-body correlations. Considering also the fact that other severe approximations are made, these expressions, which enter typically various cooling codes, could introduce errors at the level of orders of magnitude.

Thus, our message is that, before one attempts at a cooling calculation, little can be learned unless the various neutrino emissivities are reevaluated within the framework of a given many-body scheme for dense matter.

We conclude this subsection with a demonstration of the role of superfluidity for the processes of Eqs. (150)–(151) at densities corresponding to the outer core of massive neutron stars or the core of not too massive neutron stars when we have a superfluid phase. Here we limit ourselves to study the role of superconducting protons in the core of the star employing the gap for protons in the

1S_0 and effective masses from lowest-order Brueckner–Hartree–Fock calculations discussed in Sections 2, 2.2 and 2.7. The proton superconductivity reduces the energy losses considerably in the above reactions [183], and may have important consequences for the cooling of young neutron stars. The expressions for the processes in Eqs. (150) and (151) were derived by Friman and Maxwell [189] and read [183]

$$Q_n \approx 8.5 \times 10^{21} \left(\frac{m_n^*}{m_n} \right)^3 \left(\frac{m_p^*}{m_p} \right) \left(\frac{n_e}{n_0} \right)^{1/3} T_9^8 \alpha_n \beta_n, \quad (152)$$

in units of $\text{ergs cm}^{-3} \text{s}^{-1}$ where T_9 is the temperature in units of 10^9 K , and according to Friman and Maxwell α_n describes the momentum transfer dependence of the squared matrix element in the Born approximation for the production rate in the neutron branch. Similarly, β_n includes the non-Born corrections and corrections due to the nucleon–nucleon interaction not described by one-pion exchange. Friman and Maxwell [189] used $\alpha_n \approx 1.13$ at nuclear matter saturation density and $\beta_n = 0.68$. In the results presented below, we will not include α_n and β_n . For the reaction of Eq. (150) with muons, one has to replace n_e with n_μ and add a factor $(1 + X)$ with $X = k_F^\mu/k_F^e$ [190,191]. For the proton branch of Eq. (151) with electrons we have the approximate equation [183]

$$Q_p \approx 8.5 \times 10^{21} (m_p^*/m_p)^3 (m_n^*/m_n) (n_e/n_0)^{1/3} T_9^8 \alpha_p \beta_p F, \quad (153)$$

with $F = (1 - (k_F^e/4k_F^p))\Theta$, where $\Theta = 1$ if $k_F^p < 3k_F^e + k_F^e$ and zero elsewhere. Yakovlev and Levenfish [183] put $\alpha_n = \alpha_p$ and $\beta_p = \beta_n$. We will, due to the uncertainty in the determination of these coefficients, omit them in our calculations of the reaction rates. With muons, the same changes as in Eq. (152) are made.

The reaction rates for the Urca processes are reduced due to the superconducting protons. Here we adopt the results from Yakovlev and Levenfish [183], their Eqs. (31) and (32) for the neutron branch of Eq. (152) and Eqs. (35) and (37) for the proton branch of Eq. (153). We single out proton singlet-superconductivity only, employing the approximation $k_B T_C = \Delta(0)/1.76$, where T_C is the critical temperature and $\Delta(0)$ is the pairing gap at zero temperature discussed in Section 2. The critical temperature is then used to obtain the temperature dependence of the corrections to the neutrino reaction rates due to superconducting protons. To achieve that we employ Eq. (23) of [183]. We present results for the neutrino energy rates at a density $n = 0.3 \text{ fm}^{-3}$. The critical temperature is $T_C = 3.993 \times 10^9 \text{ K}$, whereas without muons we have $T_C = 4.375 \times 10^9$. The implications for the final neutrino rates are shown in Fig. 46, where we show the results for the full case with both muons and electrons for the processes of Eqs. (150) and (151). In addition, we also display the results when there is no reduction due to superconducting protons. At the density considered, $n = 0.3 \text{ fm}^{-3}$, we see that the processes of Eqs. (150) and (151) with muons are comparable in size to those of Eqs. (150) and (151) with electrons. However, the proton pairing gap is still sizable at densities up to 0.4 fm^{-3} , and yields a significant suppression of the modified Urca processes discussed here, as seen in Fig. 46. We have omitted any discussion on neutron pairing in the 3P_2 state. For this channel we find the pairing gap to be rather small, see again the discussion in Section 2.7, less than 0.1 MeV and close to that obtained in Ref. [106]. We expect therefore that the major reductions of the neutrino rates in the core come from superconducting protons in the

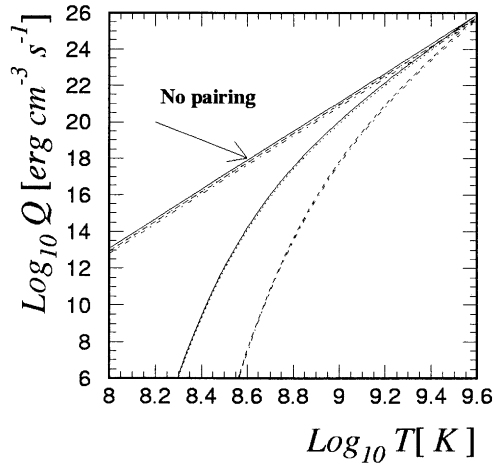


Fig. 46. Temperature dependence of neutrino energy loss rates in a neutron star core at a total baryonic density of 0.3 fm^{-3} with muons and electrons. Solid line represents Eq. (2) with electrons, dotted line is Eq. (2) with muons, dashed line is Eq. (3) with electrons while the dash-dotted line is the processes of Eq. (3) with muons. The corresponding results with no pairing are also shown.

1S_0 state. The contribution from neutrino-pair bremsstrahlung in nucleon–nucleon collisions in the core is also, for most temperature ranges relevant for neutron stars, smaller than the contribution from modified Urca processes [183]. Possible candidates are then direct Urca processes due to hyperons and isobars, as suggested in Refs. [114,179], or neutrino production through exotic states of matter, like kaon or pion condensation [36,91,96] or quark matter [30,130].

In conclusion, superfluidity reduces the neutrino emissivities considerably for the standard cooling model. However, before a firm conclusion from cooling calculations can be obtained, one needs much more reliable estimates of various emissivity processes in dense matter. In addition, such processes should be calculated consistently within the same many-body approach and EoS model for the interior of a star.

5.9. Supernovae

Neutron stars are born in type II or Ib supernovae at a rate of 1–3 per century in our galaxy. Once the iron core in massive stars exceed the corresponding Chandrasekhar mass, it collapses adiabatically until it is stopped by the incompressibility of nuclear matter, bounces, creates shock waves, stalls by infalling matter, and presumably explodes by neutrinos blowing the infalling matter off after a few tens of seconds.

Measurements of isotope abundances of various elements (r- and s-processes) give some insight in densities and temperatures during certain stages of the explosions. Neutrinos were also detected from SN1987A in the Large Magellan Cloud.

Neutron stars are normally treated as an input to supernova calculations of the complicated transport processes of baryons, photons, leptons and neutrinos going on during the explosion. Thus supernovae do not provide much information on details on neutron star structure presently. Recent supernova models include convection and spherical asymmetries (see, e.g. [192]).

The softer the equation of state the denser the matter is compressed before it bounces and the deeper into the gravitational well the star has fallen. Also, a softer EoS creates a more coherent shock wave that excites the matter less. The additional gravitational energy available can be transferred to neutrino generation which is believed to power the supernova explosion. Besides softening the EoS a first-order phase transition would store latent heat which also could affect supernovae.

With luck we may observe a supernova nearby in the near future which produces a rapidly rotating pulsar. Light curves and neutrino counts will test supernova and neutron star models. The rapid spin down may be exploited to test the structure and possible phase transitions in the cores of neutron stars [6–8].

5.10. Gamma-ray bursters

In the late 1960s the Vela satellite was launched carrying a gamma-ray detector in order to check the nuclear test ban treaty in space. It was a huge success because numerous gamma-ray bursts (GRB) were observed [193] and (more importantly) they did not come from Earth. Later (when declassified) the Russians confirmed the GRB. Numerous observations by the Pioneer Venus Orbiter, Compton Gamma Ray Observatory, Burst And Transient Source Experiment, and later gamma-ray detectors now find bursts every day. The GRB do not repeat (except for a few soft gamma-ray repeaters). Their duration varies from milliseconds to minutes. The short bursts imply a small source size $\lesssim c \cdot 1 \text{ ms} \sim 100 \text{ km}$, which points towards neutron stars or black holes. The gamma-rays have energy in the range 30 keV–2 MeV. The high-energy gamma rays are above the threshold for $\gamma \rightarrow e^+e^-$ photo production which implies that the radiation probably is relativistically expanding.

The thousands of GRB observed show a high isotropy. Thus GRB cannot be produced in the very anisotropic discs of our solar system or galaxy or even an extended galactic halo. The final kill to such (and many other) models came from the BeppoSax observations on May 8th, 1997, where a burst could be pin-pointed on the sky within an arcminut, which subsequently allowed ground based observations of an afterglow in optical and radio wavelengths. Fe-II and Mg-II absorption lines were found at high redshifts of $z = 0.835$. Assuming isotropic flux gives an energy output of $E_\gamma \gtrsim 10^{51} \text{ ergs}$ within seconds, which is about the same energy of the optical display and kinetic energy of the ejecta in a supernova. The total energy release in a supernova is $\sim 10^{53} \text{ erg's}$ of which $\sim 99\%$ is carried away by neutrinos and antineutrinos. In comparison a few kilometer size asteroid impacting with Earth's orbital velocity of 30 km/s releases $\sim 10^{31} \text{ ergs}$ and the world's nuclear arsenal contains (only) $\sim 10^5 \text{ megatons} \sim 10^{27} \text{ ergs}$ of explosive energy. At the time of writing, two dozens of GRB with afterglow in X-ray, one dozen in optical and half a dozen in radio waves have been discovered.

Merging neutron stars may be responsible for gamma-ray bursts [192]. Binary pulsars are rapidly spiralling inwards and will eventually merge and create a gigantic explosion and perhaps collapse to a black hole. From the number of binary pulsars and spiral rates, one estimates about one merger per million year per galaxy. With $\sim 10^9$ galaxies at cosmological distances $z \lesssim 1$ this gives about the observed rate of GRB. However, detailed calculations have problems with baryon contamination, i.e. the baryons ejected absorb photons in the relativistically expanding photosphere. Accreting black holes have also been suggested to act as beaming GRB. Recently, evidence

for beaming or jets has been found [2] corresponding to $E \sim 10^{51}$ ergs. Also, a bright supernova coinciding with GRB 980326 has been found which points toward that GRB are a special class of type Ic supernova where cores collapse to black holes.

So far, the physics producing these GRB is not understood. The time scales and the enormous power output points towards neutron star or black hole objects. We hope to learn more about these objects and maybe someday they can be used to gain information on neutron stars.

6. Conclusions

The aim of this work has been to give a survey of recent progresses in the construction of the equation of state for dense neutron star matter and possible implications for phase transitions inside neutron stars and the connections to neutron star observables. We will here try to recapitulate several of the arguments presented.

6.1. Many-body approaches to the equation of state

In Section 2 we attempted at a review of the present status of microscopic many-body approaches to dense neutron star matter. Several features emerged:

- Within non-relativistic lowest-order Brueckner theory (LOB), all the new phase-shift equivalent nucleon–nucleon potentials yield essentially similar equations of state up to densities of $3\text{--}4n_0$ for both pure neutron matter and β -stable matter. Other properties like the symmetry energy and proton fractions do also show a similar quantitative agreement.
- The inclusion of more complicated many-body terms at the two-body level does not alter this picture and even the recent summation of three-hole line diagrams of Baldo and co-workers [54,55] results in an EoS which is close to LOB when a continuous choice is used for the single-particle energies in matter.
- At densities up to nuclear matter saturation density n_0 , basically all many-body approaches discussed here give very similar equations of state.
- In symmetric nuclear matter the situation is however different, since there the nuclear tensor force is much more dominant due to the presence of the 3S_1 and 3D_1 partial waves. This has also consequences for the three-body interactions, arising from both effective and real three-body force terms. This is expected since the strong isospin $T = 0$ channel is present in the three-body nnp and npp clusters. In neutron matter however, such clusters are in general small at densities up to n_0 . Similar behaviors are also seen in recent works on the energy of pure neutron drops [194] and larger-scale shell-model calculations of Sn isotopes including effective three-body interactions [195]. However, for PNM and densities greater than n_0 differences do however occur when one introduces real three-body forces and/or includes relativistic corrections. In a similar way, relativistic BHF calculations, yield also significant corrections above saturation density.
- Based on the microscopic calculation of Akmal et al. [14], a simple parametrization of the EoS was given where the energy per particle could be written as

$$\mathcal{E} = \mathcal{E}_0 u \frac{u - 2 - \delta}{1 + \delta u} + S_0 u^\gamma x^2 ,$$

with $\mathcal{E}_0 = 15.8 \text{ MeV}$, $\delta \simeq 0.2$, symmetry energy $S_0 = 32 \text{ MeV}$ and $\gamma = 0.6$. Causality is ensured by $\delta \geq 0.13$.

In the case of non-nucleonic degrees of freedom we discussed also recent progresses in the construction of hyperon–hyperon interactions [19,20] and applications to neutron star matter [15]. Recent results for β -stable matter with these hyperon–hyperon interactions were also discussed [89]. In this work however, we chose to focus on the Bag model in order to deal with non-nucleonic degrees of freedom in our discussion on phase transitions.

For studies of superfluidity in neutron star matter, one needs still a careful analysis of polarization effects, especially for the 1S_0 proton contaminant. For superfluid neutrons in the 3P_2 partial wave, one needs nucleon–nucleon interactions which are fitted up to at least 1 GeV in lab energy before firm conclusions can be reached. These points leave clearly a large uncertainty for the role of superfluidity in cooling studies.

6.2. Phase transitions and stiffness of EoS from masses of neutron stars

We have discussed a number of possible phase transitions in dense nuclear matter such as pion, kaon and hyperon condensation, superfluidity and quark matter. We have specifically treated the nuclear to quark matter phase transition and the possible mixed phase that can occur in more than one component systems and replace the standard Maxwell construction. The structure of the mixed phase is similar to the mixed phase in the inner crust of neutron stars of nuclei and the neutron gas. However, as the mixed quark and nuclear matter phase can occur already at a few normal nuclear matter densities, it can soften the EoS in cores of neutron stars significantly and lower the maximum mass. A number of numerical calculations of rotating neutron stars with and without phase transitions were given.

The calculated maximum masses were discussed with the observed ones and leave two natural options:

Case I: The large masses of the neutron stars in QPO 4U 1820-30 ($M = 2.3M_\odot$), PSR J1012 + 5307 ($M = 2.1 \pm 0.4M_\odot$), Vela X – 1 ($M = 1.9 \pm 0.1M_\odot$), and Cygnus X – 2 ($M = 1.8 \pm 0.4M_\odot$), turn out to be correct and are complemented by other neutron stars with masses around $\sim 2M_\odot$.

As a consequence, the EoS of dense nuclear matter is severely restricted and only the stiffest EoS allowed by causality are allowed (i.e. $\delta \sim 0.2$). Also any significant phase transition can be excluded at densities below $\lesssim 5n_0$.

That the radio binary pulsars all have masses around $1.4M_\odot$ is then probably due to the formation mechanism in supernovae and related to the Chandrasekhar mass $M_{\text{ch}} \simeq 1.4M_\odot$ of white dwarfs. Neutron stars can subsequently acquire larger masses by accretion.

Case II: The heavy neutron stars proves erroneous by more detailed observations and only the $\sim 1.4M_\odot$ masses are found.

If even in accreting neutron stars does not produce neutron stars heavier than say $\gtrsim 1.5M_\odot$, this indicates that heavier neutron stars simply are not stable which in turn implies a soft EoS, either $\delta \gtrsim 0.4$ or a significant phase transition.

Either way, the result provides important information on neutrons stars, the EoS of dense hadronic matter and possible phase transitions.

Surface temperatures can be estimated from spectra and from the measured fluxes and known distances, one can extract the surface area of the emitting spot. This gives unfortunately only a lower limit on the neutron star size, R . If it becomes possible to measure both mass and radii of neutron stars, one can plot an observational (M, R) curve in Fig. 33, which uniquely determines the EoS for strongly interacting matter at zero temperature.

Pulsar rotation frequencies and glitches are other promising signals that could reveal phase transitions. Besides the standard glitches also giant glitches were mentioned and in particular the characteristic behavior of angular velocities when a first-order phase transition occurs right in the center of the star.

We impatiently await future observations and determinations of neutron star masses, radii, angular velocities, surface temperatures and luminosities, magnetic fields, etc., that will answer these questions.

Acknowledgements

Needless to say, we have benefitted immensely from umpteenth interactions with many colleagues. Especially, we would like to thank Øystein Elgarøy and Lars Engvik for providing us with several inputs to various figures and many invaluable comments on the present work. Moreover, we are much indebted to Marcello Baldo for sending us the data for Fig. 12, to Fred Lamb for keeping us updated on QPO's, and to Vijay Pandharipande and Geoff Ravenhall for providing us with the data for the equation of state from Ref. [14] and for numerous discussions on nuclear many-body theory. In addition, we wish to thank, Gordon Baym, Fabio de Blasio, Greg Carter, Alessandro Drago, Lex Dieperink, Jens Hjorth, Andy Jackson, Gianluca Lazzari, Ruprecht Machleidt, Larry McLerran, Ben Mottelson, Herbert Müther, Eivind Osnes, Erlend Østgaard, Chris Pethick, Artur Polls, Angels Ramos, Hans-Joseph Schulze, Ubaldo Tambini and Isaac Vidaña for the many discussions on the nuclear many-body problem and neutron star physics.

References

- [1] R. Wijnands, M. van der Klis, *Nature* 394 (1998) 344. D. Chakrabarty, E.H. Morgan, *Nature* 395 (1998) 346.
- [2] S.R. Kulkarni et al., astro-ph/9905301.
- [3] C. Thompson, R.C. Duncan, *Astrophys. J.* 408 (1994) 194; *Astrophys. J.* 473 (1996).
- [4] W. Zhang, T.E. Strohmayer, J.H. Swank, *Astrophys. J.* 482 (1997) L167.
- [5] F.M. Walter, L.D. Matthews, *Nature* 389 (1997) 358; F.M. Walter, S.J. Wolk, R. Neuhäuser, *Nature* 379 (1996) 233.
- [6] N.K. Glendenning, *Phys. Rev. D* 46 (1992) 1274.
- [7] N.K. Glendenning, S. Pei, F. Weber, *Phys. Rev. Lett.* 79 (1997) 1603.
- [8] H. Heiselberg, M. Hjorth-Jensen, *Phys. Rev. Lett.* 80 (1998) 5485; A sign error has been corrected in Eq. (136).
- [9] Ø. Elgarøy, L. Engvik, M. Hjorth-Jensen, E. Osnes, *Phys. Rev. Lett.* 77 (1996) 1421.

- [10] J.C. Collins, M.J. Perry, *Phys. Rev. Lett.* 34 (1975) 1353; G. Baym, S.A. Chin, *Phys. Lett. B* 62 (1976) 241; G.F. Chapline, M. Nauenberg, *Nature* 264 (1976) and *Phys. Rev. D* 16 (1977) 450; M.B. Kislinger, P.D. Morley, *Astrophys. J.* 219 (1978) 1017; W.B. Fechner, P.C. Joss, *Nature* 274 (1978) 347; B. Freedman, L. McLerran, *Phys. Rev. D* 17 (1978) 1109; V. Baluni, *Phys. Rev. D* 17 (1978) 2092; A. Rosenhauer, E.F. Staubo, L.P. Csernai, T. Øvergård, E. Østgaard, *Nucl. Phys. A* 540 (1992) 630.
- [11] H. Heiselberg, C.J. Pethick, E.F. Staubo, *Phys. Rev. Lett.* 70 (1993) 1355; *Nucl. Phys. A* 566 (1994) 577c.
- [12] D.B. Kaplan, A.E. Nelson, *Phys. Lett. B* 291 (1986) 57.
- [13] A. Akmal, V.R. Pandharipande, *Phys. Rev. C* 56 (1997) 2261.
- [14] A. Akmal, V.R. Pandharipande, D.G. Ravenhall, *Phys. Rev. C* 58 (1998) 1804.
- [15] H.-J. Schulze, M. Baldo, U. Lombardo, J. Cugnon, A. Lejeune, *Phys. Rev. C* 57 (1998) 704; M. Baldo, G.F. Burgio, H.-J. Schulze, *Phys. Rev. C* 58 (1998) 3688.
- [16] A. Reuber, K. Holinde, J. Speth, *Nucl. Phys. A* 585 (1994) 543.
- [17] J. Schaffner, I. Mishustin, *Phys. Rev. C* 53 (1996) 1416.
- [18] R. Knorren, M. Prakash, P.J. Ellis, *Phys. Rev. C* 52 (1995) 3470.
- [19] V.G.J. Stoks, T.-S.H. Lee, *Phys. Rev. C* 60 (1999) 024006.
- [20] V.G.J. Stoks, Th.A. Rijken, *Phys. Rev. C* 59 (1999) 3009.
- [21] M. Kutschera, W. Broniowski, A. Kotlorz, *Phys. Lett. B* 237 (1990) 159.
- [22] L.B. Leinson, A. Pérez, *JHEP* 9 (1998) 20; S. Chakrabarty, D. Bandyopadhyay, S. Pal, *Phys. Rev. Lett.* 78 (1997) 2898; *ibid.* 79 (1997) 2176.
- [23] D.R. Gies, C.T. Bolton, *Astrophys. J.* 304 (1986) 371.
- [24] A.P. Cowley, D. Crampton, J.B. Hutchings, R.A. Remillard, J.P. Penfold, *Astrophys. J.* 272 (1983) 118.
- [25] J.E. McClintock, R.A. Remillard, *Astrophys. J.* 308 (1986) 110.
- [26] J. Casares, P.A. Charles, T. Naylor, *Nature* 355 (1992) 614.
- [27] C.J. Pethick, D.G. Ravenhall, *Ann. Rev. Nucl. Part. Sci.* 45 (1995) 429.
- [28] M. Prakash, I. Bombaci, M. Prakash, P.J. Ellis, J.M. Lattimer, R. Knorren, *Phys. Rep.* 280 (1997) 1.
- [29] S. Tsuruta, *Phys. Rep.* 292 (1998) 1.
- [30] N.K. Glendenning, in: *Structure of Hadrons and Hadronic Matter*, World Scientific, Singapore, 1991, 275; N.K. Glendenning, *Compact Stars*, Springer, Berlin, 1997.
- [31] B.D. Serot, J.D. Walecka, *Adv. Nucl. Phys.* 16 (1986) 1.
- [32] See, e.g. J. Madsen, preprint astro-ph/9809032 and references therein.
- [33] A. Drago, U. Tambini, M. Hjorth-Jensen, *Phys. Lett. B* 380 (1996) 13.
- [34] C.P. Lorenz, D.G. Ravenhall, C.J. Pethick, *Phys. Rev. Lett.* 70 (1993) 379.
- [35] C.J. Pethick, D.G. Ravenhall, C.P. Lorenz, *Nucl. Phys. A* 584 (1995) 675.
- [36] A.B. Migdal, E.E. Saperstein, M.A. Troitsky, D.N. Voskresensky, *Phys. Rep.* 192 (1990) 179.
- [37] V.G.J. Stoks, R.A.M. Klomp, C.P.F. Terheggen, J.J. de Swart, *Phys. Rev. C* 49 (1994) 2950.
- [38] R.B. Wiringa, V.G.J. Stoks, R. Schiavilla, *Phys. Rev. C* 51 (1995) 38.
- [39] R. Machleidt, F. Sammarruca, Y. Song, *Phys. Rev. C* 53 (1996) R1483.
- [40] R. Machleidt, *Adv. Nucl. Phys.* 19 (1989) 185.
- [41] L. Engvik, M. Hjorth-Jensen, R. Machleidt, H. Mütter, A. Polls, *Nucl. Phys. A* 627 (1997) 85.
- [42] A. Polls, H. Mütter, R. Machleidt, M. Hjorth-Jensen, *Phys. Lett. B* 432 (1998) 1.
- [43] M. Hjorth-Jensen, T.T.S. Kuo, E. Osnes, *Phys. Rep.* 261 (1995) 125.
- [44] J.P. Jeukenne, A. Lejeune, C. Mahaux, *Phys. Rep.* 25 (1976) 83; C. Mahaux, P.F. Bortignon, R.A. Broglia, C.H. Dasso, *Phys. Rep.* 120 (1985) 1.
- [45] A. Nogga, D. Hüber, H. Kamada, W. Glöckle, *Phys. Lett. B* 409 (1997) 19.
- [46] L. Engvik, E. Osnes, M. Hjorth-Jensen, G. Bao, E. Østgaard, *Astrophys. J.* 469 (1996) 794.
- [47] S.L. Shapiro, S.A. Teukolsky, *Black Holes, White Dwarfs and Neutron Stars*, Wiley, New York, 1983.
- [48] C. Mahaux, R. Sartor, *Phys. Rep.* 211 (1992) 53.
- [49] R.V. Reid, *Ann. Phys.* 50 (1968) 411.
- [50] A. Ramos, Ph.D. Thesis, University of Barcelona, 1988, unpublished.
- [51] A. Ramos, A. Polls, W.H. Dickhoff, *Nucl. Phys. A* 503 (1989) 1.
- [52] S.D. Yang, J. Heyer, T.T.S. Kuo, *Nucl. Phys. A* 448 (1986) 420.
- [53] W.H. Dickhoff, H. Mütter, *Rep. Prog. Phys.* 55 (1992) 1947; W.H. Dickhoff, H. Mütter, *Nucl. Phys. A* 473 (1987) 394.

- [54] H.Q. Song, M. Baldo, G. Giansiracusa, U. Lombardo, *Phys. Lett. B* 411 (1997) 237.
- [55] H.Q. Song, M. Baldo, G. Giansiracusa, U. Lombardo, *Phys. Rev. Lett.* 81 (1998) 1584; M. Baldo, private communication.
- [56] M. Baldo, I. Bombaci, G.F. Burgio, *Astron. Astrophys.* 328 (1997) 274.
- [57] L. Engvik, M. Hjorth-Jensen, E. Osnes, T.T.S. Kuo, *Nucl. Phys. A* 622 (1997) 553.
- [58] B.D. Day, *Phys. Rev. C* 24 (1981) 1203.
- [59] B.D. Day, *Comments Nucl. Part. Phys.* 11 (1983) 115.
- [60] A.D. Jackson, *Ann. Rev. Nucl. Part. Phys.* 33 (1983) 105.
- [61] A.D. Jackson, A. Lande, R.A. Smith, *Phys. Rep.* 86 (1982) 55; A. Lande, R.A. Smith, *Phys. Rev. A* 45 (1992) 913 and references therein.
- [62] H. Kümmel, K.H. Lührmann, J.G. Zabolitzky, *Phys. Rep.* 36 (1977) 1.
- [63] A. Fabrocini, F. Arias de SAVEDRA, G. C  , P. Folgarait, *Phys. Rev. C* 57 (1998) 1668 and references therein.
- [64] V.R. Pandharipande, R.B. Wiringa, *Rev. Mod. Phys.* 51 (1979) 821.
- [65] B.D. Day, R.B. Wiringa, *Phys. Rev. C* 32 (1985) 1057.
- [66] J.L. Forest, Ph.D. Thesis, University of Illinois, Urbana-Champaign, 1997, unpublished.
- [67] B.S. Pudliner, V.R. Pandharipande, J. Carlson, S.C. Pieper, R.B. Wiringa, *Phys. Rev. C* 56 (1997) 1720.
- [68] A. Akmal, Ph.D. Thesis, University of Illinois, Urbana-Champaign, 1998, unpublished.
- [69] I.E. Lagaris, V.R. Pandharipande, *Nucl. Phys. A* 369 (1981) 470 and references therein.
- [70] B.D. Serot, *Rep. Prog. Phys.* 55 (1992) 1855.
- [71] C.J. Horowitz, B.D. Serot, *Nucl. Phys. A* 464 (1987) 613.
- [72] R. Brockmann, *Phys. Rev. C* 18 (1978) 1510.
- [73] L.S. Celenza, C. Shakin, *Relativistic Nuclear Physics*, World Scientific, Singapore, 1986.
- [74] R. Brockmann, R. Machleidt, *Phys. Rev. C* 42 (1990) 1965.
- [75] B. ter Haar, R. Malfliet, *Phys. Rep.* 149 (1987) 207.
- [76] R.H. Thompson, *Phys. Rev. D* 1 (1970) 110.
- [77] F. de Jong, H. Lense, *Phys. Rev. C* 58 (1998) 890; *ibid.* C 57 (1998) 3099.
- [78] C. Itzykson, J.-B. Zuber, *Quantum Field Theory*, McGraw-Hill, New York, 1980.
- [79] J.L. Forest, V.R. Pandharipande, J.L. Friar, *Phys. Rev. C* 52 (1995) 568.
- [80] R.A. Krafcik, L.L. Foldy, *Phys. Rev. D* 10 (1974) 1777.
- [81] J.L. Friar, *Phys. Rev. C* 12 (1975) 695.
- [82] J. Carlson, V.R. Pandharipande, R. Schiavilla, *Phys. Rev. C* 47 (1993) 484.
- [83] J.L. Forest, V.R. Pandharipande, J. Carlson, R. Schiavilla, *Phys. Rev. C* 52 (1995) 576.
- [84] G.E. Brown, W. Weise, G. Baym, J. Speth, *Comments Nucl. Part. Phys.* 17 (1987) 39.
- [85] V. Kalogera, G. Baym, *Astrophys. J.* 470 (1996) L61.
- [86] Th.A. Rijken, V.G.J. Stoks, Y. Yamamoto, *Phys. Rev. C* 59 (1998) 21.
- [87] S. Balberg, A. Gal, *Nucl. Phys. A* 625 (1997) 435.
- [88] S. Balberg, I. Lichtenstadt, G.B. Cook, *Astrophys. J. Suppl.* 121 (1999) 515.
- [89] I. Vida  a, A. Polls, A. Ramos, L. Engvik, M. Hjorth-Jensen, *Phys. Rev. C*, in press.
- [90] R.B. Wiringa, V. Fiks, A. Fabrocini, *Phys. Rev. C* 38 (1988) 1010.
- [91] G. Brown, C. Lee, M. Rho, V. Thorsson, *Nucl. Phys. A* 572 (1994) 693.
- [92] T. Waas, M. Rho, W. Weise, *Nucl. Phys. A* 617 (1997) 449–463.
- [93] V.R. Pandharipande, C.J. Pethick, V. Thorsson, *Phys. Rev. Lett.* 75 (1995) 4567.
- [94] J. Carlson, H. Heiselberg, V.R. Pandharipande, to be published.
- [95] N. Glendenning, J. Schaffner, *Phys. Rev. Lett.* 81 (1998) 4564.
- [96] R. Tamagaki et al., *Prog. Theor. Phys. Supplement* 112 (1993) and references therein.
- [97] J.A. Sauls, in: H.   gelman, E.P.J. van den Heuvel (Eds.), *Timing Neutron Stars*, Kluwer, Dordrecht, 1989, p. 457.
- [98] M. Baldo, J. Cugnon, A. Lejeune, U. Lombardo, *Nucl. Phys. A* 515 (1990) 409.
- [99] V.A. Kodel, V.V. Kodel, J.W. Clark, *Nucl. Phys. A* 598 (1996) 390.
- [100]   . Elgar  y, M. Hjorth-Jensen, *Phys. Rev. C* 57 (1998) 1174.
- [101] H.-J. Schulze, J. Cugnon, A. Lejeune, M. Baldo, U. Lombardo, *Phys. Lett. B* 375 (1996) 1.
- [102] J.M.C. Chen, J.W. Clark, E. Krotschek, R.A. Smith, *Nucl. Phys. A* 451 (1986) 509; J.M.C. Chen, J.W. Clark, R.D. Dave, V.V. Khodel, *Nucl. Phys. A* 555 (1993) 59.

- [103] T.L. Ainsworth, J. Wambach, D. Pines, *Phys. Lett. B* 222 (1989) 173; J. Wambach, T.L. Ainsworth, D. Pines, *Nucl. Phys. A* 555 (1993) 128.
- [104] L. Amundsen, E. Østgaard, *Nucl. Phys. A* 437 (1985) 487.
- [105] M. Baldo, J. Cugnon, A. Lejeune, U. Lombardo, *Nucl. Phys. A* 536 (1992) 349.
- [106] T. Takatsuka, R. Tamagaki, *Prog. Theor. Phys. Suppl.* 112 (1993) 27.
- [107] Ø. Elgarøy, L. Engvik, M. Hjorth-Jensen, E. Osnes, *Nucl. Phys. A* 607 (1996) 425.
- [108] V.V. Khodel, Ph.D. Thesis, Washington University, St. Louis, 1997, unpublished. V.A. Khodel, V.V. Khodel, J.W. Clark, *Phys. Rev. Lett.* 81 (1998) 3828.
- [109] M. Baldo, Ø. Elgarøy, L. Engvik, M. Hjorth-Jensen, H.-J. Schulze, *Phys. Rev. C* 58 (1998) 1921.
- [110] P.W. Anderson, P. Morel, *Phys. Rev.* 123 (1961) 1911.
- [111] H. Kucharek, P. Ring, *Z. Phys. A* 339 (1990) 23.
- [112] Ø. Elgarøy, L. Engvik, M. Hjorth-Jensen, E. Osnes, *Nucl. Phys. A* 604 (1996) 466.
- [113] Ø. Elgarøy, L. Engvik, E. Osnes, F.V. De Blasio, M. Hjorth-Jensen, G. Lazzari, *Phys. Rev. Lett.* 76 (1996) 1994.
- [114] Ch. Schaab, S. Balberg, J. Schaffner-Bielich, *Astrophys. J.* 504 (1998) L99.
- [115] M.A. Halasz, A.D. Jackson, R.E. Shrock, M.A. Stephanov, J.J.M. Verbaarschot, *Phys. Rev. D* 58 (1998) 096007.
- [116] M. Alford, K. Rajagopal, F. Wilczek, *Phys. Lett. B* 422 (1998) 247.
- [117] Y. Iwasaki, K. Kanaya, S. Kaya, S. Sakai, T. Yoshi, *Phys. Rev. D* 54 (1996) 7010.
- [118] T. Schafer, F. Wilczek, *Phys. Rev. Lett.* 82 (1999) 3956.
- [119] J.I. Kapusta, *Finite Temperature Field Theory*, Cambridge University Press, Cambridge, 1989.
- [120] G.A. Baym, S.A. Chin, *Nucl. Phys. A* 262 (1976) 527.
- [121] J. Cleymans, R.V. Gavai, E. Suhonen, *Phys. Rep.* 130 (1986) 217.
- [122] H. Satz, *Phys. Lett. B* 113 (1982) 245.
- [123] H.J. Pirner, *Prog. Part. Nucl. Phys.* 29 (1992) 33.
- [124] M.C. Birse, *Prog. Part. Nucl. Phys.* 25 (1990) 1.
- [125] A. Drago, A. Fiolhais, U. Tambini, *Nucl. Phys. A* 588 (1995) 801.
- [126] V. Barone, A. Drago, *Nucl. Phys. A* 552 (1993) 479; *A* 560 (1993) 1076; V. Barone, A. Drago, M. Fiolhais, *Phys. Lett. B* 338 (1994) 433.
- [127] M. Fiolhais, T. Neuber, K. Goeke, *Nucl. Phys. A* 570 (1994) 782.
- [128] K. Bräuer, A. Drago, A. Faessler, *Nucl. Phys. A* 511 (1990) 558.
- [129] W. Broniowski, M. Čibej, M. Kutschera, M. Rosina, *Phys. Rev. D* 41 (1990) 285.
- [130] N. Iwamoto, *Ann. Phys.* 141 (1982) 1.
- [131] F. Weber, N.K. Glendenning, in: *Hadronic Matter and Rotating Relativistic Neutron Stars*, World Scientific, Singapore, 1992.
- [132] C.J. Pethick, D.G. Ravenhall, *Ann. Phys.* 183 (1988) 131.
- [133] D.G. Ravenhall, C.J. Pethick, J.R. Wilson, *Phys. Rev. Lett.* 50 (1983) 2066; R.D. Williams, S.E. Koonin, *Nucl. Phys. A* 435 (1985) 844; M. Lassant, H. Flocard, P. Bonche, P.H. Heenen, E. Suraud, *Astron. Astrophys.* 183 (1987) L3.
- [134] E.V. Shuryak, *Phys. Rep.* 61 (1980) 71.
- [135] M.S. Berger, R.L. Jaffe, *Phys. Rev. C* 35 (1987) 213; *Phys. Rev. C* 44 (1991) R566.
- [136] K. Kajantie, L. Kärkäinen, K. Rummukainen, *Nucl. Phys. B* 357 (1991) 693; S. Huang, J. Potvion, C. Rebbi, S. Sanielevici, *Phys. Rev. D* 43 (1991) 2056.
- [137] W.L. Slattery, G.D. Doolen, H.E. Dewitt, *Phys. Rev. A* 21 (1980) 2087.
- [138] J.M. Lattimer, C.J. Pethick, M. Prakash, P. Haensel, *Phys. Rev. Lett.* 66 (1991) 2701.
- [139] H. Heiselberg, in: G. Vassiliadis, A.D. Panagiotou, S. Kumar, J. Madsen (Eds.), *Strangeness Quark Matter*, World Scientific, Singapore, 1995, p. 298.
- [140] S.E. Thorsett, D. Chakrabarty, *Astrophys. J.* 512 (1999) 288.
- [141] J. van Paradijs, astro-ph/9802177 and in: R. Bucchieri, J. van Paradijs, M.A. Alpar (Eds.), *The Many Faces of Neutron Stars*, Kluwer, Dordrecht, 1999, in press.
- [142] M.C. Miller, F.K. Lamb, D. Psaltis, *Astrophys. J.* 508 (1998) 791; D. Psaltis, M. Mendez, R. Wijnands, J. Homan, P.G. Jonker, M. van der Klis, F.K. Lamb, E. Kuulkers, J. van Paradijs, W.H.G. Lewin, *Astrophys. J.* 520 (1999) 763.
- [143] P. Kaaret, E.C. Ford, K. Chen, *Astrophys. J.* 480 (1997) L27.
- [144] H. Heiselberg, M. Hjorth-Jensen, *Astrophys. J.* 525 (1999) L45; astro-ph/9904214.

- [145] S. Barziv et al., in preparation.
- [146] J.A. Orosz, E. Kuulkers, Mon. Not. R. Astron. Soc., in press.
- [147] J.B. Hartle, *Astrophys. J.* 150 (1967) 1005. J.B. Hartle, M.W. Munn, *Astrophys. J.* 198 (1975) 467.
- [148] J.R. Oppenheimer, G.M. Volkoff, *Phys. Rev.* 55 (1939) 374.
- [149] F. Weber, N.K. Glendenning, M.K. Weigel, *Astrophys. J.* 373 (1991) 579; in: W.Y. Pauchy Hwang, Shik-Chang Lee, Chin-Er Lee, D.J. Ernst (Eds.), *Rotating Neutron Stars and the Equation of State of Dense Matter*, Elsevier, Amsterdam, 1991, p. 309.
- [150] F. Weber, N.K. Glendenning, *Z. Phys. A* 399 (1991) 211.
- [151] E.M. Butterworth, J.R. Ipser, *Astrophys. J.* 204 (1976) 200.
- [152] J.L. Friedmann, J.R. Ipser, L. Parker, *Astrophys. J.* 304 (1986) 115; *Phys. Rev. Lett.* 62 (1989) 3015.
- [153] H. Bandō, T. Motoba, J. Žofka, *Int. J. Mod. Phys. A* 5 (1990) 4021.
- [154] N.K. Glendenning, C. Kettner, astro-ph/9807155.
- [155] G. Baym, *Neutron Stars and the Properties of Matter at High Density*, Nordita lecture notes, 1977, p. 107.
- [156] Z.F. Seidov, *Astrofizika* 3 (1967) 189; *Sov. Astron.-AJ* 15 (1971) 347.
- [157] H.A. Bethe, M.B. Johnson, *Nucl. Phys. A* 230 (1974) 1.
- [158] J. Tassoul, *Theory of Rotating Stars*, Princeton University Press, 1978.
- [159] B.R. Mottelson, J.G. Valatin, *Phys. Rev. Lett.* 5 (1960) 511.
- [160] A. Johnson, H. Ryde, S.A. Hjorth, *Nucl. Phys. A* 179 (1972) 753.
- [161] G. Baym, C.J. Pethick, *Ann. Rev. Nucl. Sci.* 25 (1975) 27; *Ann. Rev. Astron. Astrophys.* 17 (1979) 415.
- [162] D. Pines, in: J. Alpar, D. Pines (Eds.), *Neutrons Stars: Theory and Observation of the Neutron Stars*, Kluwer, Dordrecht, 1991, p. 57, and references therein; P.W. Anderson, N. Itoh, *Nature* 256 (1975) 25.
- [163] H. Ögelman, in: M. Alpar, Ü. Kiziloglu, J. van Paradijs (Eds.), *The Lives of the Neutron Stars*, Kluwer, Dordrecht, 1995, p. 101.
- [164] W. Becker, P. Predehl, J. Trümper, H. Ögelman, *IAU Circular*, Vol. 5554, 1992.
- [165] J.P. Finley, H. Ögelman, *IAU Circ. No.* 5787 (1993).
- [166] W. Becker, *IAU Circ. No.* 5805 (1993).
- [167] W. Becker, B. Aschenbach, in: M. Alpar, Ü. Kiziloglu, J. van Paradijs (Eds.), *The Lives of the Neutron Stars*, Kluwer, Dordrecht, 1995, p. 47.
- [168] F. Seward, F. Harnden, P. Murdin, D. Clark, *Astrophys. J.* 267 (1983) 698.
- [169] J.P. Finley, H. Ögelman, G. Hasinger, J. Trümper, *Astrophys. J.* 410 (1993) 323.
- [170] S. Safi-Harb, H. Ögelman, in: M. Alpar, Ü. Kiziloglu, J. van Paradijs (Eds.), *The Lives of the Neutron Stars*, Kluwer, Dordrecht, 1995, p. 53.
- [171] S. Yancopoulos, T. Hamilton, D. Helfland, *Bull. American Astron. Soc.* 25 (1993) 912.
- [172] F. Seward, Z.-R. Wang, *Astrophys. J.* 332 (1988) 199.
- [173] W. Becker, J. Trümper, *Nature* 365 (1993) 528.
- [174] H. Ögelman, J.P. Finley, H. Zimmermann, *Nature* 361 (1993) 136.
- [175] J.P. Finley, H. Ögelman, Ü. Kiziloglu, *Astrophys. J.* 394 (1992) L21.
- [176] J. Halpern, M. Ruderman, *Astrophys. J.* 415 (1993) 286.
- [177] H. Ögelman, J.P. Finley, *Astrophys. J.* 413 (1993) L31.
- [178] C.J. Pethick, *Rev. Mod. Phys.* 64 (1992) 1133.
- [179] M. Prakash, M. Prakash, J.M. Lattimer, C.J. Pethick, *Astrophys. J.* 390 (1992) L77.
- [180] M. Prakash, *Phys. Rep.* 242 (1994) 191.
- [181] H.-Y. Chiu, E.E. Salpeter, *Phys. Rev. Lett.* 12 (1964) 413.
- [182] I. Itoh, T. Tsuneto, *Prog. Theor. Phys.* 48 (1972) 149.
- [183] D.G. Yakovlev, K.P. Levenfish, *Astron. Astrophys.* 297 (1995) 717.
- [184] D. Page, *Astrophys. J.* 428 (1994) 250.
- [185] Ch. Schaab, D. Voskresensky, A.D. Sedrakian, F. Weber, M.K. Weigel, *Astron. Astrophys.* 321 (1997) 591; Ch. Schaab, F. Weber, M.K. Weigel, N.K. Glendenning, *Nucl. Phys. A* 605 (1996) 531.
- [186] Ch. Schaab, F. Weber, M.K. Weigel, *Astron. Astrophys.* 335 (1998) 596.
- [187] H. Umeda, N. Shibasaki, K. Nomoto, S. Tsuruta, *Astrophys. J.* 408 (1993) 186.
- [188] K. VanRiper, R. Epstein, B. Link, *Astrophys. J.* 448 (1995) 294.
- [189] B.L. Friman, O.V. Maxwell, *Astrophys. J.* 232 (1979) 541.

- [190] S. Tsuruta, Phys. Rep. 56 (1975) 237.
- [191] G. Glen, P. Sutherland, Astrophys. J. 239 (1980) 671.
- [192] E. Müller, H.-Th. Janka, Astron. Astrophys. 317 (1997) 140; M. Ruffert, H.-Th. Janka, Astron. Astrophys. 338 (1998) 535.
- [193] A.W. Klebesadel, I.B. Strong, R.A. Olsson, Astrophys. J. 182 (1973) L85.
- [194] B.S. Pudliner, A. Smerzi, J. Carlson, V.R. Pandharipande, S.C. Pieper, D.G. Ravenhall, Phys. Rev. Lett. 76 (1996) 2416.
- [195] T. Engeland, M. Hjorth-Jensen, in preparation.